RECONFIGURABLE CAVITY FILTERS WITH CONTACTLESS TUNERS

A Dissertation

Submitted to the Faculty

of

Purdue University

by

Mahmoud Abdelfattah

In Partial Fulfillment of the

Requirements for the Degree

of

Doctor of Philosophy

December 2019

Purdue University

West Lafayette, Indiana

THE PURDUE UNIVERSITY GRADUATE SCHOOL
STATEMENT OF DISSERTATION APPROVAL

Dr. Dimitrios Peroulis, Chair

School of Electrical and Computer Engineering

Dr. Sunil Bhave

School of Electrical and Computer Engineering

Dr. Byunghoo Jung

School of Electrical and Computer Engineering

Dr. Dana Weinstein

School of Electrical and Computer Engineering

Approved by:

Dr. Dimitrios Peroulis

Head of the School Graduate Program

To my father, you are my endless source of inspiration.

To my mother, your prayers give me strength.

To my wife, you are the comfort of my soul.

ACKNOWLEDGMENTS

Praise be to Allah, Lord of the Worlds.

First, I would like to express my gratitude to my advisor Prof. Dimitrios Peroulis for being a supportive, encouraging and patient supervisor. I would like to thank my advisory committee Prof. Sunil Bhave, Prof. Byunghoo Jung and Prof. Dana Weinstein for their sincere participation and insightful comments to this work.

Special thanks to Dr. Andy Yang, Dr. Mark Hickle, Dr. Mohammad Abu Khater, Dr. Mohammad Hagag, Ahmed Abdelraheem, Michael Sinanis and Prof. Dimitra Psychogio for enabling my research by spending the time and effort and by generously sharing their expertise and knowledge.

I would also like to acknowledge Prof. Khaldoon Abugharbieh, Prof. Issa Batarseh and Dr. Mohamad Mohamad for their mentorship, inspiration and guidance which prepared me for my graduate studies.

Finally, I would like to thank the people with the greatest influence on me. My parents for all their support, prayers, selfless sacrifices and great inspiration. My sister, for her unlimited care, kindness and compassion. My brothers for always being there whenever I needed them. My wife, for her love, care and patience which made all of this possible. My son, Yahya, for the immense joy he brought to my life. It is a great blessing to have you all in my life.

"and say, My Lord increase me in knowledge" [The Holy Quran 20:114]

TABLE OF CONTENTS

Page

Page

Page

LIST OF TABLES

LIST OF FIGURES

Figure Page

Figure Page

SYMBOLS

k_E	external coupling
k_E^*	equivalent external coupling
$k_{E,min}^*$	minimum external coupling to achieve absorptive notch
k_{12}	inter-resonator coupling
Q	quality-factor
Q_u	unloaded quality-factor
f_c	center frequency
f_e	even-mode frequency
f_o	odd-mode frequency
f_{err}	frequency error
Δf_m	modes frequency separation
θ_T	through line electrical length
P_{max}	maximum RF power before gas breakdown

ABBREVIATIONS

AN	absorptive notch
BPF	bandpass filter
BSF	bandstop filter
BW	bandwidth
CABW	constant absolute bandwidth
DM	dual mode
EM	electro-magnetic
EVA-mode	evanescent-mode
FBW	fractional bandwidth
FPGA	field programmable gate arrays
GCPW	grounded coplanar waveguide
HFSS	high frequency structure simulator
HMSIW	half-mode substrate-integrated-waveguide
IL	insertion loss
MEMS	micro-electro-mechanical systems
MMR	multi-mode resonator
mm-wave	millimeter wave
PCB	printed circuit board
PHC	power handling capability
QABSF	quasi-absorptive bandstop filter
QMSIW	quarter-mode substrate-integrated-waveguide
RF	radio frequency
RL	return loss
SIW	substrate integrated waveguide

TEM	transverse electro-magnetic
TL	transmission line
TR	tuning ratio
TZ	transmission zero
VNA	vector network analyzer
XeF_2	Xenon difluoride

ABSTRACT

Abdelfattah, Mahmoud Ph.D., Purdue University, December 2019. Reconfigurable Cavity Filters with Contactless Tuners. Major Professor: Dimitrios Peroulis.

The recent development of tunable microwave filters has shown their great potential for being an integral component in future wireless systems across a wide range of applications. In the last decade, filters based on tunable evanescent-mode (EVA) cavity resonators have demonstrated high performance with high quality factor (Q), wide tuning range and high power handling. However, the implementation of these filters suffers from practical limitations and reliability issues which restricted the practical utilization of these filters in different real-system applications. This dissertation will present and evaluate several practical and novel solutions to overcome these practical challenges without compromising the filter performance.

The first part of the dissertation focuses on the design of microwave and mm-wave quasi-absorptive bandstop filters with passive absolute bandwidth compensation utilizing micromachined cavity filters. The second part of the dissertation presents a novel method to tune substrate-integrated-waveguide (SIW) cavity filters using contactless tuners. In this work, a new tuning mechanism is proposed to overcome the mechanical reliability issues and the sensitive assembly of conventional tunable cavity filters. Furthermore, a new utilization of dual-mode SIW resonators is introduced in order to improve response selectivity and realize constant absolute bandwidth filters without compromising filter size and performance.

1. INTRODUCTION

1.1 Potential for Reconfigurable Filters

Recent developments in communications systems have been heading towards more efficient utilization of the available frequency spectrum. As a result, modern communication standards are relying more on multi-band and multi-carrier approaches. In order for wireless systems to enable these capabilities, the Radio Frequency (RF) front-end is required to demonstrate higher performance and satisfy more stringent specifications.

The conventional approach to accommodate these requirements is to further increase the size of the filter banks and the number of switches in the front-end. However, utilizing more switches will negatively affect the front-end performance and restrict the frequency and RF power it can handle. Alternatively, converting to a reconfigurable system approach that utilizes high performance tunable filters will have the potential to overcome these limitations [1].

Tunable filters could potentially replace filter banks in adaptable systems which react to different environmental requirements. Also, high power tunable filters can play an important role in the suppression of harmonics generated from power amplifiers used in high power transmitters [2]. Furthermore, as new systems are being continuously deployed and expected to coexist geographically, tunable filters could save operational and installing costs for network operators and allow them to efficiently manage hardware resources [1].

To enable wider implementation of tunable filters in real-systems, the filters are expected to demonstrate certain features: high unloaded quality factor Q_u, wide tuning range (TR), high power handling, small size, low cost, high manufacturability, simple integration, operation reliability, and filter response stability. In the past

decades, several works demonstrated tunable filters using different technologies, the majority of works were demonstrated based on planar microstrip technology. However, microstrip filters have limited Q_u values, less than 200, which doesn't meet the stringent specifications of modern systems. To achieve higher Q_u values, 3D filters such as combline, dielectric resonator, waveguide filters are needed. Previous works have reported Q_u up to few thousands [1]. However, these demonstrations suffered from low TR to less than 5%, and large form factor. Also, expensive CNC machining of metal substrates is usually used to fabricate these filters and sensitive assembly of the filters is required to maintain the high performance.

1.2 Evanescent-mode Cavity Filters

In the past decade, filters based on tunable evanescent (EVA)-mode cavity resonators have demonstrated high performance while avoiding many of the aforementioned disadvantages. Several works reported wide TR (larger than octave), high power handling and a small form factor while maintaining a high Q_u (300-800). These works have also demonstrated the flexibility of cavity-based resonators to realize various filter and diplexer functions with a large degree of reconfigurability. In addition, EVA-mode cavity filters have been implemented using different technologies such as CNC machining, substrate-integrated-waveguide (SIW) and silicon micro-machining [3–10].

The structure of tunable EVA-mode resonators is shown in Fig. 1.1. In general, a flexible tuner is utilized as a ceiling of the cavity creating an air gap with the center post. The cavity can be considered as coaxial transmission line (TL) that is shorted from one end and capacitively-loaded from the other end. The resonant frequency of the resonator can be tuned as the air gap is varied. The flexible tuner has been realized using different technologies such as piezoelectric actuators on top of a thin conductive membrane and electro-statically actuated MEMS membranes.

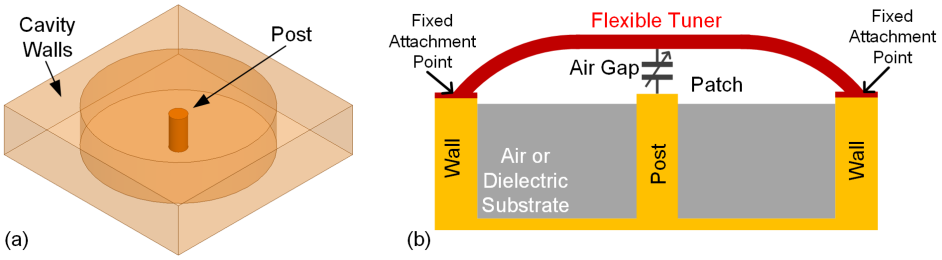

Fig. 1.1.: Tunable EVA-mode cavity resonator structure (a) 3D view (b) cross section.

1.3 Problem Statement

Despite the numerous high performance filter implementations based on EVA-mode cavity resonators, there exists some practical challenges limiting the deployment of these filters in real-systems. In this dissertation, two types of challenges will be investigated. The first type is relating to the filter response variation over the TR. The second type is pertaining to the reliability of the mechanical tuning scheme and the integration complexity/sensitivity. The specific challenges, addressed in this dissertation, are introduced and discussed in the following subsections.

1.3.1 Large ABW Variation of Tunable BSFs

Bandstop filters (BSF) have critical roles specifically in wide-band front-end systems. They are needed to suppress jamming and interference signal within or close to the band of interest. Quasi-Absorptive Bandstop (QABS) filters have been of great interest recently as they are capable of providing high rejection without requiring high Q resonators or higher order filters. One of the most popular topologies to realize a QABS response is show in Fig. 1.2. One of the practical challenges when utilizing this topology is the absolute bandwidth (ABW) variation across the TR. This is caused by the increase in the external coupling (k_E) over the TR as demonstrated in Fig. 1.3. It is shown that the 3-dB ABW variation is 732% over an octave TR given that

k_E doubles over the TR. As shown in Fig. 1.3, the large notch BW at the high end of the band is not acceptable which limits the useful TR of the filter.

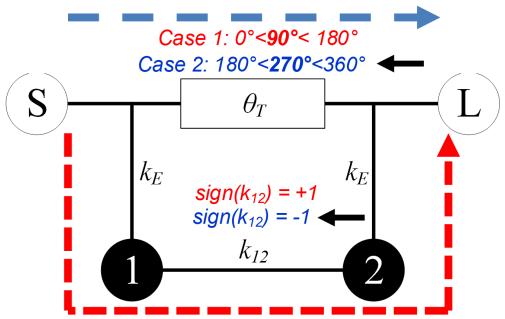

Fig. 1.2.: Hybrid-Coupler QABS filter topology.

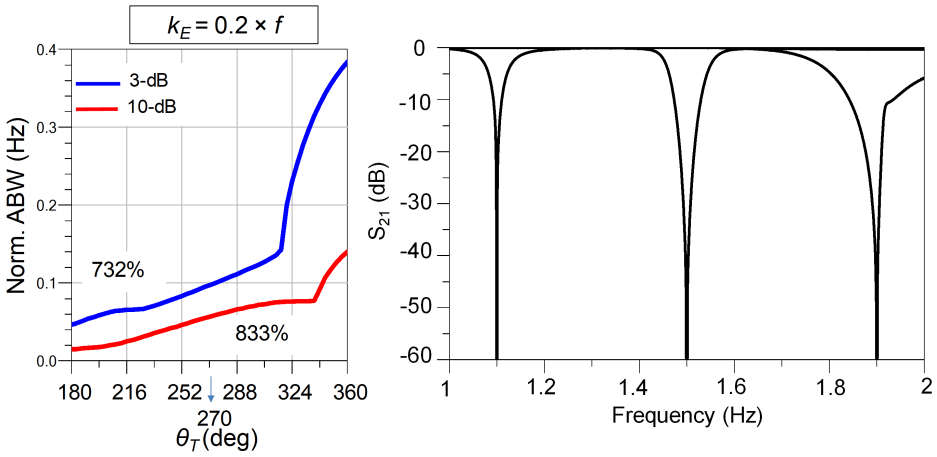

Fig. 1.3.: ABW variation across TR for conventional QABS filter.

1.3.2 Monitoring and Control of MEMS Tunable Cavity Filters

One of the main advantages of EVA-mode cavity resonators and filters is their scalability to high frequencies. Recent works have demonstrated such filters up to 110 GHz. These implementations are enabled through precise silicon micro-machining manufacturing and electrostatic MEMS tuning. An example of the filter assembly is shown in Fig. 1.4 [15]. Although previous works demonstrated high performance

using these filters, none have demonstrated a monitoring and control system to reliably control the MEMS diaphragms. Such control system is essential to guarantee the reliable operation of these filters in the field.

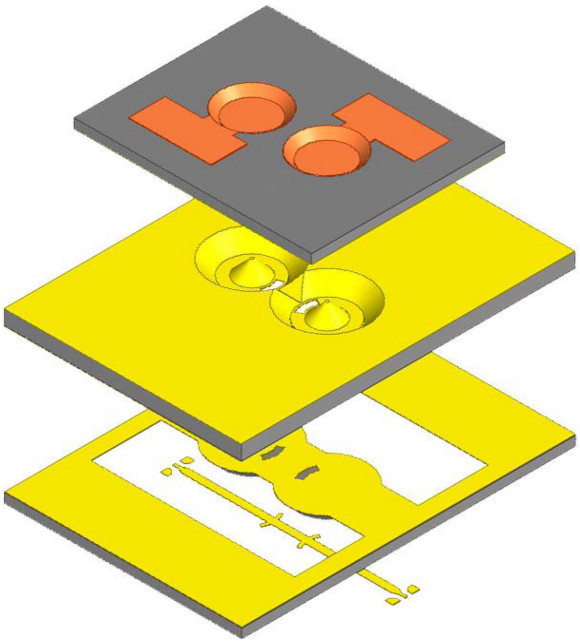

Fig. 1.4.: 3D Si micro-machined cavity filters, from top to bottom: MEMS tuner substrate, cavity substrate, signal substrate.

1.3.3 Reliable Tuning and Sensitive Integration of SIW Cavity Filters

Low cost and mass production are important aspects that need to be investigated in order to enable the transition of tunable filters to the commercial phase. Substrate-integrated-waveguide (SIW) technology is one of the main candidates to implement low cost cavity filters using only printed circuit board (PCB) conventional manufacturing. Most of the high performance filters that utilized this technology relied on piezo disk tuning of the resonators. However, this tuning scheme proved to result in operation reliability issues due to the mechanical variations in the piezo actuation such as hysteresis, creep, etc. Also, the manufacturing of these filter requires sensitive assembly process as the initial tuning gap is required to be very small (5μm) in order

to have sufficient TR. Therefore, it is crucial to modify the current tuning scheme to have simpler manufacturing and more reliable operation while maintain the high performance of the filters.

1.3.4 Independent Tuning for Dual-Mode SIW Cavity Resonators

Tunable dual-mode (DM) resonators are among the most desirable components for microwave filters as they enable the realization of a wide variety of reconfigurable filter responses while maintaining a compact size. Several works utilized DM cavity resonators using mechanical tuning and presented high Q_u and wide TR. However, in all these works the two resonant modes were tuned simultaneously without controlled separation between the modes. Other works used varactors to enable independent mode tuning which compromised the filter performance specifically Q_u and TR. To maintain filter performance, a novel tuning scheme is required to independently tune DM resonators. With independent mode tuning, one DM resonator could be utilized to realize a compact bandpass filter with center frequency and transmission zero reconfigurability as illustrated in Fig. 1.5.

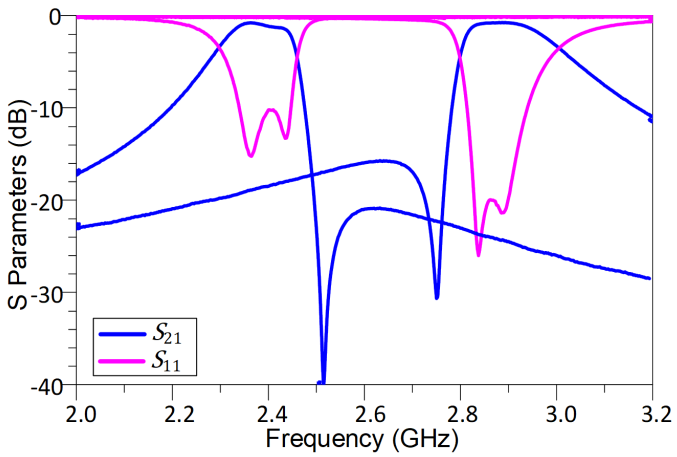

Fig. 1.5.: BPF filter with reconfigurable center frequency and transmission zero using one independently-tuned DM resonator.

1.3.5 Improved Selectivity and ABW Variation for BPFs

Recent research efforts for future SIW-based tunable filters focus on achieving two major goals. The first is producing a tunable response with a constant absolute bandwidth (CABW) over the TR. The second is improving the response selectivity by added transmission zeros (TZs) while maintaining the size compactness. An illustration of the desired response, for a second-order case, compared to a conventional response is shown in Fig. 1.6. Most conventional approaches used to achieve any or both goals suffer from one or more of these drawbacks; increased filter size, higher number of tuning elements or compromised filter performance due to using varactor tuned coupling structures. Successful solutions are expected to achieve the desired response in a single design of satisfactory filter RF performance such as low insertion loss, wide TR and high power handling. In addition, the proposed implementation is required to maintain the same size and number of tuning elements as the conventional filter.

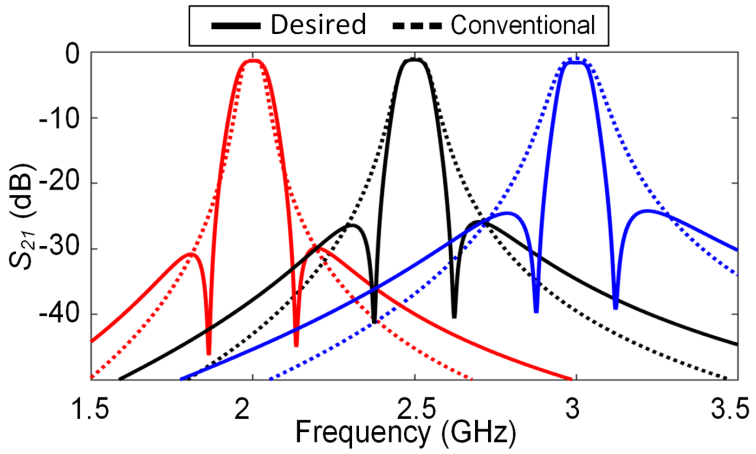

Fig. 1.6.: Desired response (CABW with improved selectivity) versus conventional BPF response for a second-order case.

This dissertation focuses on addressing the above mentioned challenges of tunable cavity resonators. The organization of the dissertation is as follows:

1. Chapter 2 presents two frequency-tunable QABS filters. One of the filters covers the 12-20 GHz range while the other covers the range 23-45 GHz. The designs employ, for the first time above 10 GHz, a dual-coupling slot scheme that limits the filter's ABW variation. In addition to wide TR, both filters demonstrate low 3-dB ABW variation and high rejection up to 60 dB.

2. Chapter 3 demonstrates a monitoring and control system for MEMS tunable EVA-mode filters. Inductive proximity sensing is utilized to detect the deflection of the tuning MEMS membrane. The sensed deflection is used as a feedback for a closed loop control of the MEMS bias voltage to deliver the desired deflection, and hence, desired RF response, based on an input from the user.

3. Chapter 4 presents a novel method to widely tune high Q EVA-mode cavity resonators and filters using contactless tuners. The proposed method resolves multiple challenges facing reliable manufacturing and operation of these filters by avoiding the attachment of the flexible tuner to the cavity and replacing it with capacitive contactless tuners. This work discusses the design consideration and trade-offs as well as demonstrates the performance of the proposed concept using SIW technology.

4. Chapter 5 presents a novel, widely-tunable, SIW, DM resonator with mode-independent frequency tuning. Two contactless tuners are used to enable the independent tuning. The DM resonator is utilized to realize a second-order reconfigurable bandpass filter based on a doublet-configuration. The filter measurements shows a tunable center frequency with a reconfigurable TZ that can be located on either the upper or the lower side of the passband.

5. Chapter 6 presents a new utilization of SIW-based DM resonators in an L-shaped coupling scheme to effectively realize a CABW tunable filter response with additional TZs. The presented solution achieves both goals without increasing the size or the number of tuning elements compared to a conventional

filter implementation. Using the proposed scheme, the even- and the odd- resonant modes are employed to produce the reflection zeros and TZs, respectively. Each resonator is designed to have one contactless tuner which tunes both modes simultaneously producing a controllable separation between the reflection zeros and TZs over the entire TR.

6. Chapter 7 summarizes the presented research efforts and provides recommendations for future work.

2. MICROWAVE AND MM-WAVE PASSIVELY-COMPENSATED TUNABLE QABS FILTERS

2.1 Introduction

Over the last decade tunable QABS filters have been of great interest as they offer effective solutions to interference problems in wide-band RF front-ends. Lumped-element-, microstrip- and substrate-integrated-waveguide-resonators have been employed in implementing such filters [11–13]. In recent works, MEMS-tunable silicon micro-machined EVA-mode cavity filters have demonstrated state-of-the-art performance in the Ka and W bands [14, 15].

One weakness of the presented designs is the large ABW variation over the TR. Specifically, none of the demonstrations at X-band or above have presented an effective solution to this problem. For instance, the 10-dB ABW in [16] varies by about 88% over its 27% TR (8.9-11.34 GHz). Similarly, the filter presented in [17] experiences a 400% variation in its 20-dB ABW over its 22% TR (9.6-11.7 GHz). Moreover, none of the high-frequency demonstrations have presented a practical solution for connectorizing the filters.

In this chapter, we present the design and implementation of two connectorized, high rejection QABS filters with ABW passive compensation. Filter A covers the range 12-20 GHz and Filter B covers the range 25.5-40 GHz with better than 40 dB notch rejection level. To limit bandwidth variation, the filters include a unique passive bandwidth compensation coupling scheme that is implemented for the first time at frequencies above than 10 GHz. Compared with state-of-the-art, the filters' performance represents at least 4× reduction in ABW variation.

Some of the text and figures presented in this chapter are based on the following paper: M. Abdelfattah, M. Hickle, M. D. Sinanis, Y. Wu and D. Peroulis, "A 12 –

20 GHz Passively-compensated Tunable Bandstop Filter with 40-dB Notch Level," *IEEE/MTT-S International Microwave Symposium – IMS*, Philadelphia, PA, 2018, pp. 571-574. The author's contribution in this chapter include the analysis, design, fabrication, assembly and measurements of Filter B.

2.2 Filter Design

Both filters are implemented using silicon micro-machined cavity resonators with electro-statically actuated MEMS membranes. The exploded 3-D views of both filters are shown in Fig.2.1. Each filter is comprised of four main parts: the MEMS tuner, the EVA-mode cavity substrate, the RF signal substrate and the launch board for the coaxial connectors. Although both filters has similar structures, the dimensions were scaled and optimized for the specific frequency range of each filter. As a result, different substrate thicknesses and dimensions were used. The filters were simulated using ANSYS High Frequency Structure Simulator (HFSS).

2.2.1 Constant ABW QABS Filter Topology

The topology of the passively-compensated QABS filter is shown in Fig. 2.2. It is based on a two-resonator hybrid-coupler topology, as in Fig. 1.2, with two external coupling elements per resonator instead of one. As shown in the figure, there are two solutions that yield a theoretically-infinite notch level (absorptive notch, AN). The first solution requires a 90° through line and can yield nearly CABW over an octave TR [13]. While this solution is ideal for low frequencies, it becomes challenging beyond 10 GHz as a 90° through line becomes impractically short in this range. Consequently, in this work, we opt for the second possible solution that requires a 270° through line. The sections below outline how the challenges associated with this choice are addressed.

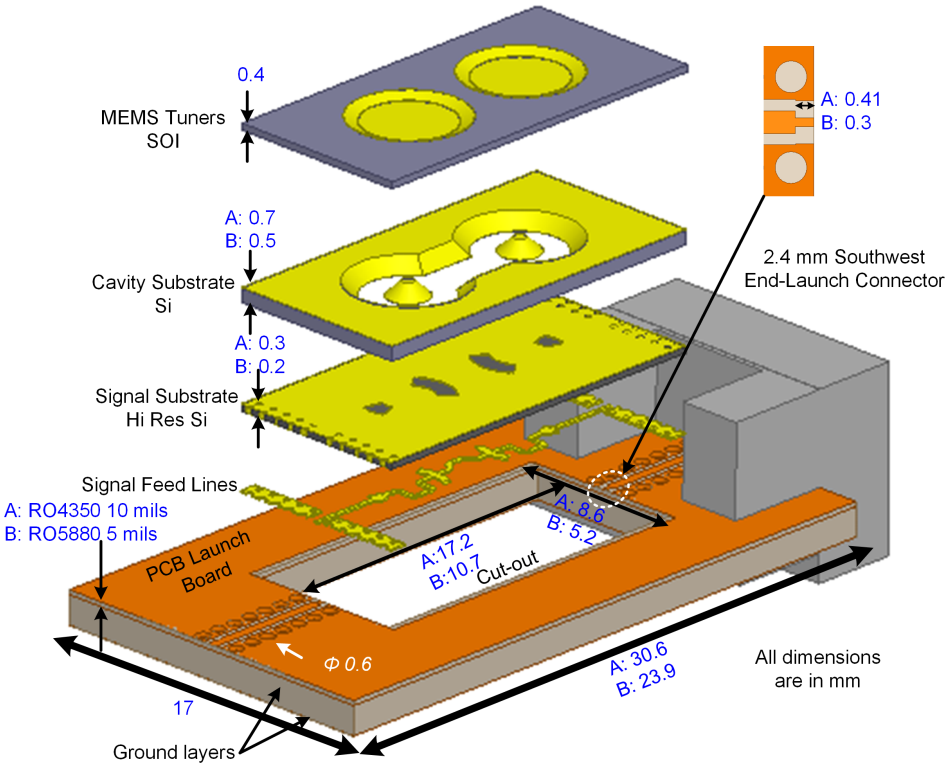

Fig. 2.1.: Exploded view of connectorized silicon micro-machined cavity filter, A denotes Filter A and B denotes Filter B.

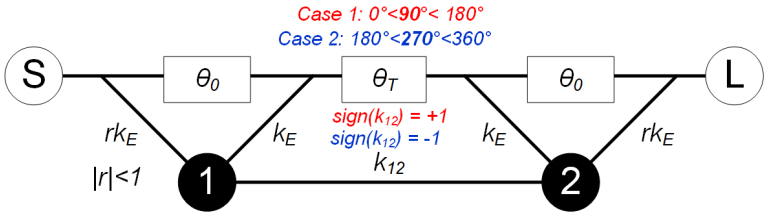

Fig. 2.2.: Coupling topology for constant BW QABS filter.

Constant ABW

The external coupling dominates the filter's BW variation. The purpose, therefore, of the doubly-coupled resonator scheme is to manipulate the external coupling frequency dependence over the needed TR [13]. As shown in (2.1), the equivalent external coupling to the resonator, k_E^*, depends on the coupling ratio, r, the trans-

mission line length, θ_0, and the main coupling element value, k_E. Hence, we have several degrees of freedom to control the external coupling and bandwidth variations. It should be noted that this coupling scheme also modifies the through line electrical length as shown in (2.2) where θ_T^* is the effective through-line electrical length. This modification potentially results with a positive impact on the AN frequency range as will be shown later.

$$k_E^* = k_E\sqrt{1 + r^2 + 2r\cos(\theta_0)} \tag{2.1}$$

$$\theta_T^* = \theta_T + \Big(\pi - arg\Big(\frac{1 + re^{-j\theta_0}}{1 + re^{j\theta_0}}\Big)\Big) \tag{2.2}$$

The effects of the coupling parameters (r and θ_0) are studied in Fig. 2.3 to illustrate the available control over the external coupling variation and the through line electrical length. In this study, the single-element external coupling k_E is assumed to double over an octave TR. To validate the effectiveness of the proposed topology, both parameters r and θ_0 are optimized to minimize the 3-dB ABW over an octave TR. As a result, the 3-dB ABW variation is reduced from 732% to 32% as shown in Fig. 2.4.

AN Frequency Range

An additional important advantage of the presented topology is that it achieves an AN over a wide range by slightly detuning the resonant frequency of the two resonators. In order to achieve an AN, the condition on k_E^* shown in (2.3) must be satisfied [18]. The minimum required external coupling, $k_{E,min}^*$, depends on the resonator unloaded Q_u, the inter-resonator coupling, k_{12}, and θ_T^*. As a result, the parameters r and θ_0 should be carefully selected to guarantee in a wide AN frequency range.

$$k_E^* \geq k_{E,min}^* = \sqrt{\frac{Q_u^{-2} + k_{12}^2}{k_{12}\sin(\theta_T^*)}} \tag{2.3}$$

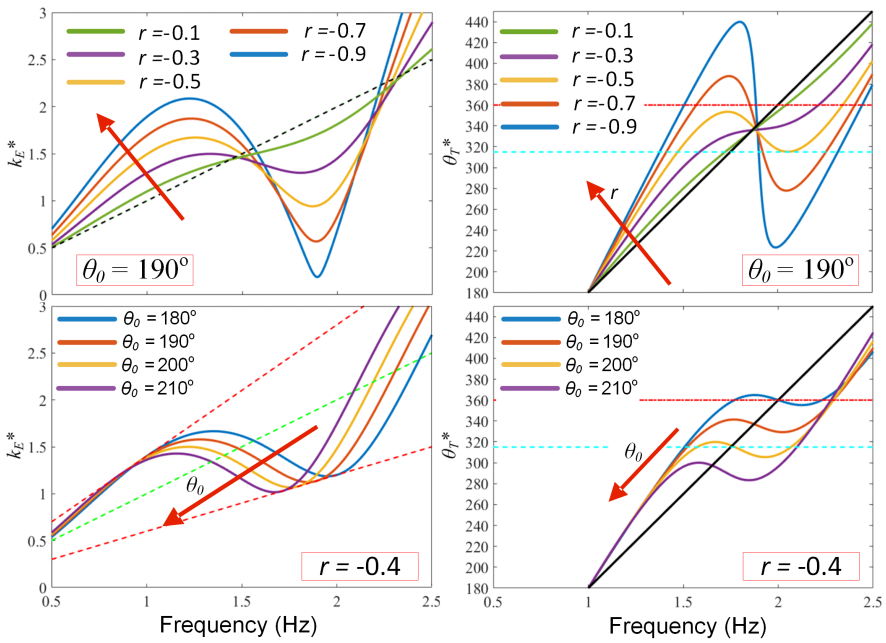

Fig. 2.3.: The effect of r and θ_0 on k_E^* and θ_T^*.

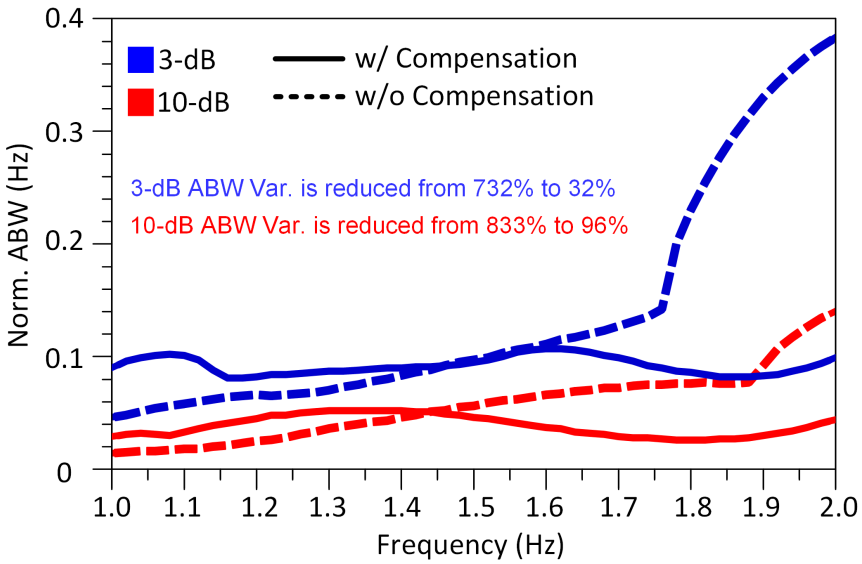

Fig. 2.4.: ABW variation improvement with optimized coupling parameters, $r = -0.42$, $\theta_0(1\text{ Hz}) = 192^o$ and $k_E(1\text{ Hz}) = 0.2$.

Considering the condition in (2.3), it can be shown that achieving a wide AN frequency range is more challenging when θ_T is centered around 270° as opposed to

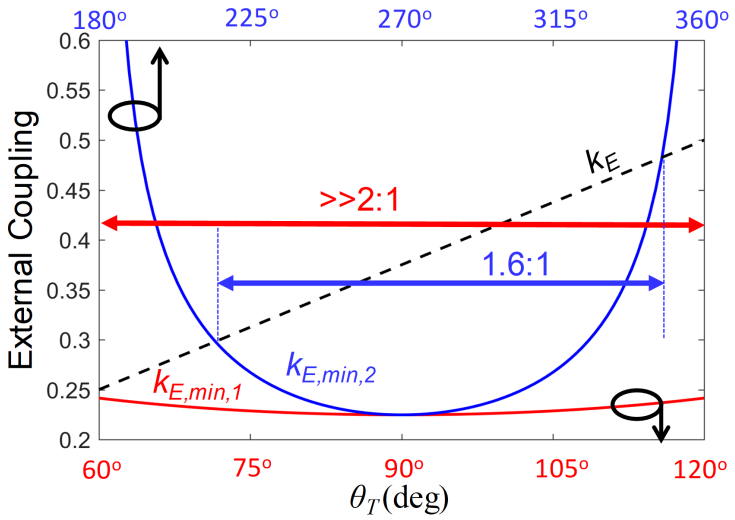

Fig. 2.5.: Achievable AN frequency range with $r = 0$ for two cases of θ_T.

90°. To illustrate, Fig. 2.5 shows an example of the achievable AN frequency range with linearly increasing k_E when $r = 0$ and $\theta_0 = 0^o$. Therefore, the AN frequency range is an added challenge specifically facing the high-frequency implementations of these filters.

As previously mentioned the proposed coupling topology could potentially improve the AN frequency range. This is mainly due to the fact that this topology results in θ_T^* which is not linearly dependent on frequency as shown in Fig. 2.3. As a result, the coupling parameter values could either decrease or increase the AN frequency range. This is demonstrated in Fig. 2.6 for different cases of the coupling parameters. It is shown in Fig. 2.6(c) that only with optimized coupling parameters the AN frequency range is larger than an octave which is not theoretically possible without the double-coupling scheme .

2.2.2 Silicon Micro-machined EVA Mode Cavity Design

The topology in Fig. 2.2 is realized using silicon micro-machined EVA-mode cavities. The cavities are tuned using electro-statically actuated micro-corrugated di-

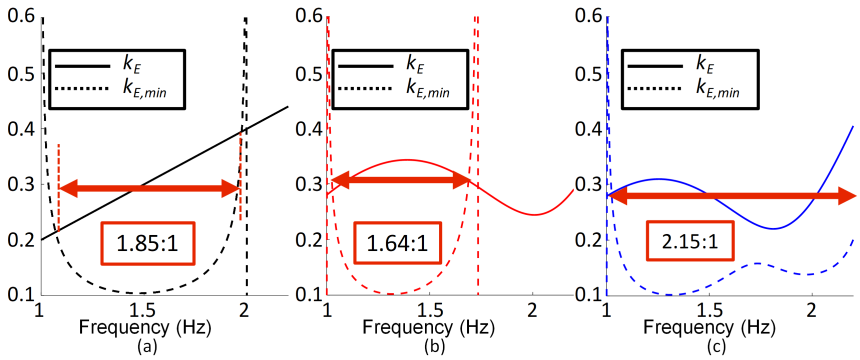

Fig. 2.6.: Achievable AN frequency range for different cases (a) $r = 0$ (b) non-optimized coupling parameters $r = -0.5$, $\theta_0(1\text{ Hz}) = 180^o$ and $k_E(1\text{ Hz}) = 0.2$ (c) optimized coupling parameters $r = -0.42$, $\theta_0(1\text{ Hz}) = 192^o$ and $k_E(1\text{ Hz}) = 0.2$.

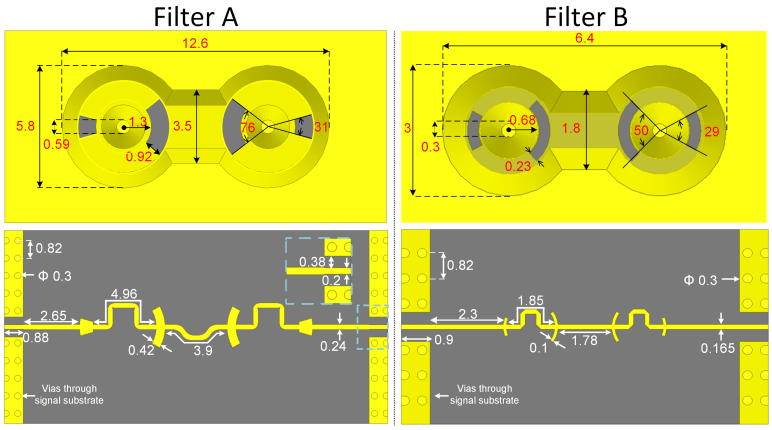

Fig. 2.7.: Dimensions of designed silicon cavity filter in millimeters.

aphragms on top of their posts. The inter-resonator coupling (k_{12}) is realized by the coupling iris which achieves the negative polarity required by this topology. The external couplings (k_E, rk_E) are realized via the large and small coupling apertures etched at the bottom of each cavity. The through transmission line is placed on a second high-resistivity silicon substrate at the bottom of the cavity substrate. Fig. 2.7 shows all important dimensions of the top side of the cavities as well as the transmission line on the back for both designed filters.

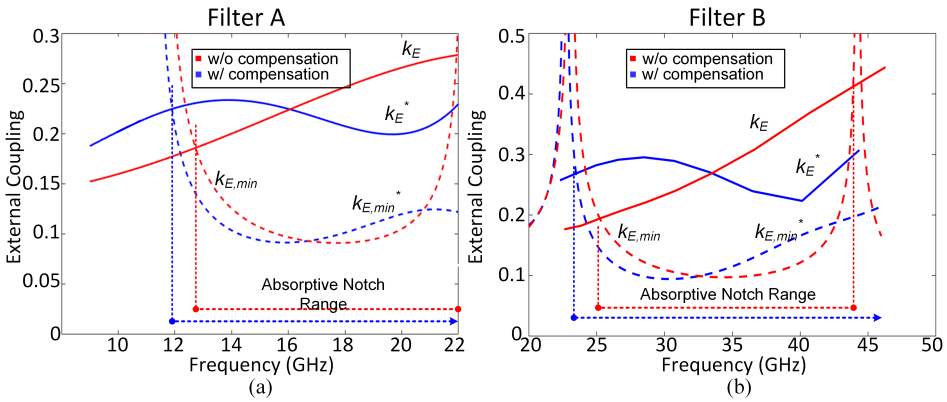

Fig. 2.8.: k_E^* and $k_{E,min}^*$ for (a) Filter A (b) Filter B.

Fig. 2.8 shows the simulated frequency dependence of the individual and total external couplings for both filters. While k_E grows linearly with frequency, k_E^* exhibits a sinusoid-like variation. In addition, Fig. 2.8 shows the curves for k_E^* and $k_{E,min}^*$ for both cases; with and without bandwidth compensation. It can be seen that for both filters, the AN frequency range is increased when using the bandwidth compensation topology due to the non-linear frequency dependence exhibited by θ_T^*.

2.2.3 Connectorized Design

Both filters are designed to have a 2.4 mm coaxial interface. A printed circuit board (PCB) is designed to be attached to a Southwest end-launch connector as shown in Fig. 2.1. The board is constructed of two layers; a thin top layer for signal propagation and a thick bottom layer for physical support. The structure contains two transitions for the RF feed. First, from the end-launch connector to a grounded coplanar waveguide (GCPW) on the board. Second, a flip chip transition from the board to the silicon signal substrate on the filter. Finally, on the silicon substrate from GCPW to microstip line which couples to the cavity resonators.

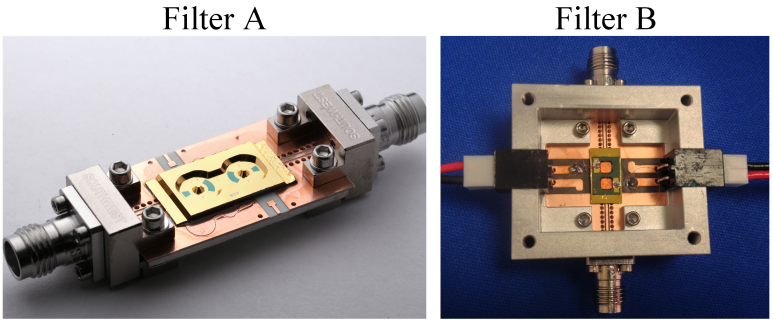

Fig. 2.9.: Pictures of the manufactured filters (a) Filter A after attachment to the connectorized launch board before the attachment of the MEMS tuners (b) Filter B in a full packaged housing after full assembly.

2.3 Measured Results

The filters have been fabricated at the Birck Nanotechnology Center, Purdue University. Pictures of the manufactured filters are shown in Fig. 2.9. The filters were measured using an Agilent Tech E8261A network analyzer. Filter A is tuned from 9-20 GHz and the measured response is shown in Fig. 2.10(a). The notch rejection is better than 20 dB over the full TR, and better than 40 dB from 12-20 GHz. The out-of-band IL is 1.3-2.5 dB. The measured response for Filter B is shown in Fig. 2.10(b). The notch is tunable from 23-45 GHz with a notch depth between 30-50 dB. The required DC bias voltage to tune the MEMS diaphragms is less than 100 V.

The measured and simulated filter BW are shown in Fig. 2.11. For Filter A, the measured 3-dB and 10-dB ABW variation are 48% (402-595 MHz) and 71.6% (155-266 MHz), respectively, over the range 12-20 GHz. Compared to the uncompensated BW variation, the 3-dB and 10-dB BW variations are reduced by about 4×. Over a 25.2% TR, the measured 3-dB ABW variation is 12.5% (432-486 MHz) and the 10-dB ABW variation is 21.5% (219-266 MHz). For Filter B, the measured 3-dB and 10-dB ABW variation are 40% (1.41-1.97 GHz) and 129% (0.44-1.01 GHz), respectively over

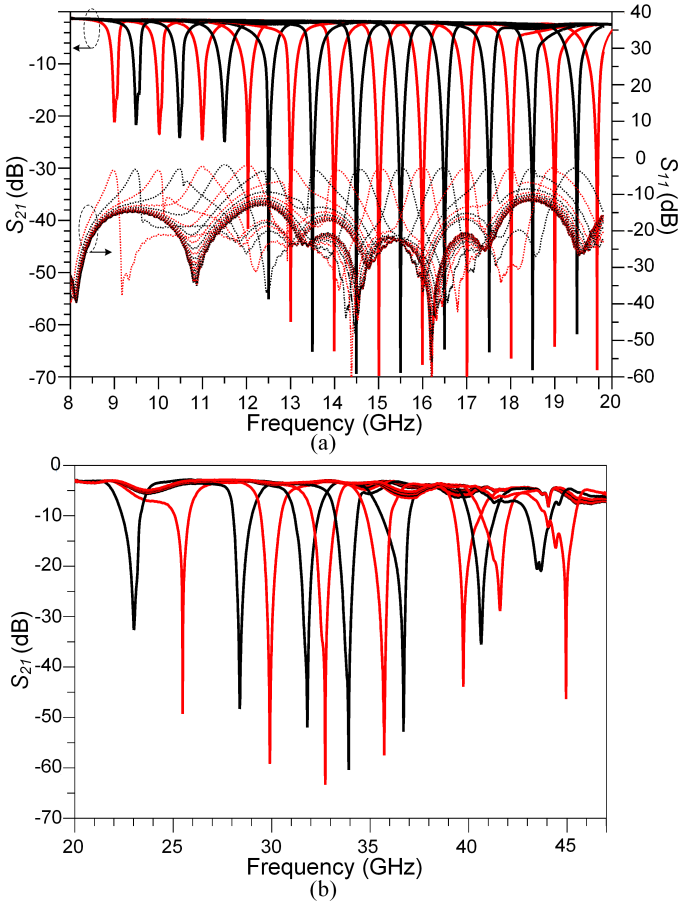

Fig. 2.10.: Measurements of filter response at different tuning states (a) Filter A (b) Filter B.

the full range 25-45 GHz. Compared to the uncompensated BW variation, the 3-dB BW variations is reduced by about 9.5×.

2.4 Conclusion

This work presented the design and implementation of connectorized, high rejection, passively-compensated, bandstop filters. The filters are fabricated with silicon micro-machined EVA-mode cavity resonators. The filters demonstrate low ABW variation and high rejection that exceeds 40 dB.

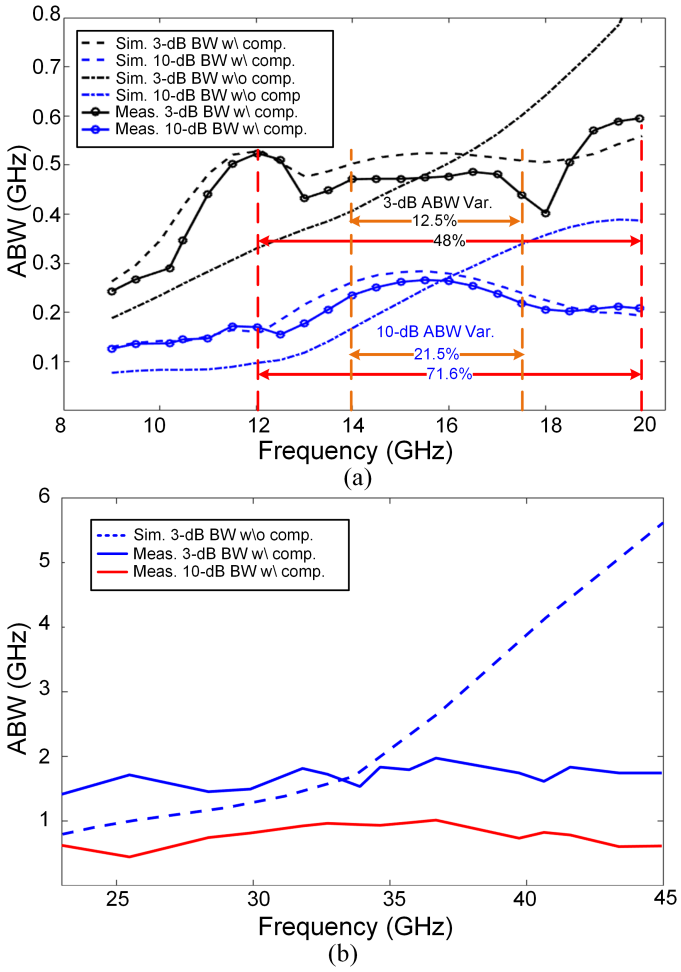

Fig. 2.11.: Measured and simulated 3-dB and 10-dB ABW with and without BW compensation (a) Filter A (b) Filter B.

3. MONITORING AND CONTROL OF MEMS TUNABLE FILTERS USING INDUCTIVE PROXIMITY SENSING

3.1 Introduction

Tunable cavity-based RF and microwave filters are essential for adaptive wireless systems due to their superior performance in terms of loss, tuning range, and linearity compared to alternative technologies [19–22]. In addition, recent advances in silicon-based evanescent-mode cavity filters cover frequencies in the 10–100 GHz range [15, 22, 23], allowing efficient use of those bands. Since evanescent-mode cavity filters are mechanically tuned by bending a flexible membrane, they might be vulnerable to non-ideal effects such as long-term deformation (creep) and hysteresis, in addition to fabrication nonidealities. As a result, achieving long-term, reliable and repeatable tuning with such filters has been a focus in the literature.

Various types of electric motors have been used as tuning actuators to resolve such filter tuning issues [22, 24, 25]. The motor feedback system can provide a repeatable sub-micron resolution. The size, cost, and power consumption of such devices, however, make them impractical for the majority of in-the-field adaptive applications. Alternative electronic approaches to monitor the resonators in a filter rely on sensing secondary modes of oscillation in the cavity [26], measuring the capacitance between the electrostatic actuator and the tuning membrane [27], or measuring reflected signals from the filter [28]. While these sensing methods are successful in monitoring the filters, the complexity of such methods require laboratory scale test equipment. The same applies to optical sensing techniques. The monitoring and control techniques presented by the authors in [29,30] rely on a stacked dual-cavity structure, where one cavity is in the RF filter and the other is used for monitoring. This allows monitoring and controlling the filter electronically and in real-time, without disturbing the RF

signal. As a result, this technique resolves the issues above faced by the alternative techniques. The employed dual-cavity structure, however, is primarily suitable for PCB fabricated cavities, which normally operate below 10 GHz. This monitoring structure is not easily implemented in miniature micro-machined silicon-based MEMS filters, used in frequencies above 10 GHz.

In this chapter we present a fully electronic monitoring and control system for electro-statically tunable MEMS cavity filters. The monitoring of the MEMS membrane is based on inductive proximity sensing for each cavity membrane in the filter, as a feedback. The sensing inductor doubles as the bias electrode, minimizing the presence of metallic objects in the vicinity of the magnetic field. The sensing method measures the absolute deflection of the MEMS membrane and, based on that, adjusts the MEMS dc bias voltage until the membrane is at the desired deflection, providing the required frequency response of the monitored resonator. The system is conceptually shown in Fig. 3.1. This chapter also provides the detailed analyses for the sensitivity, control loop, and the RF filter as well as the trade-offs in choosing the optimal inductance and the operating frequency, supported with measurements. In addition, repeatability and long-term performances are measured and analyzed. This system is demonstrated on a second order bandstop filter (BSF) operating in the 30–42 GHz mm-Wave range. Long-term measurements show that the filter notch frequency is maintained within the original 20 dB bandwidth throughout the test period, which was not possible with open-loop tuning (constant voltage). Tuning repeatability is also tested, and the presented control system can tune the filter with less than 1% error over 100 repetitions. The presented system consumes 0.88 W/resonator from a single 5 V source, of which 0.07 W/resonator are in the dc-dc converters, and 0.325 W/resonator are in the FPGA development board.

The text and figures presented in this chapter are based on the following paper: M. Abu Khater, M. Abdelfattah, M. D. Sinanis and D. Peroulis, "Monitoring and Control of MEMS Tunable Filters Using Inductive Proximity Sensing," in *IEEE Transactions on Microwave Theory and Techniques*, vol. 66, no. 12, pp. 5605-5613, Dec. 2018.

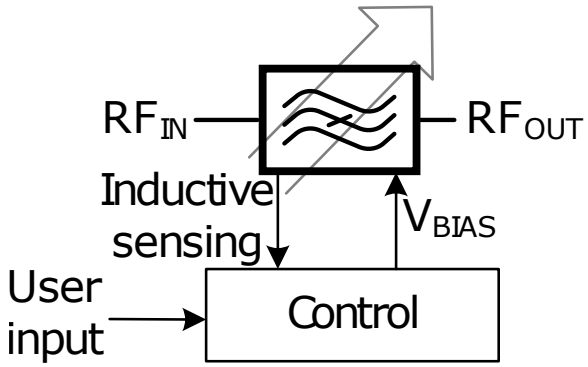

Fig. 3.1.: Inductive proximity sensing is used to monitor MEMS tunable filters. The monitoring is the feedback in a control loop, which tunes the filter to a desired frequency response based on an input from the user.

The author's contribution in this chapter include the analysis, design, fabrication, assembly and measurements of the demonstrated bandstop filter.

3.2 Monitoring Concepts and Optimizations

A schematic of the presented system is shown in Fig. 3.2(a). When a dc bias voltage (V_{BIAS}) is applied to the sensing inductor (L_{SPIRAL}), the MEMS membrane bends towards L_{SPIRAL}, which increases the resonant frequency of the RF cavity (due to a decrease in the loading capacitance). Also, this results in reducing the effective value of L_{SPIRAL} (due to the counteracting eddy currents in the membrane), which in turn increases the resonant frequency of the series LC circuit, where the capacitors C1 and C2 are fixed external components. The shift in the LC resonance frequency changes the amplitude response of the monitoring circuit, as discussed in Sec. 3.2.2. As a result, by measuring V_{SENSE} and relating it to the resonant frequency of the corresponding RF cavity, the filter response can be monitored. This monitoring information is used as feedback in a control system that can adjust the bias voltage V_{BIAS} until the desired RF response is achieved.

A spiral inductor is chosen due to its easily manufacturable planar structure. Additionally, because the spiral inductor covers most of the area above the membrane, it is operated as the MEMS bias electrode. The electric field due to dc biasing exerts sufficient electrostatic force on the membrane for actuation.

The circuit is driven by an ac source, referenced to a crystal oscillator. This aids in achieving a stable excitation, which is necessary in detecting the motion of thin membranes (typically 1 μm) with small deflection range (typically 10 μm).

3.2.1 Inductive Proximity Sensing

A circuit model for the monitoring structure is shown in Fig. 3.2(b). Fig. 3.2(c) shows the ac equivalent circuit. R_S is the output impedance of the ac source, and R_L is the effective resistance of the spiral inductor. L_{SH} and R_{SH} are the effective sheet inductance and resistance of the membrane, discussed in more detail later in this section.

The value of L_{SPIRAL} is calculated using [32]

$$L_{Spiral} = \frac{\mu_0 N^2}{(R_{out} - R_{in})^2} \times \int_0^{\pi} \int_{R_{in}}^{R_{out}} \int_{R_{in}}^{R_{out}} \frac{\cos(\theta) r_1 r_2 dr_1 dr_2 d\theta}{\sqrt{r_1^2 + r_2^2 - 2r_1 r_2 \cos(\theta)}}, \tag{3.1}$$

where μ_0 is the free space permeability, N is the number of turns, R_{in} and R_{out} are the inner and outer radii of the spiral structure, respectively.

Since the eddy currents in the membrane run in a circular fashion, and since the metal of the membrane has a finite resistance, the membrane can be modeled as an RL circuit as shown in Fig. 3.2(b) [33]. The effective inductance of the sheet membrane (L_{SH}) can be also calculated using (3.1), while multiplying it by 0.5 to accommodate for the absence of gaps between the tracks, and setting $N = 1$.

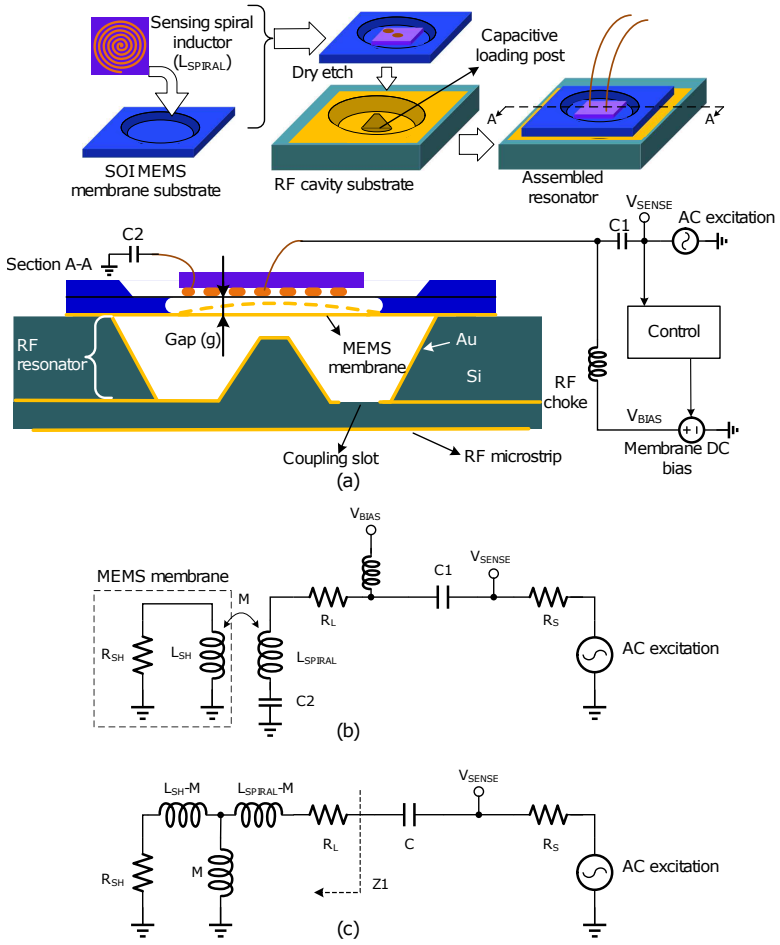

Fig. 3.2.: (a) A schematic structure of the inductive sensing method where a spiral inductor also functions as the biasing electrode, and the readout from the spiral is used as feedback to bias the MEMS membrane to a desired location [31]. (b) A circuit model for the inductive sensing in (a). (c) Equivalent ac circuit model of the circuit in (b).

When the spiral inductor is in close proximity to the metallic membrane, the mutual inductance between them can be calculated by [32]

$$M = \kappa(g)\sqrt{L_{SPIRAL}L_{SH}} = \frac{\mu_0 N}{(R_{out} - R_{in})R_{out}} \times \int_0^{\pi} \int_{R_{in}}^{R_{out}} \int_0^{R_{out}} \frac{\cos(\theta) r_1 r_2 dr_1 dr_2 d\theta}{\sqrt{g^2 + r_1^2 + r_2^2 - 2r_1 r_2 \cos(\theta)}}, \tag{3.2}$$

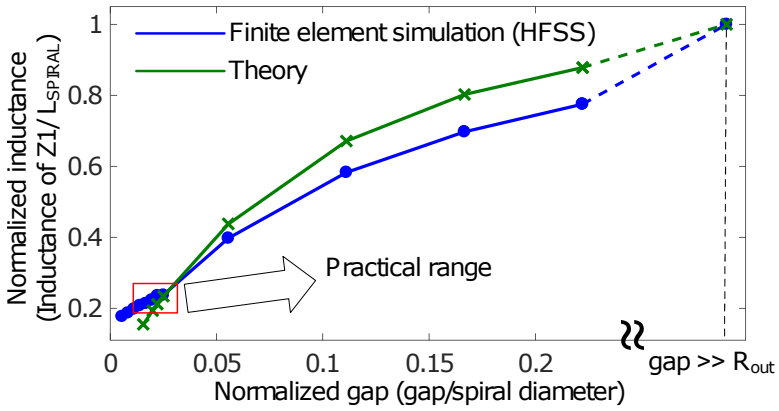

Fig. 3.3.: Simulated, and calculated equivalent inductance of $Z1$ versus the gap g.

where $\kappa(g)$ is the coupling coefficient as a functions of the gap between the spiral inductor and the membrane, shown in Fig. 3.2(a).

To evaluate the resultant effective inductance of $Z1$ (at the terminals of the spiral), shown in Fig. 3.2(c), as a function of the gap g, the circuit is analyzed with (3.1) and (3.2) evaluated numerically. The details of the circuit analysis are discussed in Section 3.2.2. The spiral inductor and the membrane structure is simulated using High Frequency Structure Simulator (HFSS) finite element solver. Fig. 3.3 shows the calculated and simulated sensed inductance (L at $Z1$) as a function of g. It is worth mentioning here that the practical range indicated in Fig. 3.3 is due to the fact that the the gap g is small (typically < 50 μm) compared to the bias electrodes (spiral inductor in this case, typically > 1000 μm).

3.2.2 Circuit Optimization

A change in the gap g (whether intentional due to a dc bias, or unintentional due to imperfections such as long-term creep) changes the effective value of the sensed inductance at $Z1$, which in turn affects the frequency response of the sensing node (V_{SENSE}). The circuit model in Fig. 3.2(c) is analyzed and each parameter in the circuit is optimized to improve the sensitivity of the circuit to changes in g.

The sensitivity of the circuit primarily depends on how much $Z1$ changes per unit change in g. To simplify the analysis, an impedance sensitivity is defined as

$$\begin{aligned} ImpedanceSensitivity &= \left|\frac{\partial Z1}{\partial g}\right| \\ &= \left|\frac{\partial M}{\partial g} \times \frac{\partial Z1}{\partial M}\right|. \end{aligned} \tag{3.3}$$

In order to maximize the sensitivity, each term in (3.3) is maximized separately.

To optimize the contribution of the first term in (3.3), $\frac{\partial M}{\partial g}$ is evaluated from (3.2)

$$\begin{aligned} \frac{\partial M}{\partial g} = \frac{\mu_0 N}{(R_{out} - R_{in})R_{out}} \times \\ \int_0^{\pi} \int_{R_{in}}^{R_{out}} \int_0^{R_{out}} \frac{-g\cos(\theta) r_1 r_2 dr_1 dr_2 d\theta}{(g^2 + r_1^2 + r_2^2 - 2r_1 r_2 \cos(\theta))^{\frac{3}{2}}}. \end{aligned} \tag{3.4}$$

As can be seen from (3.4), the sensitivity of the mutual inductance to the gap can be improved by decreasing g. Decreasing g arbitrarily, however, can limit the tuning range, and can complicate the fabrication process. Also, increasing the number of turns N, and decreasing $(R_{out} - R_{in})$ can further increase $\frac{\partial M}{\partial g}$. On the other hand, these changes may require small feature dimensions that complicate the fabrication of the spiral inductor.

To optimize the contribution of the second term in (3.3), $Z1$ is found by analyzing the circuit shown in Fig. 3.2(c) as

$$Z1 = R_L + j\omega L_{SPIRAL} + \frac{\omega^2 M^2}{R_{SH} + j\omega L_{SH}}, \tag{3.5}$$

where ω is the operating angular frequency of the ac excitation. From (3.5), we get

$$\frac{\partial Z1}{\partial M} = \frac{2\omega^2 M}{R_{SH} + j\omega L_{SH}} = \frac{2\omega^2 \kappa \sqrt{L_{SPIRAL} L_{SH}}}{R_{SH} + j\omega L_{SH}}. \tag{3.6}$$

From (3.6), it can be seen that the sensitivity can be improved by increasing the mutual inductance. This can be achieved by increasing the coupling coefficient and by increasing L_{SPIRAL}, which is consistent with the conclusions drawn from (3.4). Increasing the operating frequency is also an efficient way to increase the sensitivity, as long as the frequency is below the self-resonant frequency of the spiral inductor.

While reducing sheet resistance and inductance of the membrane, R_{SH} and L_{SH}, by increasing the metal thickness improves the sensitivity, it might result in a much higher actuation voltage to bend the membrane. As a result, R_{SH} and L_{SH} are typically dictated by the MEMS design and fabrication process.

For further circuit optimizations, the sensing voltage V_{SENSE} is evaluated. V_{SENSE} is found by analyzing the circuit in Fig. 3.2(c), resulting in

$$V_{SENSE} = V_{IN}\left(1 - \frac{j\omega C R_S}{1 + j\omega C R_S + j\omega C Z1}\right). \tag{3.7}$$

Due to the complexity of the expressions in (3.7) and (3.5), the effect of each design parameter might not be obvious. As a result, the amplitude of V_{SENSE} is evaluated numerically and verified with SPICE simulations. Fig. 3.4 shows the effect of each design parameter on $|V_{SENSE}|$.

As shown in Fig. 3.4(a), when driving the circuit at a frequency where V_{SENSE} has the highest slope ($\left|\frac{\partial V_{SENSE}}{\partial \omega}\right|$), the voltage sensitivity to a change in g is maximized. In other words, if the circuit is operating at the maximum slope frequency, and the gap g changes, the resonant frequency shifts, causing the maximum change in V_{SENSE}. The evaluation of (3.7) shows that the maximum slope occurs just below the resonant frequency as shown in the figure. It is important here to realize that, since a MEMS membrane deflection is typically very small (10–20 μm) compared to the size of the actuating inductor, the deviation in the frequency of maximum slope is also small. As a result, a linear approximation of the maximum slope region is used across the tuning range.

It should also be noted here that choosing the frequency of the highest slope in V_{SENSE} does not contradict the requirement of choosing high frequency as concluded from (3.6). To satisfy both conditions, the frequency of highest slope should be placed as high as possible by reducing C. The effect of reducing C, or increasing L_{SPIRAL}, which improves the sensitivity, is shown in Fig. 3.4(b).

The effect of the spiral resistance (R_L) is shown in Fig. 3.4(c). Lower inductor resistance causes a sharper frequency response, resulting in a better voltage sensitivity.

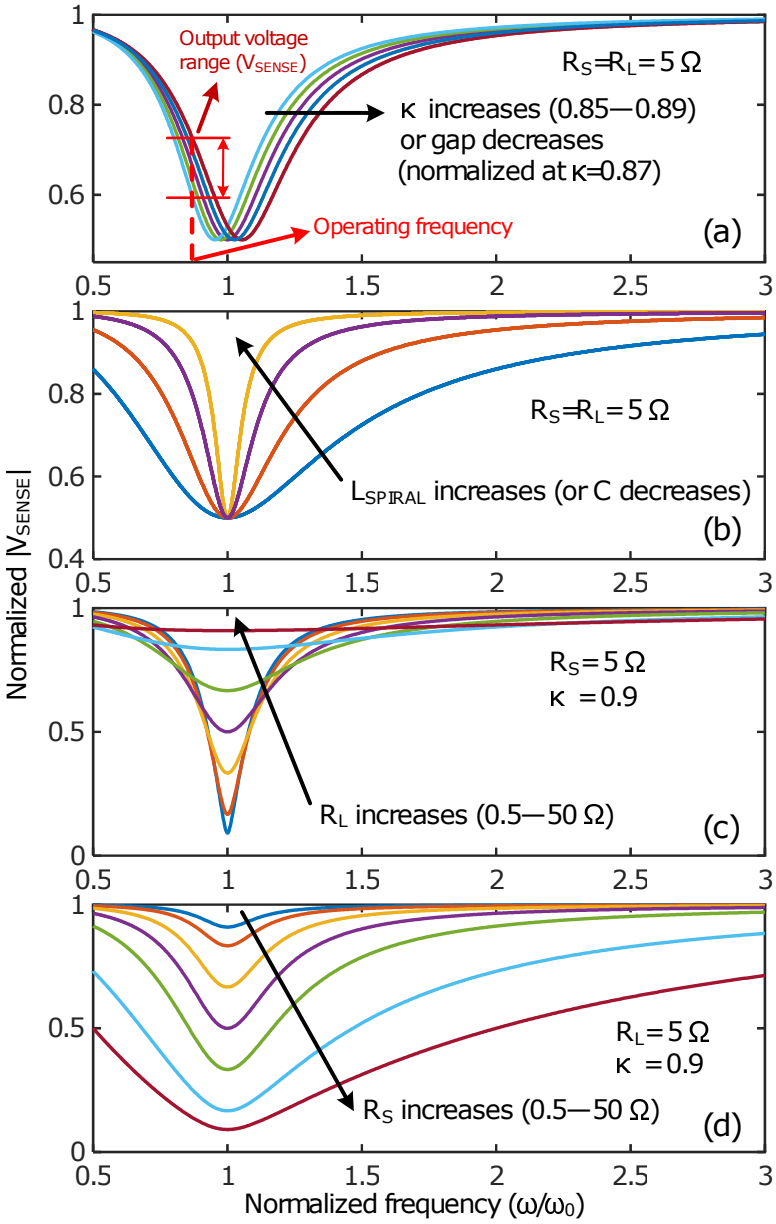

Fig. 3.4.: The amplitude of V_{SENSE} versus frequency and how it is affected by: (a) The coupling coefficient (or the gap), (b) the spiral inductance and the external capacitance, (c) the inductor resistance R_L, and (d) the source resistance R_S.

In order to reduce R_L, the spiral inductor should be fabricated with thick metal on a high-quality substrate.

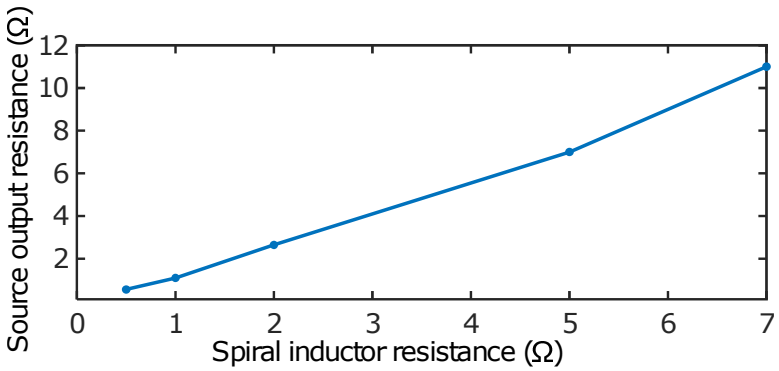

Fig. 3.5.: For each value of the inductor resistance R_L, there is a specific value for the source resistance R_S such that the sensitivity is maximized.

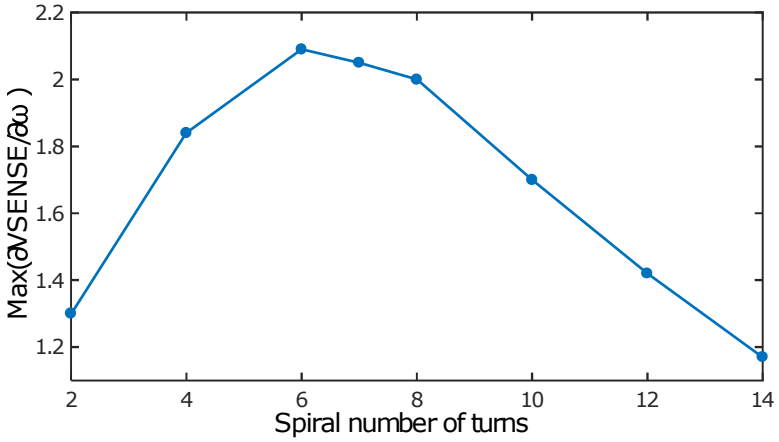

Fig. 3.6.: The tradeoff between the number of turns in the spiral inductor and its effect on the sensitivity of the inductive monitoring.

If the design process enables controlling the source impedance (R_S), its value can further optimize the sensitivity, as plotted in Fig. 3.4(d). When $R_S \ll R_L$ or $R_S \gg R_L$, the output shows no significant slope near the resonant frequency. As a result, for each R_L, there is an optimal value for R_S that produces the highest sensitivity. The optimal value of R_S can be found numerically by sweeping its value and calculating the maximum slopes of the curves in Fig. 3.4(d) for a given value of and R_L. An example of the relationship between R_L and optimal R_S is shown in Fig. 3.5.

3.2.3 Spiral Inductor

The analysis in Section 3.2.2 assumes the general case where L_{SPIRAL} and R_L can vary independently. In realistic implementations, however, a higher inductance typically results in a higher R_L. The increase in L_{SPIRAL} and the increase in R_L have opposite effects on the sensitivity. As a result, a tradeoff exists when using a spiral inductor.

Fig. 3.6 shows the normalized highest slope on the amplitude of V_{SENSE}, versus the number of turns in the spiral inductor. Since R_{in} and R_{out} are kept constants (1700 μm and 2000 μm, respectively, which fits the MEMS design), the tracks are fitted to the same area by reducing the track width and the spacing between the tracks. As shown in Fig. 3.6, our design results in highest voltage sensitivity when the spiral inductor has six or seven turns.

3.3 Control System Design

The control loop utilizes the monitoring system from Section 3.2 for feedback to ensure that the MEMS membrane sheet is at the desired deflection, which results in the desired filter frequency response. A separate independent control loop is applied to each resonator in the filter.

The control loop, shown in Fig. 3.7(a), takes a digital input from the user, and compares it to a digitized version of V_{DETECT}, which is the measure of the amplitude of V_{SENSE}. The digitization is done using an Analog to Digital Converter (ADC). The user input is based on a pre-calibrated look-up table. This comparison determines whether the deflection of the membrane is too high or too low. Then, using an integrator and a Digital to Analog Converter (DAC), a low voltage replica of V_{BIAS} is increased or decreased to correct the position of the membrane. A dc-dc converter boosts this voltage to generate V_{BIAS}, which is sufficiently high for MEMS actuation. The change in the deflection is detected using the inductive monitoring system, resulting in a change in V_{SENSE}, and thus closing the control loop.

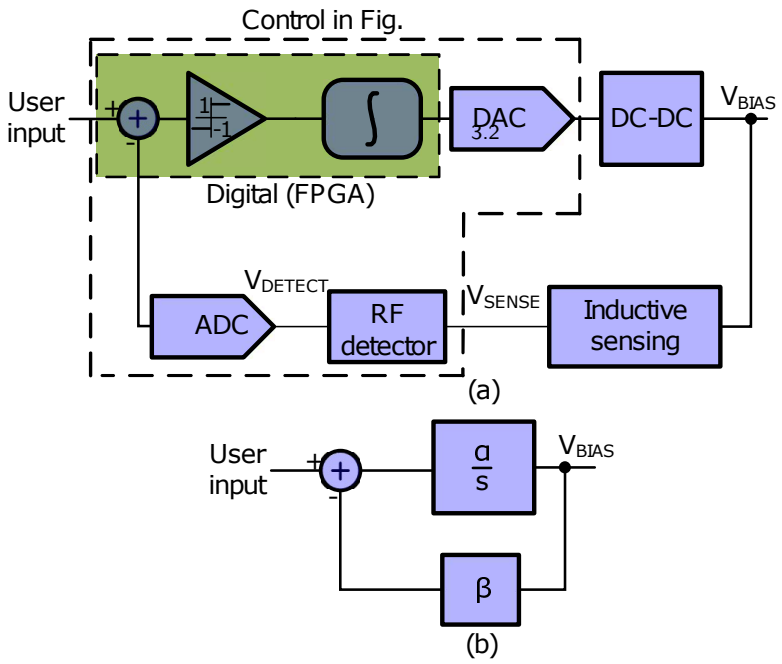

Fig. 3.7.: (a) A block diagram of the presented monitoring and control system, and (b) a linearized and simplified block diagram of the control loop in (a).

Fig. 3.7(b) shows a linearized and simplified model of the control loop, which can be analyzed for stability. The describing function method is used for the linearization [30, 34]. The transfer function of this control loop is given by

$$H(s) = \frac{\alpha}{s + \alpha\beta}, \tag{3.8}$$

where α and β are positive scalars resembling the forward and feedback path gains, respectively. $H(s)$ has a single pole in the left hand plane (at $-\alpha\beta$), which denotes that the system is unconditionally stable for bounded inputs.

3.4 Testbed Filter Design

3.4.1 Filter Topology

A quasi-absorptive BSF, covering the frequency range 30–42 GHz, is used to demonstrate the functionality of the control loop. The filter is designed based on

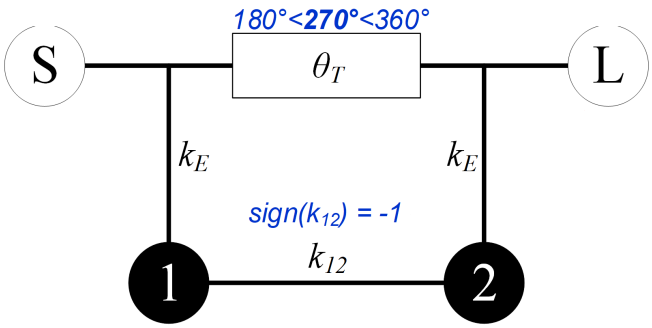

Fig. 3.8.: Coupling diagram for the absorptive BSF topology used to demonstrate the control system.

the quasi-absorptive topology shown in Fig. 3.8. Unlike conventional reflective band-stop filter topology, this topology employs additional inter-resonator coupling (k_{12}) between the resonators, creating two signal paths which can result in destructive interference [18]. This interference enables the filter to achieve a high-rejection notch regardless of the unloaded quality factor (Qu) of the resonators. An absorptive notch is achieved by satisfying the condition [18]

$$\frac{1}{Q_u^2} + B^2 + k_{12}^2 - k_{12}k_E^2 \sin(\theta_t) = 0, \tag{3.9}$$

where k_E is the external coupling to the cavities, θ_t is the electrical length of the transmission line, and B represents the detuning between the two resonators required to satisfy the condition.

3.4.2 Evanescent-Mode Filter Structure

The filter topology is implemented using silicon micro-machined cavity resonators. These cavity resonators have high-Q which increases the absorptive tuning range while reducing the notch bandwidth [18].

In this work, the through transmission line is realized using a microstrip line on a high-resistivity silicon, bonded to the bottom of the substrate of the cavities as shown in Fig. 3.2(a). The coupling between the microstrip line and the resonators is realized

using coupling slots etched on the bottom of the cavities. The electrical length of the transmission line between the two slots is designed to be 270° at the center frequency of the tuning range. Inter-resonator coupling is realized using a coupling iris between the two cavities. Coupling through the iris results in negative polarity coupling, which is required to satisfy the absorptive notch condition in (3.9). The resonant frequency of each cavity resonator depends on the capacitive gap between the loading post and the cavity membrane, which is complimentary to the sensed gap g [Fig. 3.2(a)].

3.5 Implementation and Measurements

3.5.1 Fabrication

The spiral inductors are fabricated using a PCB fabrication process on a 4-mil thick 370HR substrate, with 8.9 μm thick copper. The spiral inductor has seven turns, and the measured L_{SPIRAL} is 42 nH compared to the simulated 51 nH, with discrepancy due to fabrication and simulation modeling errors.

The MEMS membrane and the filter cavities are fabricated on silicon substrate in a process similar to the one in [15], with the exception that each biasing electrode is replaced with a spiral inductor as shown in Fig. 3.9(a). The spiral inductors are glued to the MEMS substrate. The gold membrane is 1 μm thick, and has 5 μm deep corrugations to improve the stability and reduce the required actuation voltage. The membrane is released using XeF_2 dry etching. Small holes (5 μm in radius) are etched in the gold membrane to provide access for the etchant to remove the silicon layer beneath it. The MEMS membrane substrate is then attached on the cavity substrate to form the BSF.

The BSF is placed on a connectorized PCB board to simplify testing. The connectors are 2.4 mm end launch from Southwest. The connectorized filter structure is shown in Fig. 3.9(b).

The connectorized filter is then attached to the inductive sensing and control board as shown in Fig. 3.9(c). The inductive sensing and control PCB is fabricated

on a 4-layer, 62 mil thick Rogers 4350B substrate. The spiral inductors' terminals are attached to the monitoring circuits and are driven by the ac signal and the bias signal. The ac signal is generated by an FPGA and an operational amplifier, which is used for conditioning and harmonics filtering. The components used to realize the control system in Fig. 3.7 are summarized in Table 3.1.

The system runs from a single 5 V power supply and consumes a total of 350 mA for the control of both resonators. Of which, 130 mA is consumed in the FPGA development board, and 28 mA in the dc-dc converters. Since most of the monitoring and control components are electronic, embedding the system in an on-chip solution with high efficiency charge-pumps [35], can significantly reduce the power consumption.

Table 3.1.: List of components used in the monitoring and control

DAC	DAC8565	ADC	ADS8353
FPGA	Altera Cyclone IV	RF power sensor	LTC5507
DC-DC	UMHV0505	Conditioning Opamp	MAX4203
C1, C2	47 pF	RF choke	1.5 μH

3.5.2 Sensing Feedback

The inductive sensing blocks are measured separately to verify their operation. When the filter is attached to the PCB substrate, as shown in Fig. 3.9(b), the spiral inductor leads are connected to a Network Analyzer (NA) to measure the inductance versus the membrane bias voltage V_{BIAS}. This is the inductance of $Z1$ discussed in Section 3.2.1. Since increasing the bias voltage decreases the gap g, the inductance is expected to decrease, which is observed in the measurements in Fig. 3.10. The value of the inductance is then used to extract the value of the gap g from HFSS simulation results. The corresponding values of g are also plotted in Fig. 3.10.

With the filter connected to the sensing circuit as shown in Fig. 3.9(c), the output of the power detector V_{DETECT} measured across a range of excitation frequencies.

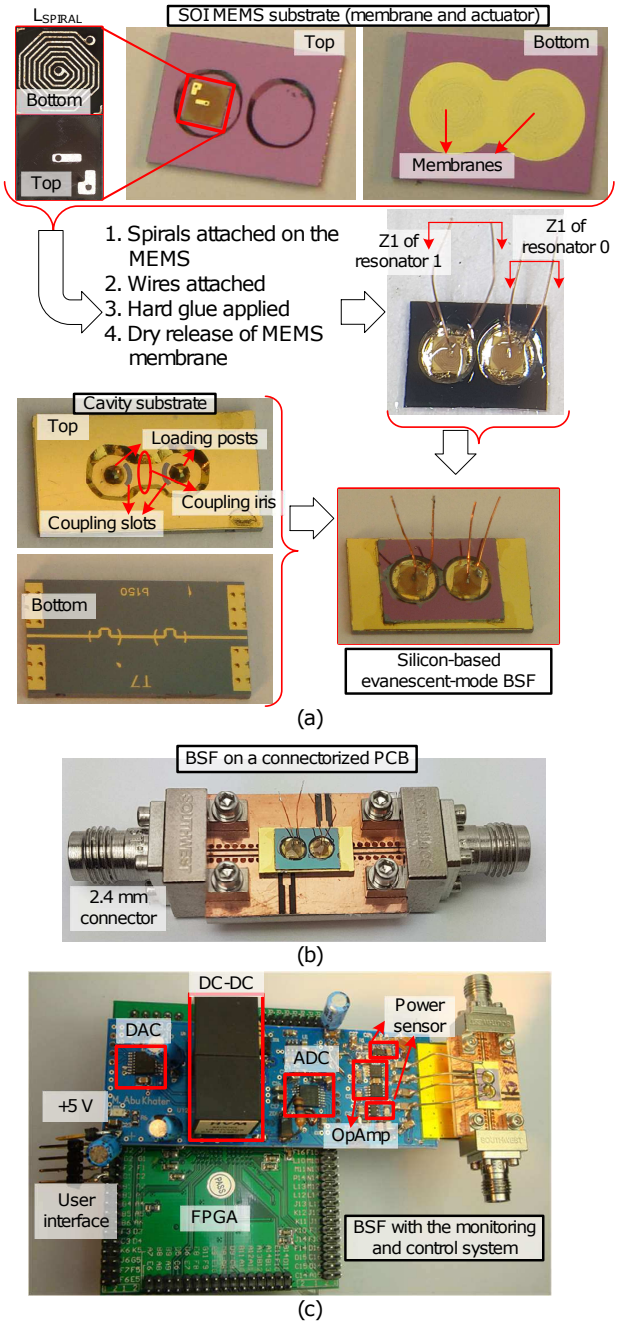

Fig. 3.9.: (a) The assembly process of the silicon-based RF MEMS filter with the monitoring spiral inductor. (b) The BSF is placed on a connectorized PCB to simplify RF testing. (c) The PCB of the filter attached to the rest of the monitoring and control system [31].

This measurement, shown in Fig. 3.11(a), is used to find the frequency of the highest sensitivity as discussed in Section 3.2.2. The fabricated inductive monitoring system shows highest sensitivity at 142 MHz, which is chosen as the ac monitoring frequency. While increasing this frequency, by decreasing C1 and C2, can improve the sensitivity, the values of the capacitors are chosen such that the operating frequency is well below the resonance of the spiral.

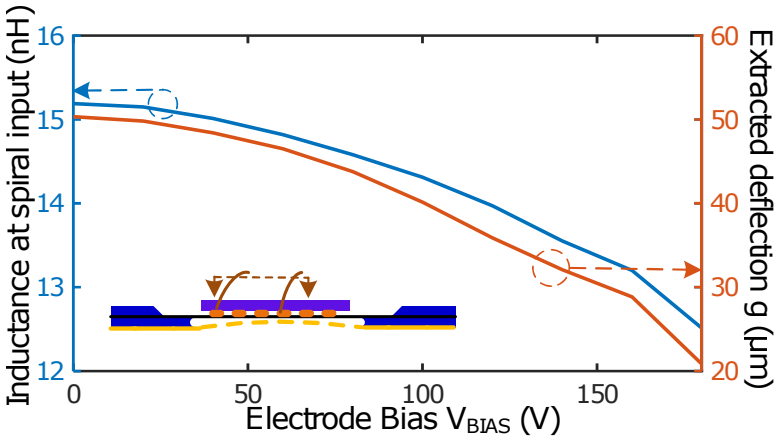

Fig. 3.10.: The measured sensed inductance at $Z1$ versus the bias voltage, and the membrane gap g is extracted from the simulated inductance values shown in Fig. 3.3.

Fig. 3.11(b) shows the change in V_{DETECT} versus the bias voltage. As shown in the figure, the majority of the sensing occurs when the bias voltage is above 50 V, which is consistent with the inductance measurement shown in Fig. 3.10. This measured range of V_{DETECT} dictates the operating sensing range. In other words, the user input should be the digital code for the voltage levels in this range. It should be noted that the measurement in Fig. 3.11(b) shows a monotonic relationship, which is necessary to sustain stable control.

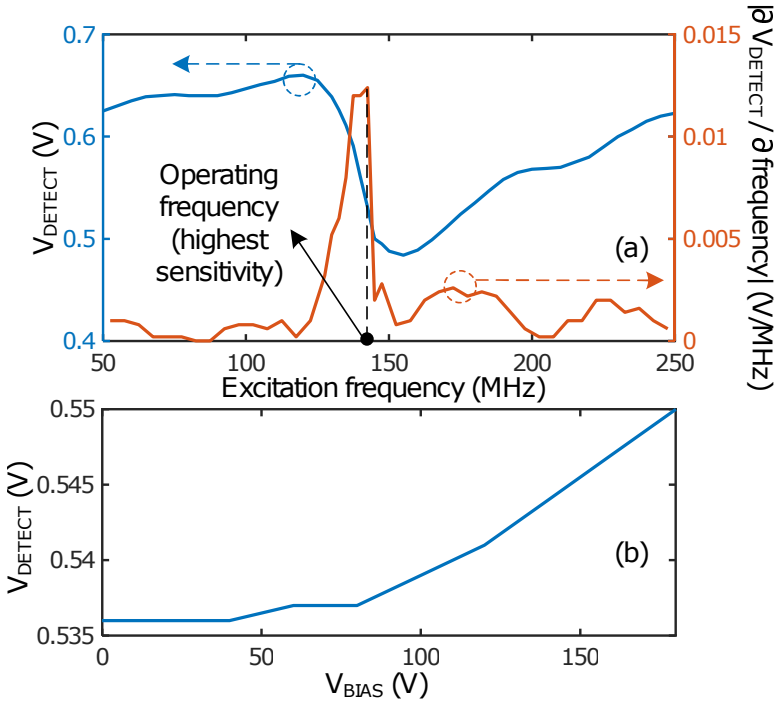

Fig. 3.11.: (a) The measured frequency response of V_{DETECT} and its derivative, which dictates the operating frequency. (b) The measured V_{DETECT} versus the bias voltage V_{BIAS}, with the system operating at the highest sensitivity frequency. This relationship is the readout of the inductive sensing.

3.5.3 Filter Monitoring and Control

With the filter assembled on the monitoring and control board, the user input is changed to get various RF responses. Fig. 3.12 shows the response of the RF filter, where the rejection frequency is tuned using the control loop. The filter is tuned within 30–42 GHz to maintain a rejection of 25–51 dB.

In order to test the repeatability of the monitoring and control system, the filter is tuned back and forth between two different frequencies one hundred times. The center frequencies are recorded for each tuning event. The results, shown in Fig. 3.13, show that the system can tune the filter with a maximum error of 1% (spread of 2%), which mostly falls within the 20 dB bandwidth of the target filter response.

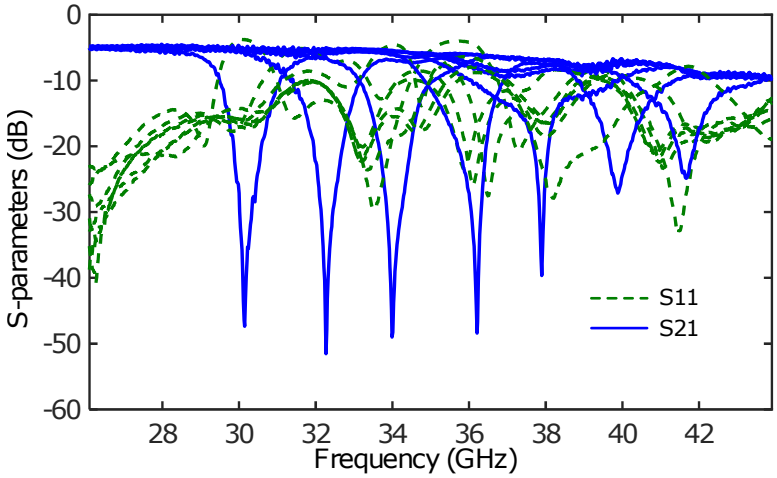

Fig. 3.12.: The monitoring and control system is used to tune the BSF notch to various frequencies [31].

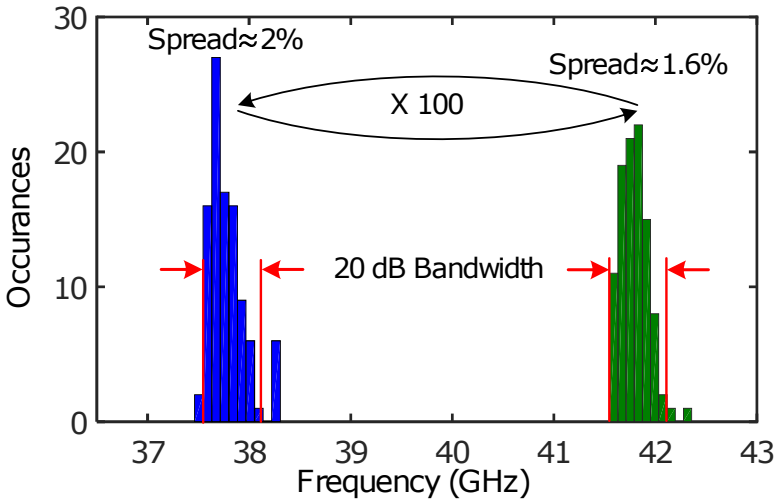

Fig. 3.13.: The filter is tuned between two different frequencies one hundred times, and maintains the center frequency within the 20 dB bandwidth of the filter.

The long-term performance of the presented work is also measured. First, the performance of the inductive monitoring is measured without the MEMS actuation. The sensing spiral and a 1 μm gold membrane are placed on opposite sides of a micrometer screw gauge as shown in Fig. 3.14. A ceramic insulating layer is used on the micrometer spindles to avoid the effect of its metal on the readings. The output

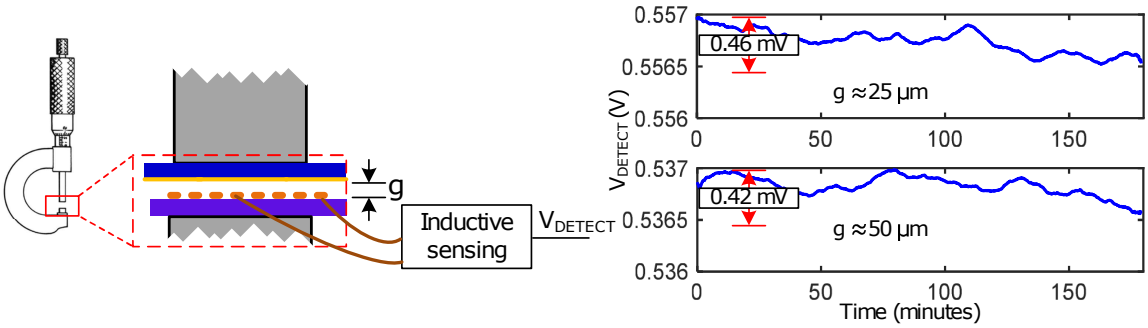

Fig. 3.14.: Schematic drawing for the long-term measurement setup of the inductive proximity sensing using a micrometer screw gauge (left), and the measured V_{DETECT} over 180 minutes showing no significant drift over time.

V_{DETECT} is recorded over 180 minutes (3 hours), also shown in Fig. 3.14, and shows no significant drift over time.

The fluctuations in the measured voltage, shown in Fig. 3.14, are primarily due to ambient temperature variations and mechanical vibrations. From the peak-to-peak fluctuation on V_{DETECT} ($V_{DETECT\ peak-to-peak}$), the average resolution of the system can be calculated by

$$Resolution_{Avg.} = \frac{V_{DETECT\ peak-to-peak}}{\Delta V_{DETECT}} \approx \pm 1.1\%, \tag{3.10}$$

where Δ V_{DETECT} is the change in V_{DETECT} across the whole tuning range.

The long-term performance is also measured with the BSF, a measure that is essential for using the filter reliably in the field. The filter is connected to a network analyzer, and the notch frequency is recorded over time. The filter is first tested under open loop condition using a constant V_{BIAS} for each of the two resonators. As shown in Fig. 3.15(a), the open loop measurements can sustain the 20 dB rejection for less than 10 minutes before the two resonators are split in frequency. The measured S-parameters of the filter at this point show that the two resonators are significantly separated in frequency.

The closed loop long-term performance of the filter, using the inductive sensing control loop, is also measured. As shown in Fig. 3.15(b) and (c), the two resonators

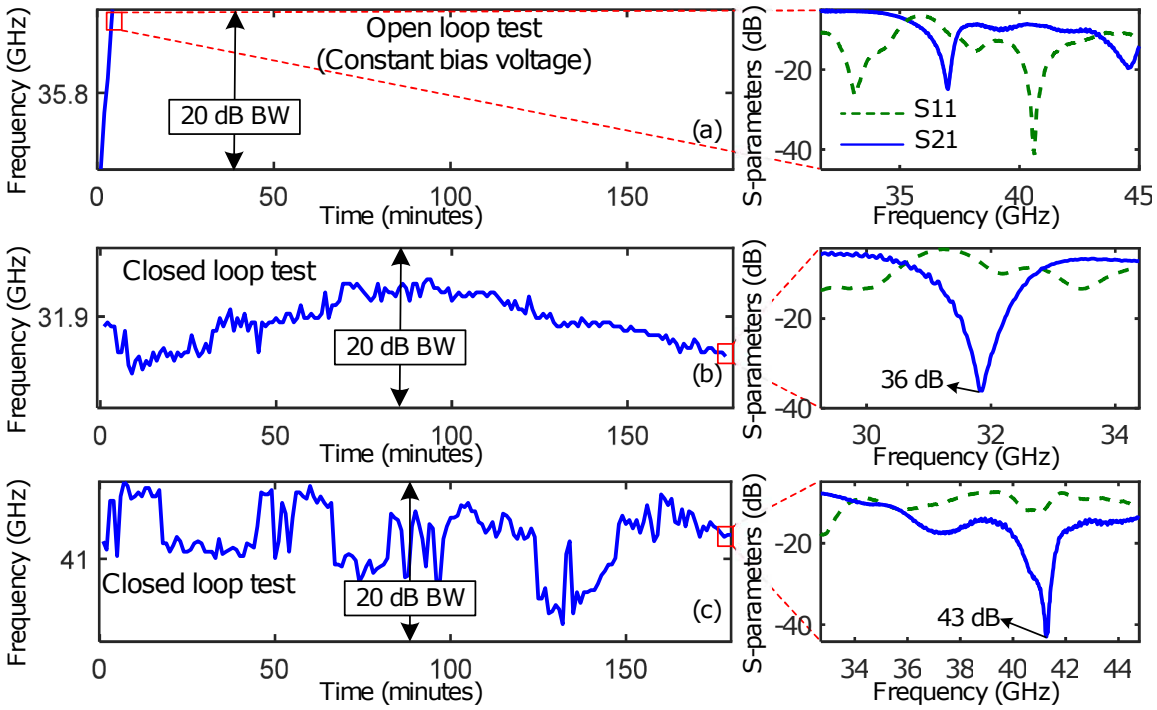

Fig. 3.15.: Measured notch frequency versus time (left) and the filter response at the end of the measurement (right) for (a) open loop (constant V_{BIAS}) where the filter tuning is not sustainable, (b) at 32 GHz and (c) at 41 GHz, where the filter maintains the resonators tuning and the rejection center frequency for the 3-hour test period.

remain properly tuned in frequency, and the 20 dB rejection of the filter response is sustained over the 180-minute test period. The 20 dB bandwidths of the filter are 1% and 1.6% at 32 GHz and 41 GHz, respectively. The filter response at the end of the test period is also shown in Fig. 3.15, where the resonators are still properly tuned. The long-term resolution results are within reasonable agreement with the resolution values calculated from (3.10).

3.6 Conclusion

A monitoring and control method for silicon-based MEMS tunable filters is presented in this chapter. The inductive proximity sensing method, used as feedback in the closed loop control, is capable of accurately sensing the deflection of a 1 μm thick membrane. The control loop is implemented and applied to a tunable evanescent-mode BSF in the 30–42 GHz range. The measured results show that the control loop successfully tunes the filter based on an input from the user, with good repeatability and long-term performance. The presented work facilitates taking advantage of high-performance mm-Wave evanescent-mode cavity filters in real-life applications.

4. HIGH-Q TUNABLE EVANESCENT-MODE CAVITY SIW RESONATORS AND FILTERS WITH CONTACTLESS TUNERS

4.1 Introduction

The recent development of tunable microwave filters has shown their great potential for being an integral component in future microwave and millimeter-wave wireless systems across a wide range of applications. In the last decade, filters based on tunable evanescent-mode (EVA) cavity resonators have demonstrated high performance with high quality factor (Q), wide tuning range, high power handling and a small form factor. Several research efforts have demonstrated the flexibility of cavity-based resonators to realize various filter and diplexer functions with a large degree of reconfigurability. In addition, various technologies have been utilized to implement EVA-cavity filters such as CNC machining, substrate-integrated-waveguide (SIW) and silicon micro-machining [3–10].

In all of these implementations, the main concept of the resonator is to have a conductive flexible membrane creating the ceiling of a post-loaded cavity as shown in Fig. 4.1 (a). The resonant frequency of the cavity can be tuned by actuating the membrane vertically to change the air gap between the post patch and the ceiling. This tuning mechanism was realized using various technologies, the most popular are piezoelectric actuators on top of a conductive ceiling and electro-statically actuated MEMS diaphragms.

These different tuning mechanisms present many challenges to the advancement of EVA-mode cavity based filters to the mass production phase and reliable system integration. First, the achievable displacement by these methods is generally about (15 – 50) μm. Achieving wide tuning range with this range of displacement requires

the design to have initially small gaps usually less than 5 μm. This requirement increases the sensitivity and complexity of the filter assembly and manufacturing. A more practical challenge to this scheme is the mechanical reliability of the tuner. Since the tuner has a fixed anchor point, the repeated bending of the tuner results in mechanical creep and fatigue which changes the performance of the membrane over time. In addition, the actuation does not have a constant mode of bending. Other uncontrollable and undesired bending modes can occur during tuning.

One approach to overcome the mechanical reliability drawbacks of the tuner is to develop a closed-loop monitoring and control system to control each individual cavity. Since the cavity is completely closed, it was proposed to monitor the tuner displacement externally. This has been accomplished using capacitive monitoring [27,36] and resonant monitoring [29,30]. However, these implementations still require small gap values due to the limited available deflection of the membrane. This significantly limits the tuning range where the monitoring and control resolution is acceptable. In addition, these approaches require sensitive assemblies between the filter, the tuning membrane and the monitoring device which increases the overall complexity of the manufacturing process. Also, the external monitoring of the tuner movement will always be limited and does not necessary capture the non-ideal bending effects that occur inside the cavity.

The second approach to avoid both the mechanical issues and the sensitive assembly is to modify the cavity to have ring capacitance around the post patch instead of the vertical gap and tune it electronically using varactors. Based on this approach, a wide range of filter applications have been demonstrated [37–39]. Although using the varactors presents a simple solution to the mentioned challenges, it negatively affects the filter performance by dramatically reducing Q and tuning range. In addition, this approach significantly limits the power handling capability of the resonator due to the non-linearities in the varactors.

To overcome the aforementioned challenges without significantly compromising the performance of EVA-mode cavities, we present a new class of tunable, EVA-mode

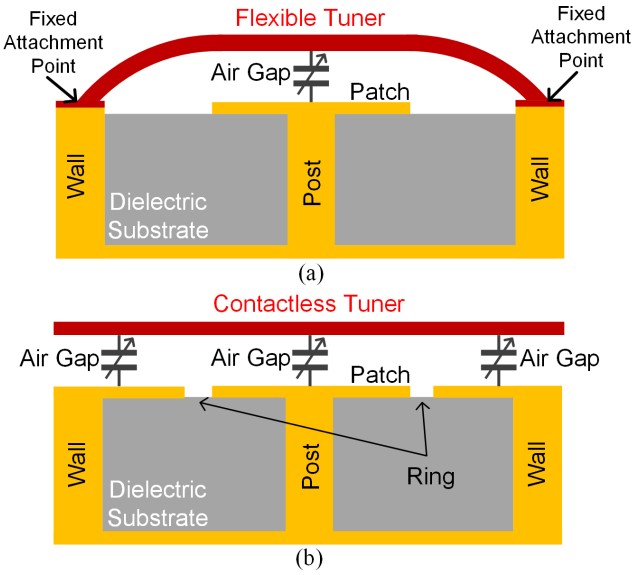

Fig. 4.1.: Tunable EVA-mode cavity resonator tuning concept (a) conventional (b) proposed.

cavity resonators with contactless tuners. The concept of the proposed resonator is shown in Fig.4.1 (b). In this approach, the ring loaded SIW cavity is tuned using a floating tuner which creates a capacitance to both the post patch and the cavity top wall. The resonant frequency of the proposed cavity depends on the equivalent capacitance which can be controlled by the vertical movement of the tuner. By avoiding the attachment of the tuner to the cavity, the assembly process becomes significantly simpler which improves the tuning reliability. The proposed tuning scheme is compatible with any actuator that provides sufficient vertical displacement. Using this approach, we present resonators with a measured unloaded quality factor, Q_u, in the range 200 – 650, for a larger than octave tuning range and an initial gap of 40 – 50 μm.

The text and figures presented in this chapter are based on the following paper: M. Abdelfattah and D. Peroulis, "High-Q Tunable Evanescent-Mode Cavity SIW Resonators and Filters With Contactless Tuners," in *IEEE Transactions on Microwave Theory and Techniques*.

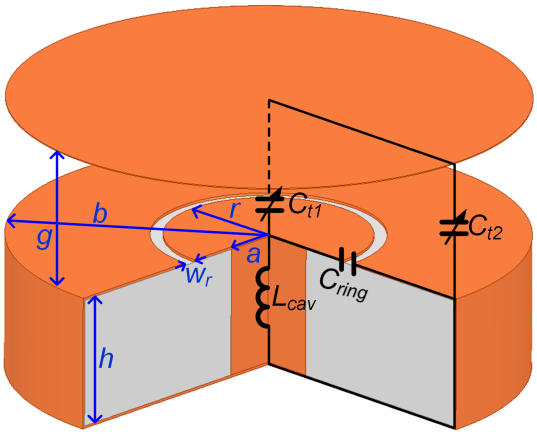

Fig. 4.2.: Proposed contactless tuner resonator 3D view with main physical dimensions and simplified lumped element model.

4.2 Resonator Design

A 3-D view of the proposed tunable cavity resonator structure with a contactless tuner is shown in Fig. 4.2 highlighting the main physical dimensions and basic lumped element model. Without the tuner, the resonator is a ring-gap loaded cavity resonator such as the presented in [40]. It is realized by isolating a central circular patch on the top wall and shorting it to the bottom wall of the cavity through the central post. The resultant cavity has a fundamental TEM resonant mode which results from the inductance of the shorted coaxial transmission line (L_{cav}) and the annular gap capacitance (C_{ring}) between the patch and the top wall of the cavity. The inductance (L_{cav}), of the TEM mode, can be approximated as

$$L_{cav} = \frac{60}{\omega\sqrt{\epsilon_r}} \tan\left(\frac{\omega h\sqrt{\epsilon_r}}{c}\right) \ln(b/a) \tag{4.1}$$

where h is the cavity height, b is the cavity radius, a is the post radius, ϵ_r the dielectric constant of the substrate, and c is the speed of light [8, 37].

In addition, the annular capacitance C_{ring}, when neglecting the copper thickness, is given by

$$C_{ring} = \frac{2\pi r\epsilon_0(1+\epsilon_r)}{\ln(1+\frac{w_r}{r})}\int_0^\infty [J_0(\zeta r) - J_0(\zeta(r+w_r))]\frac{J_1(\zeta r)}{\zeta}d\zeta \tag{4.2}$$

where r is the patch radius, w_r is ring width and J_n is the nth-order Bessel function of the first kind [41, 42].

Thus, the static resonant frequency of the resonator without the tuner is given by

$$\omega_0 = \frac{1}{\sqrt{C_{ring}L_{cav}}}. \tag{4.3}$$

Introducing the contactless tuner on top of the cavity modifies the total capacitance between the center patch and the top wall. Since the tuner is floating, it creates a parallel plate capacitance with both the center patch, (C_{t1}), and the top wall, (C_{t2}), as shown in Fig. 4.2. These capacitances create a parallel path for the signal. Using this simplified lumped element model, the equivalent capacitance between the patch and the top wall can be expressed as

$$C_{eq}(g) = C_{ring} + C_{t12}(g) \tag{4.4}$$

where C_{t12} is the series equivalence of C_{t1} and C_{t2}. When only considering the parallel plate capacitance and assuming a gap (g) between the tuner and cavity, C_{t12} can be found as

$$C_{t12} = \frac{C_{t1}C_{t2}}{C_{t1}+C_{t2}} = \frac{\epsilon_0\pi r^2}{gb^2}(b^2 - (r+w_r)^2) \tag{4.5}$$

The resonant frequency of the resonator, in the presence of the tuner, becomes dependent on the total capacitance C_{eq} as shown in

$$\omega_0(g) = \frac{1}{\sqrt{C_{eq}(g)L_{cav}}} \tag{4.6}$$

Since C_{eq} and ω_0 are dependent on the gap (g), the tuning of the resonator can be enabled by varying g through the vertical displacement of the tuner.

4.2.1 Frequency Tuning Range

After establishing the tuning concept, this section will discuss how the cavity parameters affect the frequency tuning range (TR). As shown in (4.4), C_{eq} has a fixed part C_{ring} and a tunable part C_{t12}. Both of these capacitances strongly depend on r as shown in (4.2) and (4.5). The variation of C_{eq} with tuner displacement depends on the ratio C_{t12}/C_{ring}. For a constant w_r, this ratio is dominated by the value of r/b. Based on the previous analysis, the capacitance ratio is expected to have an optimum value with respect to the value of r/b. The optimum value can be found by solving the formula

$$\frac{\partial}{\partial r}\Big(\frac{C_{t12}}{C_{ring}}\Big) = 0 \tag{4.7}$$

To simplify the analysis, it is assumed that ($w_r << r$) and the expression in (4.2) is simplified to ($C_{ring} = 2\pi r\epsilon_0(1+\epsilon_r)$). Solving (4.7), under these assumptions, results in a maximum when $r = b/\sqrt{3} \approx 0.57b$.

To verify the expected relations, we used the quasi-static solver ANSYS Q3D [43] to simulate the structure compromised of the center patch, the cavity top wall and the tuner to extract C_{eq} versus g for different values of r while $b = 10$ mm. The dielectric substrate is Rogers TMM3 ($\epsilon_r = 3.27$, $\tan(\delta) = 0.002$). The simulation along with the theoretical model results are shown in Fig. 4.3 (a) where r is between 1 mm and 7 mm, and g is swept from 10 μm to 3 mm. C_{eq} is defined as the total capacitance between the signal net (center patch) and the ground net (cavity top wall) while the tuner is assigned as a floating net.

The difference between the simulated and the theoretical capacitance values is less than 10% for the cases with ($r = 2 - 7$) mm with smaller error for small gap values. For the case $r = 1$ mm, the error reaches 18%, when g is maximum, due to the contribution of the copper thickness which is not considered in the theoretical model. A more accurate analytical description of this capacitance can be found in [41].

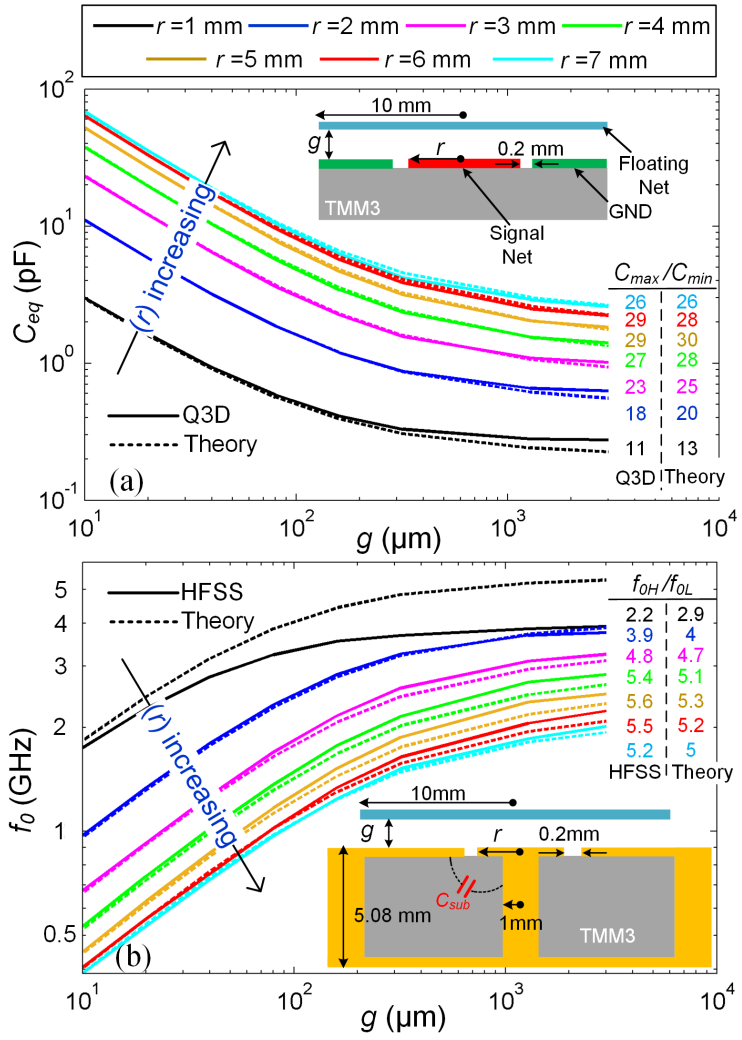

Fig. 4.3.: (a) Equivalent capacitance and (b) Resonant frequency versus g for different r with $b = 10$ mm, $h = 5.08$ mm, $w_r = 0.2$ mm, $a = 1$ mm.

Furthermore, it can be observed that the capacitance tuning increases with r/b and reaches a maximum around $r = 5 \sim 6$ mm as expected from analytical derivation.

To demonstrate the frequency tuning of the cavity using this capacitance tuning structure. A full cavity is designed and simulated using ANSYS High Frequency Structure Simulator (HFSS) [44]. The value of a is fixed at 1 mm to only observe how the capacitance tuning affects the frequency tuning range. The simulated as well as the calculated frequency tuning curves are shown Fig. 4.3 (b). The difference error

Table 4.1.: Required displacement (Δg) in μm to achieve given TR.

TR $\frac{f_{0H}}{f_{0L}}$	$g_0 = 20$ μm			$g_0 = 40$ μm			$g_0 = 60$ μm		
	r (mm)			r (mm)			r (mm)		
	2	3	6	2	3	6	2	3	6
1.5	36	33	33	99	76	66	196	123	103
2	116	88	86	1060	260	208	-	950	592
2.5	518	260	213	-	2070	847	-	-	2950
3	-	657	397	-	-	-	-	-	-
3.5	-	2880	1055	-	-	-	-	-	-

(-) indicates that TR is unachievable with the corresponding r, g_0 values.

in frequency is less than 8% for the cases $r = 2 - 7$ mm. However, it reaches 35% for $r = 1$ mm due to two reasons; the copper thickness effect mentioned previously and the capacitance between the top wall and the post through the substrate shown as C_{sub} in Fig. 4.3 (b). This capacitance is only significant when the patch's size is the same as the post's size ($r = a$) and has negligible effects when the patch becomes larger than the post. Moreover, the maximum frequency TR is achieved at $r = 5 \sim 6$ mm as previously predicted.

Another critical parameter that has a great effect on the tuning range is the initial gap value, g_0. It can be seen in Fig. 4.3 (b) that the curve slope is much larger for smaller gaps as expected by the parallel plate capacitance dependence. Therefore, with larger g_0, the tuning range will be reduced. This is illustrated in Table 4.1 where it shows the required tuner displacement, Δg, to achieve different values of TR. It is noted that in order to achieve a larger tuning range with smaller displacement, a smaller g_0 and/or a larger r/b have to be used.

In this section, we have demonstrated the significant impact of the ratio r/b on the frequency TR. In fact, it will be later shown that this ratio has a large impact on the cavity performance in all aspects. In many cases, for the resonator to meet

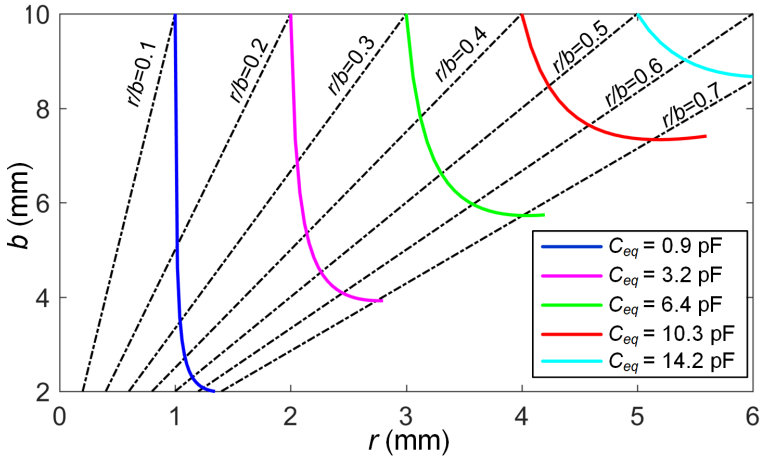

Fig. 4.4.: Constant C_{eq} contours covering different values for the ratio r/b with a fixed gap $g = 40$ μm.

certain specifications, the ratio r/b needs to be modified while maintaining constant f_0 or constant C_{eq} for the same air gap. Fortunately, this can be achieved since C_{eq} is dominantly the result of the series connection of two capacitances as shown in (4.4) (4.5). This gives us the opportunity to change the values of both C_{t1} and C_{t2} while keeping the equivalent value C_{t12} constant. This additional degree-of-freedom is demonstrated in Fig. 4.4 where constant C_{eq} contours are plotted spanning a wide range of r/b values with a constant gap of 40 μm. Moreover, these contours also represent constant f_0 curves given that L_{cav} is kept constant by keeping fixed values for h and b/a. This technique will prove useful in the resonator design and optimization as shown in Section 4.3.

4.2.2 Quality Factor

Compared to traditional EVA-mode cavity resonator, the contactless resonator has more loss mechanisms that need to be analyzed individually in order to successfully optimize the resonator quality factor, Q. Fig. 4.5 shows a modified lumped element model that includes the main losses in the resonator. The added lossy elements are G_{rad}, G_{die} and R_{cav} which represent the radiation losses, the dielectric losses and the

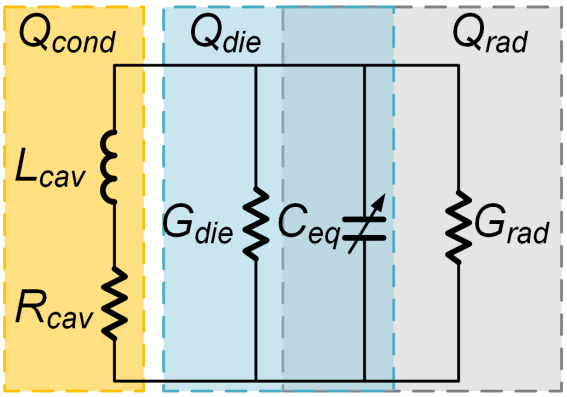

Fig. 4.5.: Lossy lumped element model for the proposed resonator showing Q breakdown.

conductive losses, respectively. All of these elements are dependent on the resonator physical dimensions and the resonant frequency. In order to study these losses, we define individual Q values, each represents one type of losses. These are Q_{rad}, Q_{die} and Q_{cond} defined as

$$Q_{rad} = \frac{\omega C_{eq}}{G_{rad}}, Q_{die} = \frac{\omega C_{eq}}{G_{die}}, Q_{cond} = \frac{\omega L_{cav}}{R_{cav}}. \tag{4.8}$$

Using these definitions, the total Q factor of the resonator, Q_{tot}, is given by

$$Q_{tot} = \left(\frac{1}{Q_{rad}} + \frac{1}{Q_{die}} + \frac{1}{Q_{cond}}\right)^{-1}. \tag{4.9}$$

Similar to the tuning range, the main dimensions for Q optimization are r and g. Therefore, the following discussion presents the effect of these parameters on each type of loss, while the other dimensions are fixed ($b = 10$ mm, $a = 1$ mm, $h = 5.08$ mm, $w_r = 0.2$ mm).

Radiation Loss

The proposed design suffers from radiation losses due to the open ring around the patch. The radiated power from the slot mainly depends on the slot dimensions

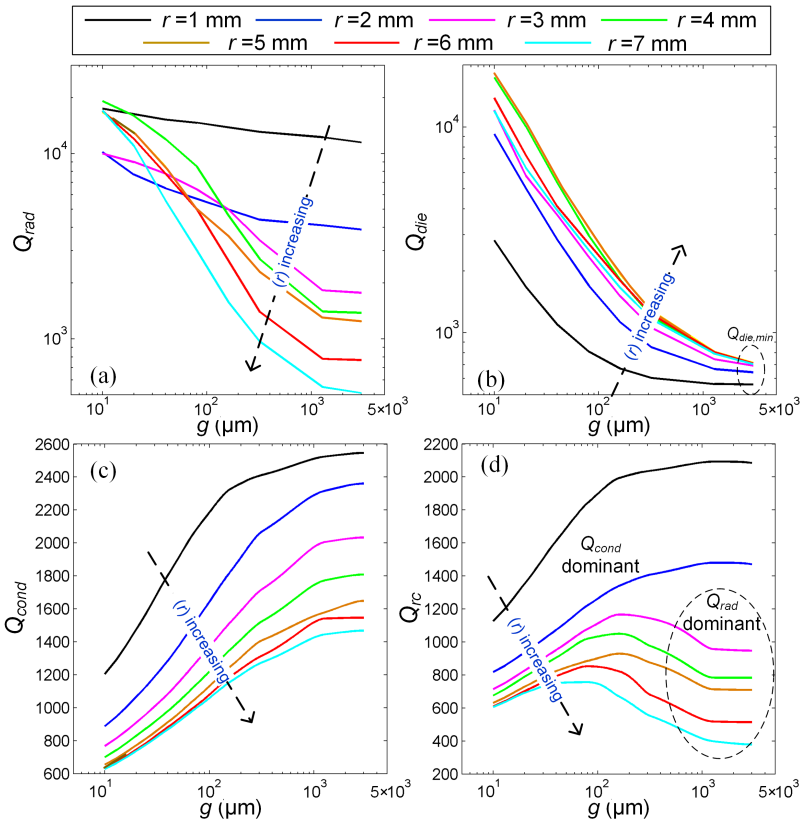

Fig. 4.6.: Different Q values versus g (a) Q_{rad} (b) Q_{die} (c) Q_{cond} (d) Q_{rc}, note that f_0 is not maintained constant.

and the resonant frequency. Q_{rad} is extracted from HFSS simulations at different r and g values as shown in Fig. 4.6 (a). To remove the other losses, the cavity is simulated with perfect conductor walls and a lossless dielectric substrate. By studying the curves individually, it is observed that as g is increased, Q_{rad} is reduced. This is due to two factors; the reduction of C_{eq} in addition to the increase of G_{rad} with higher frequency. Also, increasing r significantly reduces Q_{rad}. This is explained by the increase of the ring length ($2\pi r$). However, the Q reduction is less severe when g is smaller because of the increase of C_{eq} due to the larger patch area which has an opposite effect.

Dielectric Loss

Dielectric losses are the result from the non-zero loss tangent, $\tan(\delta)$, of the cavity substrate. These losses, represented by G_{die}, emerge due the fringing electric field, associated with C_{ring}, passing through the dielectric substrate. The minimum value for Q_{die}, occurs when $C_{eq} = C_{ring}$ and it depends on ϵ_r and $\tan(\delta)$. When neglecting the copper thickness, and assuming $r > a$ this value can be approximated as

$$Q_{die,min} \approx \frac{1 + 1/\epsilon_r}{\tan(\delta)}. \tag{4.10}$$

A larger copper thickness improves this value, because a larger fraction of the fields will pass through air rather than the substrate. As g is reduced, C_{eq} is increased, with negligible effect on G_{die}, which results in increasing Q_{die}. To illustrate these relations, the resonator is simulated with ideal conductors and no radiation losses. The resulting Q_{die} curves are shown in Fig. 4.6 (b). For the case ($r = a = 1$ mm), Q_{die} is smaller than the other cases. This is because of the larger C_{sub} capacitance mentioned previously. Nonetheless, this capacitance and the losses it adds can be reduced if the center post is formed using multiple smaller vias as in the SIW implementation discussed later.

Conductive Loss

The conductive losses are due to the finite conductivity of the cavity walls and are represented using R_{cav} which is in series with the cavity inductance. As shown in (4.8), Q_{cond} is proportional to ωL_{cav}, which by looking at (4.1) is proportional to frequency. Therefore, unlike the previous Q values, Q_{cond} increases proportionally as the gap increases, as shown in Fig. 4.6(c). It is also shown that increasing r shifts Q_{cond} down due to the larger loading of the cavity. Based on reported studies of the conductive losses, Q_{cond} can be analytically expressed as

$$Q_{cond} = \frac{377 \tan\left(\frac{\omega h\sqrt{\epsilon_r}}{c}\right) \ln(b/a)}{R_s\sqrt{\epsilon_r}(h/a + h/b + 2\ln(b/a))} \tag{4.11}$$

where R_s is the surface resistance [7, 8, 37]. It was also shown that Q_{cond} is optimum when $a = a_{opt} = b/3.6$. In addition, increasing the cavity size by increasing b and h will improve Q_{cond} as L_{cav} is increased and more energy will be stored in the cavity. An illustration of the effects of h will be presented later in Table 4.3.

Combined Loss

Since the proposed concept can be implemented using different dielectric substrates which vary in their loss tangent, It is beneficial to study the combined effect of the conductive and radiation losses first. To capture these losses, we define a new quality factor, Q_{rc}, as

$$Q_{rc} = \left(\frac{1}{Q_{rad}} + \frac{1}{Q_{cond}}\right)^{-1}. \tag{4.12}$$

The simulation results for Q_{rc} are shown in Fig. 4.6(d). It is shown that Q_{rc} is inversely proportional to r. Also, it is shown that Q_{rc} has regions that are proportional to g when Q_{cond} is dominant, and other regions with the opposite dependence when Q_{rad} is dominant.

Finally, by simulating the resonator with all the losses included, the total quality factor, Q_{tot} given by (4.9) is extracted. The results of the simulations are shown in Fig. 4.7 (a-b). It is observed that for small g values, Q_{tot} is increasing with frequency as Q_{cond} is dominant. It reaches a maximum value when g is between 80 μm and 160 μm, then starts declining due to the negative slope of Q_{die} and Q_{rad}. As for large g, smaller r results in better Q_{tot} because Q_{die} is similar for most r values but Q_{rc} is inversely dependent on r. This is not observed for $r = 1$ mm because of the worse Q_{die} as mentioned previously, therefore it is recommended to always choose $r > a$.

Finally, the effects of a and w_r on Q_{tot} are shown in Fig. 4.8. As discussed previously, Q_{cond} is optimum with $a = b/3.6$ which improves Q_{tot}, specifically when

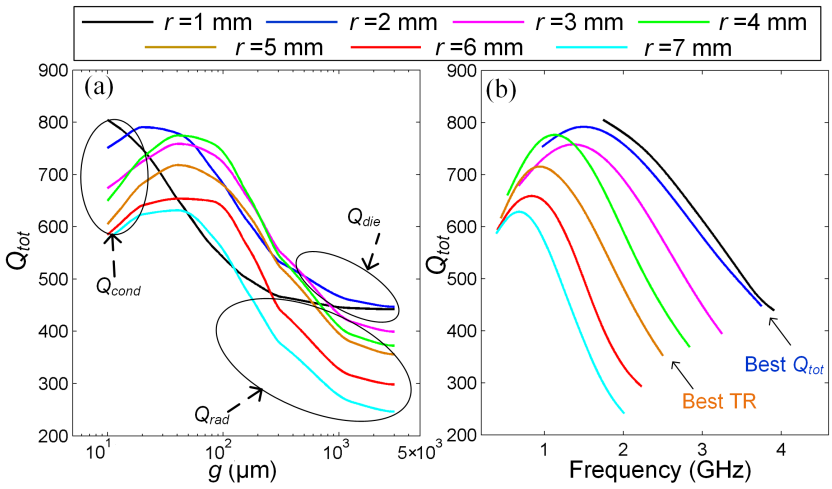

Fig. 4.7.: (a) Q_{tot} vs. g (b) Q_{tot} vs. f for different r values.

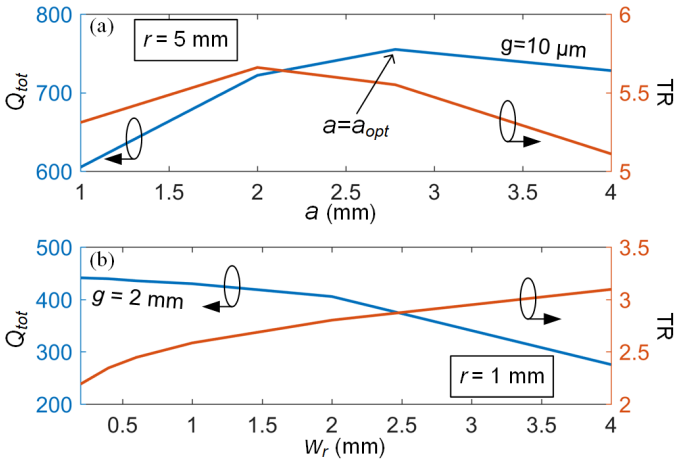

Fig. 4.8.: Q_{tot} and TR dependence on (a) post radius, a and (b) ring width, w_r.

Q_{cond} is dominant (small gap), with a very small compromise in the tuning range. Moreover, increasing w_r increases the tuning range as C_{ring} is reduced, however, this compromises Q_{tot} as more power is radiated. Therefore, a smaller w_r is recommended, and the tuning range should be increased only using r.

4.2.3 SIW Implementation

The previous discussion of the resonator design and optimization was based on the model shown in Fig. 4.2. However, when implementing this resonator using SIW technology, the cavity walls and the post have to be realized through plated vias as shown in Fig. 4.9 (a-b). Replacing the side walls with vias has a small effect on the resonator performance. On the other hand, the post vias are expected to reduce Q_{tot} specifically for small g values and small r values. This is due to the reduction of the patch area which effectively reduces C_{t1}. This was shown to reduce both Q_{die} and Q_{rad}.

Fig. 4.9 also shows the external coupling structure to be used with the SIW resonator. External coupling is realized through grounded coplanar waveguide (GCPW) feed, at the bottom of the cavity, with signal line width (w_{cpw}) and gap (g_{cpw}). For the case of weak external coupling, which is used to extract the unloaded quality factor, Q_u, from S_{21} measurements, the signal line is shorted with the bottom wall of the cavity as shown in Fig. 4.9 (a). For larger values of external coupling, which are required for practical filter design, the signal line is shorted with the top wall using a coupling via. The strength of the coupling is controlled by the distance of the coupling via to the cavity center, (df).

After demonstrating the design trade offs in the previous sections, we designed two cavities with different dimensions as shown in Fig. 4.9 which are Resonators A and B. The dimensions of these resonators are shown in Table 4.2. Resonator A is designed to have higher Q, specifically for g more than 200 μm, compromising tuning range as result. On the other hand, resonator B is designed to have an octave tuning range with $Q > 270$ given that $g_0 = 50$ μm .

4.2.4 Power Handling

There are three main limitations that affect the power handling capability (PHC) of tunable EVA-mode cavities; tuning non-linearities, self-heating and gas breakdown

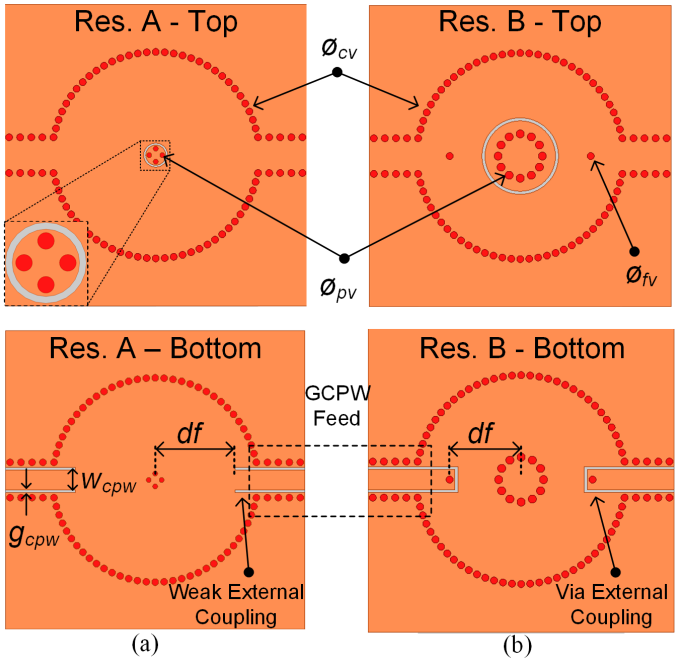

Fig. 4.9.: SIW implementation of the proposed cavity resonator (a) Resonator A with weak external coupling (b) Resonator B with via external coupling. df is the spacing between the cavity center and the end of the GCPW feed. w_{cpw}, g_{cpw} are the GCPW dimensions. $\varnothing_{cv}, \varnothing_{pv}, \varnothing_{fv}$ indicate the diameter of the cavity side wall vias, the post vias and the feeding vias, respectively.

Table 4.2.: Designed resonators dimensions.

Dimension	Res. A	Res. B	Dimension	Res. A&B
a	0.9	2.7	b	10
r	1	3.5	h	5.08
w_r	0.2	0.25	$\varnothing_{cv}$	0.7
df (weak)	8	8	w_{cpw}	1.94
df (via)	6.5	7	g_{cpw}	0.2
$\varnothing_{pv}$	0.5	0.8	$\varnothing_{fv}$	0.7

*All dimensions are in (mm).

[45, 46]. The non-linear behavior results from the tuner's self-actuation due to the induced RF force between the tuner and the post patch. This results in distorting the filter response with increasing input power [45]. This type of PHC limitation is strongly dependent on the actuator type and the gap between the post and the tuner. In [47], EVA-mode cavities, actuated using piezoelectric actuator with tuning gap smaller than 20 μm, have demonstrated very small distortion for input power up to 10 W. As the proposed contactless resonator enables larger gap values, it is expected that it will improve this type of limitation on the PHC.

Applying continuous-wave (CW) high input power to SIW filters results in heating the substrate due to both conductive and dielectric losses. The self-heating mechanism is studied and analyzed in [46] on static SIW resonators. Since, this mechanism is independent of the tuning scheme, the same analysis can be directly applicable to the proposed resonator with the contactless tuner.

EVA-mode resonators produce the majority of the electric field density in the air gap between the post patch and the tuner. With larger input power, the electric field density increases, and, at a certain power level, it results in gas breakdown in the air gap. When the breakdown occurs, the resonator is shorted. This defines the peak PHC of the resonator, P_{max}. The authors in [48] presented the following formula to predict P_{max} of EVA-mode cavity resonators based on EM and circuit simulations,

$$P_{max} = \left(\frac{E_{breakdown}}{E_{max-norm}}\right)^2 \times \frac{1}{W_{stored-max}} \tag{4.13}$$

where $E_{breakdown}$ is the air breakdown electric field 7.9 V/μm, $E_{max-norm}$ is the normalized maximum electric field on top of the post found using HFSS eigen-mode simulations with the stored energy in the resonator normalized to 1 nJ and $W_{stored-max}$ is the maximum stored energy in the resonator in (nJ) which depends on the filter group delay and losses [48, 49].

When considering a single resonator with a fixed external quality factor (Q_e) and fixed resonant frequency (f_0), the stored energy $W_{stored-max}$ at resonance is expressed as,

$$W_{stored-max} = \frac{1}{2} C_{eq} V^2 \tag{4.14}$$

where V is the nodal voltage across C_{eq}. Since, C_{eq} is mainly compromised of the series connected C_{t1} and C_{t2}, voltage across C_{t1} is usually larger because it has smaller capacitance. Therefore, air breakdown occurs when this voltage induces electric field close to $E_{breakdown}$ inside C_{t1}. For a fixed L_{cav} and C_{eq}, there are two approaches to reduce $E_{max-norm}$ and improve P_{max}. The first is having a larger value for g_0, which results in smaller induced electric field for the same voltage value. This is shown in Fig. 4.10, where the prediction method is used to evaluate P_{max} at different g_0 values. To maintain the frequency f_0, C_{eq} is kept the same by increasing the value of r. It is observed that P_{max} improves dramatically when a larger g_0 is used.

The other approach to improve P_{max}, if g_0 is fixed, is by modifying the ratio r/b to result in a larger value for C_{t1}. This reduces the voltage across C_{t1} and $E_{max-norm}$ as a result. This is demonstrated in Fig. 4.10, where g_0 is fixed at 60 μm and the dimensions r, a, b are modified to maintain fixed C_{eq} and L_{cav}. It is shown that P_{max} has a linear increase as r/b is increased. Finally, the effect of the dimensions a, b, h on the power handling can be intuitively predicted by observing their effect on L_{cav}. Any modifications of these dimensions that increases L_{cav}, at a certain f_0, will result in a smaller value for C_{eq} and larger value for V which reduces P_{max}. The effect of h on the cavity performance is illustrated in Table 4.3. It is shown that P_{max} is reduced with larger h.

Table 4.3.: Illustration of the effect of h on cavity performance.

$f_{0L} = 1.65$ GHz	h (mm)	r/b	TR	P_{max} (W)	Q_{min}
$g_0 = 50$ μm	2.504	0.56	2.6	396	209
$b = 10$ mm	5.08	0.35	2.22	111	408
$a = 2.7$ mm	6.1	0.31	2.02	85	445

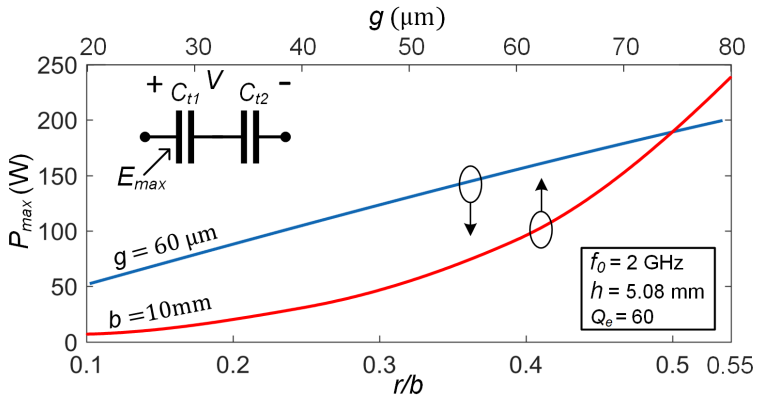

Fig. 4.10.: Power handling versus g and r/b for fixed frequency $f_0 = 2$ GHz and $h = 5.08$ mm.

The prediction method was utilized to predict the power handling for the designs of Resonator A and Resonator B when excited using the via coupling with dimensions shown in Table 4.2. The results of the normalized electric field using HFSS simulations are shown in Fig. 4.11 with corresponding power handling calculations for each case. Resonator A is studied for the case $g = 70$ μm ($f_0 = 3.25$ GHz), while Resonator B is simulated with $g = 49$ μm ($f_0 = 1.75$ GHz). The expected power handling is found to be about 30 W for Resonator A and 149 W for Resonator B. These predictions will be compared to measurements in section 4.5.2. It should be noted that $W_{stored-max}$ is proportional to C_{eq}. Also, $E_{max-norm}$ is reduced with a larger gap. These two factors ensure that P_{max} increases when we tune the resonator to higher frequencies.

4.2.5 Stability and Repeatability

The proposed tuning scheme is compatible with any actuator that could create sufficient vertical displacement. The reliability of the tuning will depend on the ability of the actuator to maintain, or travel to, a certain position with minimal error. The displacement uncertainty, g_{err}, results in a frequency error defined as

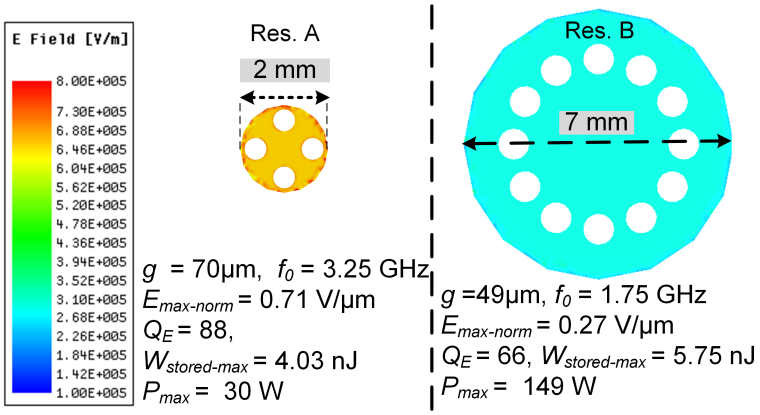

Fig. 4.11.: Electric field distribution on the post patch along with P_{max} calculations for both resonator designs A and B.

$$f_{err} = \frac{f_{max} - f_{min}}{f_{avg}} \times 100\% \tag{4.15}$$

f_{err} is maximum at the lowest frequency (f_{0L}) of the tuning range when $g = g_0$. Therefore, for the expected g_{err} of a certain actuator, a larger value for g_0 is required to reduce f_{err}. However, it was shown that, for fixed cavity dimensions, larger g_0 will result in a smaller TR. Hence, the cavity design needs to be modified to satisfy TR when starting with a specific g_0. This is illustrated in Fig. 4.12. In this example, the required frequency range is 2 – 4 GHz with available displacement $\Delta g = 2$ mm. The frequency error is calculated at different g_0 values given that $g_{err} = 1$ μm. For each g_0, the ratio r/b is varied in order to maintain the required frequency range. As expected from Section 4.2.1 larger r/b is required to satisfy the TR when starting with a larger g_0.

In this paper, we have chosen two main metrics to evaluate the tuning reliability, long term stability and repeatability. Stability is defined as the frequency error over time with the resonator fixed at the lowest (most sensitive) frequency in the tuning range. Repeatability is defined as the worst case frequency error for a certain tuning state as the resonator is tuned to cycle different states across the tuning range.

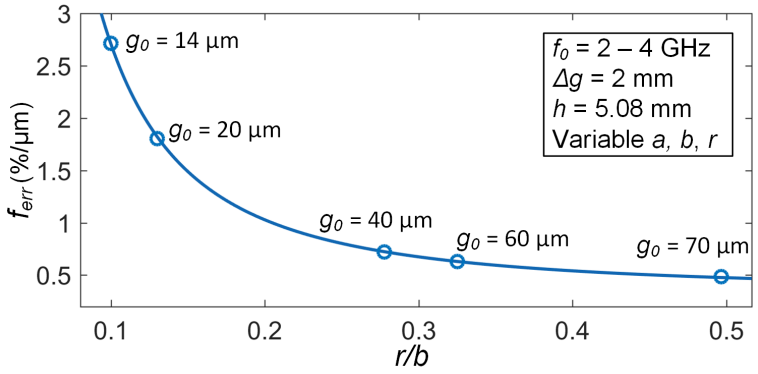

Fig. 4.12.: Frequency error caused by 1 μm at different g_0 values for a specific frequency range and actuator displacement.

4.3 Resonator Design Procedure

In this section, we propose an iterative design procedure to optimize the cavity based on certain specifications. The procedure assumes required values for tuning range, power handling and frequency error based on given size and maximum actuator displacement. The following procedure will guide the designer through the right sequence of decisions to get the optimal cavity dimensions that achieve the best Q given the required specifications.

1. Start with largest b and h based on size limitations. For a fixed value of f_{0L}, larger values of h will improve Q but will reduce both TR and P_{max} as illustrated in Table 4.3.

2. Choose the smallest practical values for r and w_r that are achievable by the manufacturing method. Keep a smaller than r.

3. Start with the smallest practical g_0. This is based on the accuracy of the assembly and the actuator resolution.

4. Check TR given the available Δg. If not satisfied, increase r and modify a to make it closer to optimum value a_{opt}. Repeat this step until TR is achieved.

5. Use power handling prediction method (Section 4.2.4), and the frequency error simulation (Section 4.2.5) to predict P_{max} and f_{err} at g_0 given the expected actuator displacement error. If higher P_{max} or lower error are needed, increase g_0 and redo step 4.

6. At this point, the frequency range could be different from the desired range. To shift the frequency range while satisfying the other specifications, all the cavity dimensions should be scaled with the same ratio. In many cases, h is limited to the available PCB substrates thicknesses. Thus, it is more practical to only scale a, b, r to shift f_{0L} to desired frequency.

7. Check if TR, P_{max} and f_{err} are still satisfied after scaling. If not, increase r/b, while maintaining constant f_{0L} as previously illustrated in Fig. 4.4. Stop when specifications are met.

8. Find the minimum Q which occurs at the maximum frequency f_{0H}. If Q needs improvement, relax P_{max} and/or f_{err} specifications and restart from step 4, or relax size limits (b, h) and restart from step 1.

To illustrate the proposed design procedure, Table 4.4 shows the process of designing a tunable resonator with the following specifications: $f_0 = 2 - 4$ GHz, $b \leq 10$ mm, $w_r \geq 0.25$ mm, $g_0 \geq 40$ μm, $P_{max} \geq 100$ W, $f_{err} \leq 0.5\%/\mu$m and the chosen substrate is Rogers TMM3 with $h = 5.08$ mm. The first step starts with largest $b = 10$ mm, smallest $w_r = 0.25$ mm, $r = 1$ mm and $a = 0.9$ mm. After completing the procedure, the final design meets all the specifications with Q between 428 - 805.

Table 4.4.: Demonstration of the Contactless Cavity Resonator Iterative Design Procedure

step	b (mm)	a (mm)	r (mm)	g_0 (μm)	f_{0L} (GHz)	f_{0H} (GHz)	TR	f_{err} (%/μm)	P_{max} (W)	Comments
1	10	0.9	1	40	2.91	4.16	1.43	-	-	Fails TR, $r, a \uparrow$
2	10	1.42	2	40	1.95	3.86	1.98	1.09	-	Fails f_{err}, $r, a \uparrow$
3	10	2.7	3	40	1.72	3.73	2.17	0.99	-	Fails f_{err}, $g_0 \uparrow$
4	10	2.7	3	49	1.86	3.73	2	0.88	-	Fails f_{err}, $r \uparrow$, $a = a_{opt}$
5	10	2.7	3.25	60	1.79	3.7	2.06	0.49	155	Shift f_{0L}, scale a, b, r w\same ratio
6	9.2	2.46	2.99	60	2.03	3.9	1.92	0.72	135	Fails f_{err}, $r/b \uparrow$ w\fixed f_{0L}
7	7.82	2.08	3.08	60	2.04	4.12	2.02	0.54	144	Final design, $428 < Q < 805$

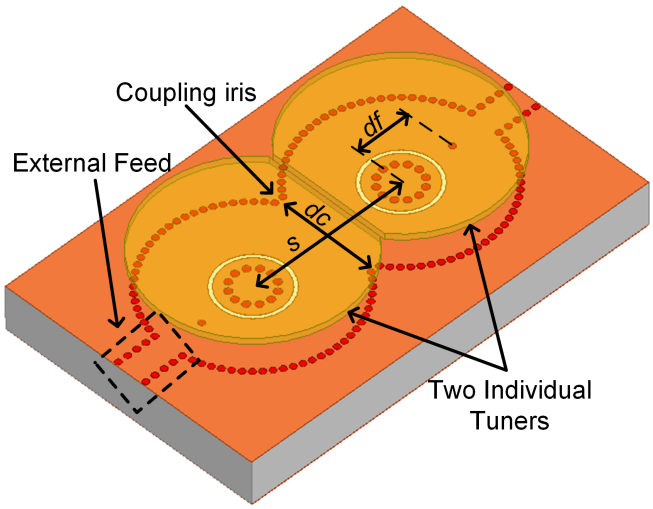

Fig. 4.13.: 3-D view of a second order BPF based on Resonator B design.

4.4 Filter Design

The literature is rich in filter designs employing tunable EVA-mode cavities, most of these designs will be compatible with the proposed contactless resonator. Therefore, we will briefly discuss the filter design concepts in this section. In general, to obtain a filter response using the proposed resonator, external coupling and inter-resonator coupling between the cavity resonators need to be realized. The response type and the fractional bandwidth (FBW) depend on the strength of these coupling values [50]. A 3D view of a second order filter based on Resonator B design is shown in Fig. 4.13. External coupling to the GCPW feed is realized using the coupling via that shorts the signal line in the bottom with the top wall of the cavity. The strength of the external coupling is dependent on df. Furthermore, inter-resonator coupling is realized through the coupling iris between the two cavities. The strength of the inter-resonator coupling is increased by reducing the spacing between the cavity posts, s, and/or increasing the iris opening, dc. Further details about the modeling and optimization of external and inter-resonators coupling can be found in [8]. In addition, two separate tuners, with two individual actuators, are used to independently tune each resonator.

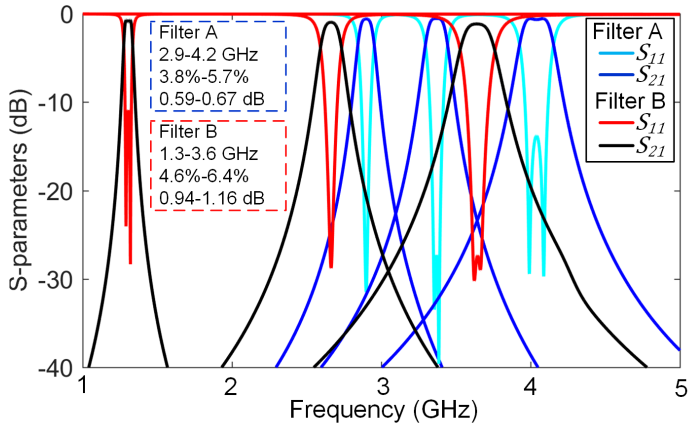

Fig. 4.14.: HFSS simulation results for Filters A and B highlighting frequency tuning, FBW and IL.

To demonstrate filter performance, based on the proposed concept, we designed two second-order filters. Filter A is based on Resonator A to maintain high-Q at large gaps and Filter B is based on Resonator B to offer wider tuning range. For both filters, s is 17.8 mm and dc is 11.05 mm, while df is 6 mm and 6.1 mm for filters A and B, respectively. HFSS simulation results for both filters with expected FBW and insertion loss (IL) are shown in Fig. 4.14. Filter A covers the range 2.9 GHz – 4.2 GHz with FBW (3.8% – 5.7%) and a starting g_0 of 40 μm while Filter B covers the range 1.3 GHz – 3.6 GHz, with FBW (4.6% – 6.4%) and g_0 of 35 μm.

4.5 Experimental Validation

To demonstrate the proposed resonator performance and trade-offs, multiple resonators and filters were manufactured and measured. The devices were manufactured using conventional 2D printed circuit board (PCB) machining in Birck Nanotechnology Center, Purdue University. All the devices were fabricated on a 5.08 mm-thick Rogers TMM3 substrate. The tuners were realized using routed PCB pieces out of a 1.5mm-thick Rogers 4350 substrate and attached to M3-L linear actuators provided by New Scale Technologies. This actuator has a 6 mm travel range with 0.5 μm step

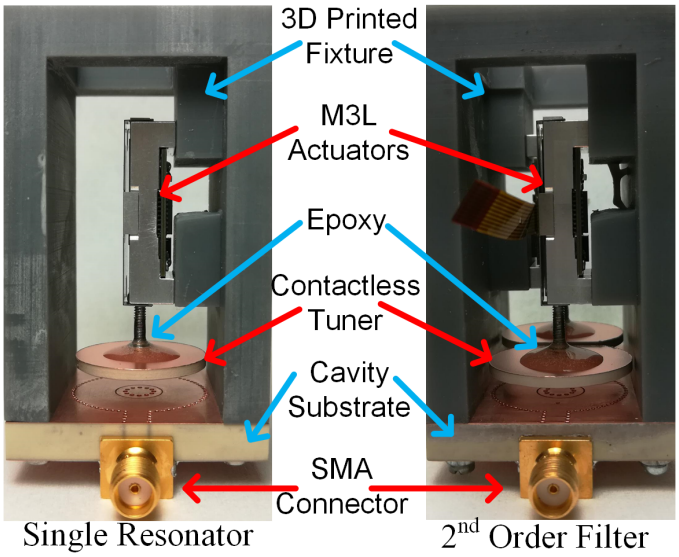

Fig. 4.15.: Picture of full assembly for single resonators and second order filters.

size. The reported actuation speed is 5 mm/sec and the displacement repeatability error is 2 μm [51]. Since the contactless tuner does not add any significant loading to the actuator, the actuator parameters are the limiting factors on the tuning speed, resolution and repeatability performance. Low cost 3D printed plastic fixtures were used to hold the actuators on top of the PCB substrates. A picture of a manufactured single resonator and a filter with the full assembly are shown in Fig. 4.15 with all the main parts highlighted.

4.5.1 Q_u measurements

Two weakly-coupled resonators were manufactured to evaluate Q_u of the resonators. Both resonators were tuned to different gaps and their Q_u was extracted from the S_{21} measurements. Resonator A was tuned from 1.7 GHz to 4.1 GHz with g from 10 μm to 1 mm. The measured Q_u is between 370 – 510. Resonator B was tuned with g starting from 40 μm up to 1.5 mm, which covered the 1.5 – 3.6 GHz frequency range with Q_u between 200 – 650. The measured Q_u values with comparison to simulations are shown in Fig. 4.16. In the implementation of Resonator A, a

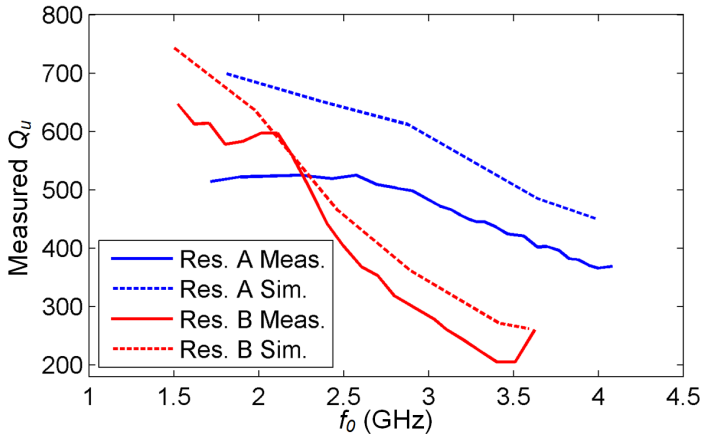

Fig. 4.16.: Extracted Q_u from weakly-coupled measurements compared to simulations.

layer of Parylene N was deposited on the tuner to enable tuning to small g without shorting the tuner and cavity. This resulted in lower Q_u than simulated specifically for small gaps.

4.5.2 Power Handling

To examine the power handling of the resonators, via-coupled resonators were manufactured and measured using the high power measurement setup shown in Fig. 4.17. The setup can provide up to 50 W of power for the band 1 – 2 GHz and 100 W for the band 2 – 4 GHz, which are the circulator's power ratings. Only the transmission path (S_{21}) was measured using input power sweep at a single frequency equal to the resonant frequency in each case. The IL of the resonator as well as a through calibration standard were measured and plotted versus the input power to the device.

Fig. 4.18(a-c) show the high power measurements for both resonators at different frequencies. Resonator A was measured at a frequency of 3.25 GHz with g equal to 70 μm, the results show that the gas breakdown occurred at 44.1 dBm (25.7 W) which lies within 13% of the predicted power from Section 4.2.4. Resonator B was measured

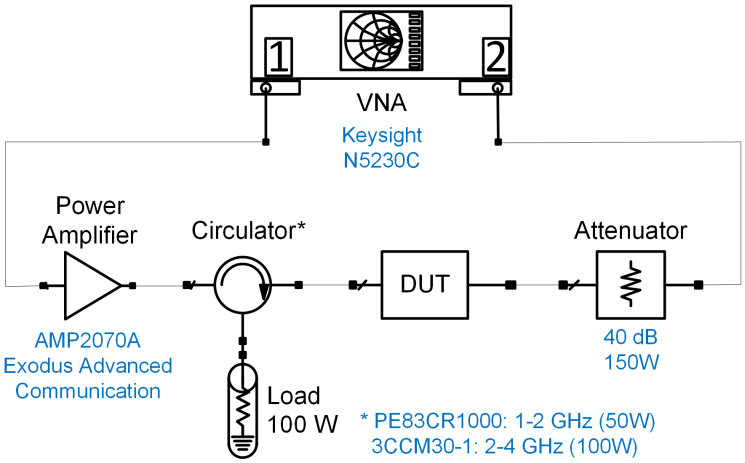

Fig. 4.17.: High power measurement setup with identified equipment models.

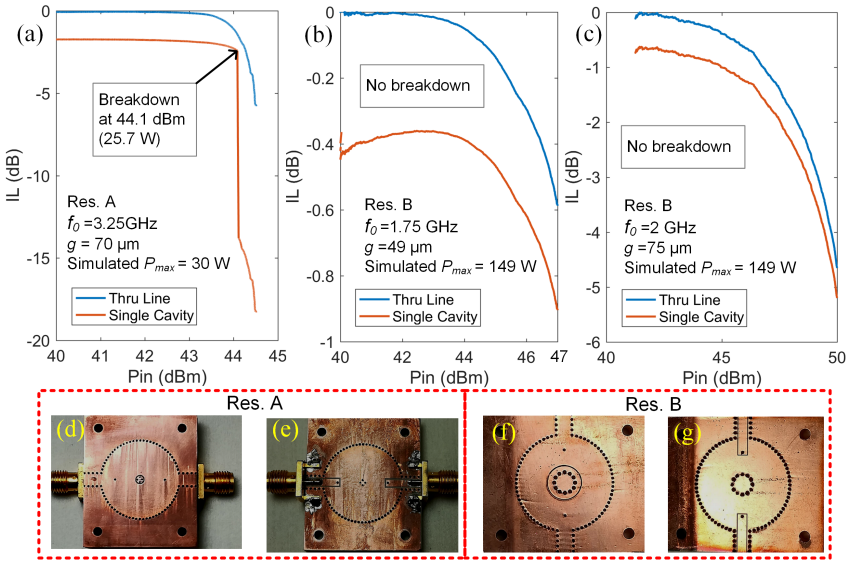

Fig. 4.18.: (a-c)High power measurements for Resonator A at 3.25 GHz and Resonator B at 1.75 GHz and 2 GHz, each case has different vertical axis scaling (d-g) Pictures of manufactured via coupled single cavity resonators for power handling test.

at 1.75 GHz up to 50 W and at 2 GHz up to 100 W. For both cases, the resonator does not experience breakdown which was expected as the predicted power handling for the resonator is around 150 W. Pictures of the via-coupled resonators used for the power measurements are shown in Fig. 4.18(d-g).

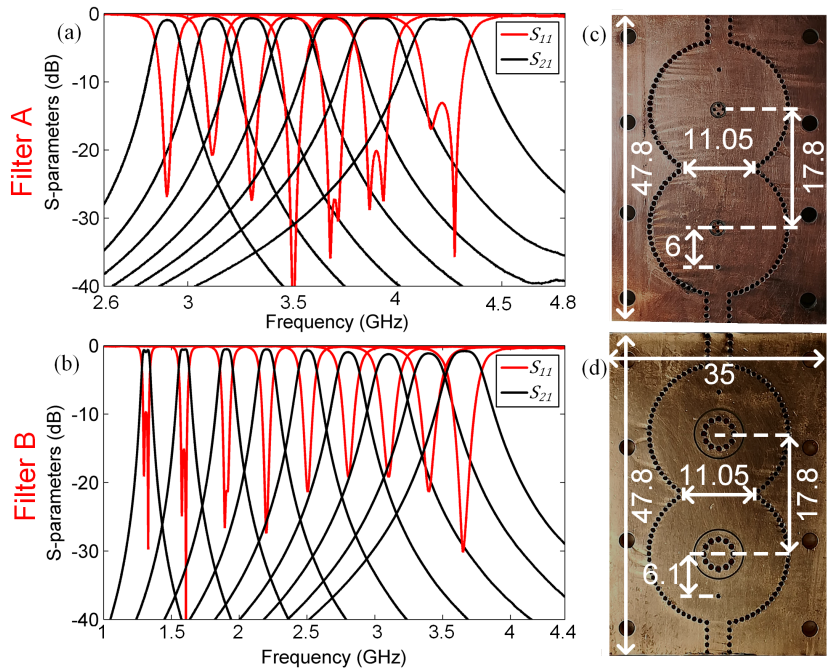

Fig. 4.19.: (a-b) Measured S-parameter of second order Filters A and B (c-d) pictures of manufactured Filters A and B.

4.5.3 Bandpass Filters

The two second order filters, designed in section 4.4, were fabricated and measured. Pictures of the manufactured filters and the measured S parameters are shown in Fig. 4.19. Filter A demonstrates a 1.46 TR from 2.9 – 4.22 GHz when the gap changes from 40 μm to 2 mm. The IL of the filter ranges from (0.64 – 0.94) dB and the RL is better than 10 dB over the full range. The FBW of the filter changes from 4% to 6.5%. Filter B shows TR equal to 2.77 from 1.3 – 3.6 GHz when the gap changes from 30 μm to 2 mm. The IL of the filter ranges from (0.571 – 1.3) dB and the RL is better than 10 dB over the full range. The FBW of the filter changes from 4.7% to 7.1%. These measured results are compared with state-of-the-art tunable resonators in Table 4.5. The used M3-L actuators cover the full range for Filter B within 0.4 seconds and cover the range from 1.3 GHz to 2.7 GHz within 13.6 milliseconds.

4.5.4 Stability and Repeatability

The via-coupled version of Resonator B as well as Filter B were the subject of long-term tests, namely stability and repeatability, as defined in section 4.2.5. Since there are two individual actuators for the filter case, different error is expected from each actuator. Thus it is critical to observe the transfer function parameters, such as BW and in-band RL, to assure that they are maintained within the acceptable range. In this study, the tuning range, for both Resonator B and Filter B, is limited to an octave (2:1) TR from 1.8 GHz to 3.6 GHz, which is achievable if tuning starts from g_0 equal to 52 μm.

For the stability test, we ran the test at a center frequency of 1.75 GHz which is lower than the start of the octave tuning range. This guarantees that the stability error of this experiment provides the high bound on the stability error for any frequency in the range. The duration of the experiment is 15 hours and the S-parameters were recorded every 1 minute. All the recorded S-parameters are plotted in the same curve in Fig. 4.20 (a-b). The variation of the center frequency versus time is plotted in Fig. 4.20 (c-d). The stability f_{err} is 1.02% for the single resonator test and 1.17% for the filter case. Also, the worst-case in-band RL for the filter is 12 dB and the 3-dB BW error is 1.33%.

The first repeatability test was performed with the single resonator at three frequency points (f_0 =1.8, 2.7 and 3.6 GHz), which corresponds to g = 52 μm, 120 μm and 1077 μm. In this test, the actuator is programmed to circulate the three points for 300 iterations with 1 minute wait at each point. The measured f_{err} is 1.53%, 0.3% and 0.11% at 1.8 GHz, 2.7 GHz and 3.6 GHz, respectively. For the filter repeatability test, the actuator is programmed to circulate four points covering the same tuning range. The extra point is at 2 GHz and the test was run for 450 cycles with 30 second wait time at each point. The measured f_{err} is 1.47% at f_{0L} and 0.28% at f_{0H}, and the worst-case 3-dB BW error is 1.88%.

Table 4.5.: Comparison with state-of-the-are tunable Resonators

Ref.	Technology	f_0 (GHz) (TR)	Q_u	P_{max} (W)	Res. Size (mm^3)
[52]	Combline - RF MEMS	6.93-7.15 (1.03)	2,320-3,850	-	18,886
[53]	Cavity - RF MEMS	2.39-2.5 (1.046)	374-1,300	-	27,000
[54]	Waveguide - RF MEMS	4.4-5.2 (1.18)	250-620	-	8,640
[5]	SIW - RF MEMS	1.9-5 (2.63)	300-650	-	509
[55]	Cavity - RF MEMS	4.07-5.58 (1.37)	300-500	0.004	750
[37]	SIW - Varactors	0.5-1.1 (2.2)	84-206	-	2,262
[56]	Cavity - Varactors	2.43-3.45 (1.42)	45-684	-	4,011
[6]	SIW - Piezo Disk	0.98-3.48 (3.55)	300-650	-	600
[4]	Cavity - Piezo Disk	2.3-4.6 (2)	360-702	-	200
[47]	Cavity - Piezo Disk	2.2-2.8 (1.27)	400-600 †	10	1,434
[57]	Cavity - Piezo Disk	6-8.25 (1.38)	2,000 †	31.6	2,035
This - Res. A	SIW - M3-L	1.7-4.1 (2.41*)	370-510	26 at 3.25 GHz	1,596
This - Res. B	SIW - M3-L	1.3-3.6 (2.85**)	200-650	$>$ 100 at 1.75 GHz	1,596

$*g_0 = 10$ μm $**$ $g_0 = 30$ μm † simulated Q_u

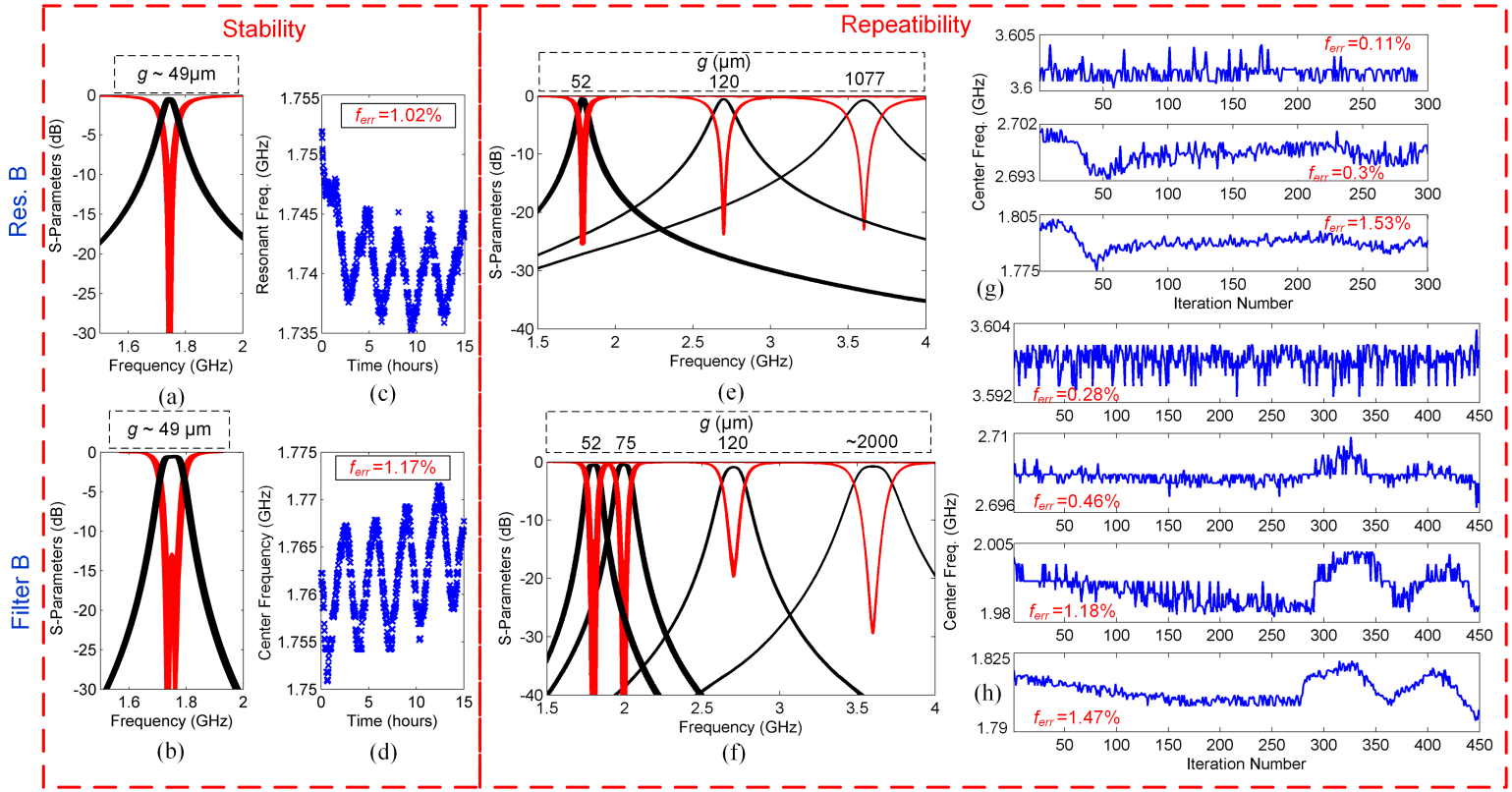

Fig. 4.20.: Long term measurements for Resonator B and Filter B (a-b) S-parameters for 15 hours stability test (c-d) Center frequency error for stability test (e-f) S-parameters for repeatability test (g-h) Center frequency error for repeatability test.

4.6 Conclusion

A novel method for tuning EVA-mode cavity resonators using contactless tuners is presented. Resonator design considerations and trade-offs are discussed. Resonators demonstrate wide tuning range up to 2.77, high measured Q_u between 200 – 650 and power handling up to 100 W. Long-term stability and repeatability tests were performed on single resonators as well as second order filters with octave tuning range and better than 1.47% frequency error was achieved. The proposed concept presents a feasible solution to enable mass production as well as reliable system integration of high frequency tunable EVA-mode cavity-based filters.

5. A NOVEL INDEPENDENTLY-TUNABLE DUAL-MODE SIW RESONATOR WITH A RECONFIGURABLE BANDPASS FILTER APPLICATION

5.1 Introduction

Tunable dual-mode resonators are among the most desirable components for microwave filters as they enable the realization of a wide variety of reconfigurable filter responses while maintaining a compact size [58]. One specifically desired feature in such resonators is the ability to control the resonant frequency of each mode independently.

Many implementations of these resonators are presented utilizing varactor-tuned microstrip resonators [59, 60]. However, due to technology limitations, these implementations suffer from low quality factor (Q) and limited tuning range. The implementation presented in [61] utilized substrate-integrated-waveguide (SIW) cavity resonators to achieve higher Q multi-mode resonator. It exhibits, however, a very low tuning range. Also, all the modes are tuned together limiting the filter reconfigurability. Other implementations using SIW resonators achieved individual tuning by loading the resonators with varactors [62]. Nevertheless, this reduced the Q values which resulted in higher losses.

In this work, we present a novel, high-Q, tunable dual-mode SIW resonator. The resonator is controlled using two vertically-moving tuners above the resonator thus enabling independent tuning for each mode. The even resonant mode maintains a Q_u higher than 200 over 59% tuning range, from 1.7 - 2.7 GHz, and higher than 150 over a 94% tuning range, from 1.7 - 3.3 GHz. The frequency of the odd mode can be controlled to be lower or larger than the frequency of the even mode with a better than 27% tuning range and a Q_u higher than 260.

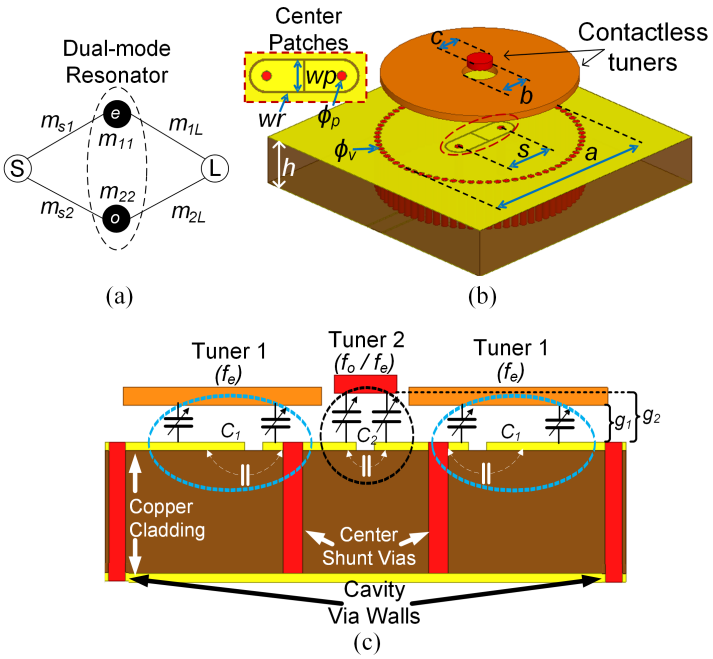

Fig. 5.1.: (a) General coupling diagram with a dual-mode resonator. (b) Proposed dual-mode SIW resonator. (c) Cross-section of proposed resonator.

In addition, this work utilizes the presented structure to implement a reconfigurable second-order bandpass filter based on a doublet-configuration. Using this configuration, the filter has a controllable finite transmission-zero (TZ) that can be located on the lower or the upper side of the passband. The center frequency of the filter is tunable from 2-3.2 GHz and the insertion loss (IL) is better than 1.1 dB over the full tuning range.

The text and figures presented in this chapter are based on the following paper: M. Abdelfattah and D. Peroulis, "A Novel Independently-Tunable Dual-Mode SIW Resonator with a Reconfigurable Bandpass Filter Application," *IEEE/MTT-S International Microwave Symposium – IMS*, Philadelphia, PA, 2018, pp. 1091-1094.

5.2 Resonator and Filter Design

5.2.1 Resonator Design

A general coupling diagram utilizing a dual-mode resonator is shown in Fig. 5.1(a). In this representation, the two modes of the resonator are in parallel and have no inter-resonator coupling. The 3-D view and the side view of the proposed resonator, with the main physical dimensions, are shown in Fig. 5.1(b-c). The resonator is constructed by electrically isolating two center patches from the top of a conventional SIW cavity resonator and connecting them to the cavity bottom through two shunt vias. This resonator can be modeled as two TEM-mode combline resonators with distributed coupling as presented in [63]. However, we will assume a simple L-C resonator model, which is sufficiently accurate for the purpose of this work. Further details on the modeling and modes' field distribution is discussed in Chapter 6. Therefore, the modes' resonant frequencies can be described by the formulas shown in (5.1).

$$f_e = \frac{1}{2\pi\sqrt{L_e C_1}}, f_o = \frac{1}{2\pi\sqrt{L_o(C_1 + 2C_2)}} \tag{5.1}$$

L_e and L_o are the inductance values associated with the even and odd modes, respectively. C_1 is the capacitance between both center patches and the resonator top layer, while C_2 is the capacitance between the center patches themselves (Fig.5.1(c)).

The ratio between the modes' resonant frequencies is found to be directly related to the inductance and the capacitance ratios as shown in (5.2).

$$\frac{f_o}{f_e} = \sqrt{\frac{L_e}{L_o}\frac{C_1}{C_1 + 2C_2}} \tag{5.2}$$

The inductance ratio (L_e/L_o) depends on the separation distance between the center vias (s). Moreover, before adding the tuners, C_2 mainly depends on the patch width (wp). To demonstrate the effect of these parameters on the frequency ratio, the resonator is simulated without the tuners and the resulting frequency ratio dependence is shown in Fig. 5.2(a).

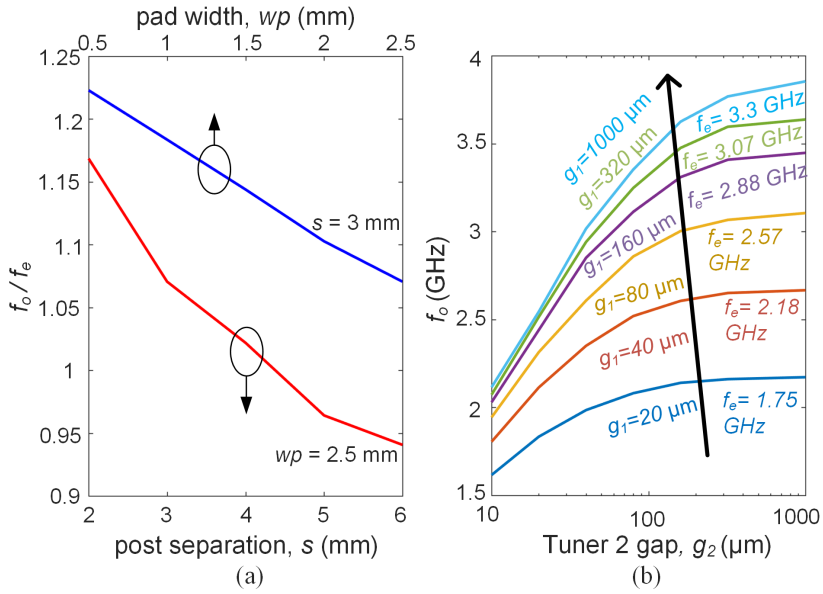

Fig. 5.2.: (a) Modes frequency ratio dependence on s and wp. (b) Both modes frequency tuning versus tuner gaps (g_1, g_2).

The capacitance dependence shown in (5.1) and (5.2) presents a suitable opportunity to independently control f_e and f_o. To enable this tuning, two flat tuners with conductive surfaces are positioned on top of the resonator creating two different controllable gaps (g_1, g_2). The presence of the tuners modifies both capacitances, C_1 and C_2, making them dependent on g_1 and g_2, respectively (Fig. 5.1). In the resulting structure, varying g_1 changes C_1 which tunes both f_e and f_o. While varying g_2 only changes C_2 which only tunes f_2, hence it tunes the frequency ratio. To demonstrate the tuning capability, g_1 is set at different values from 20 to 1000 μm while g_2 is swept from 10 to 1000 μm. The tuning simulation results are shown in Fig. 5.2(b) . It can be seen that g_2 can tune f_o to a lower or a higher value than f_e at any value for g_1.

For this work, a dual-mode resonator with the dimensions shown in Table 5.1 is designed on a 5.08 mm-thick Rogers TMM3 substrate. The tuners are cut from a 0.75 mm-thick Rogers 4003 substrate with 17.5 μm copper thickness.

Table 5.1.: Designed resonator dimensions.

Dimension	a	b	c	s	h	w_p	w_r	ϕ_v	ϕ_p
Value (mm)	20	3.6	2.6	3	5.08	2.5	0.15	0.7	0.8

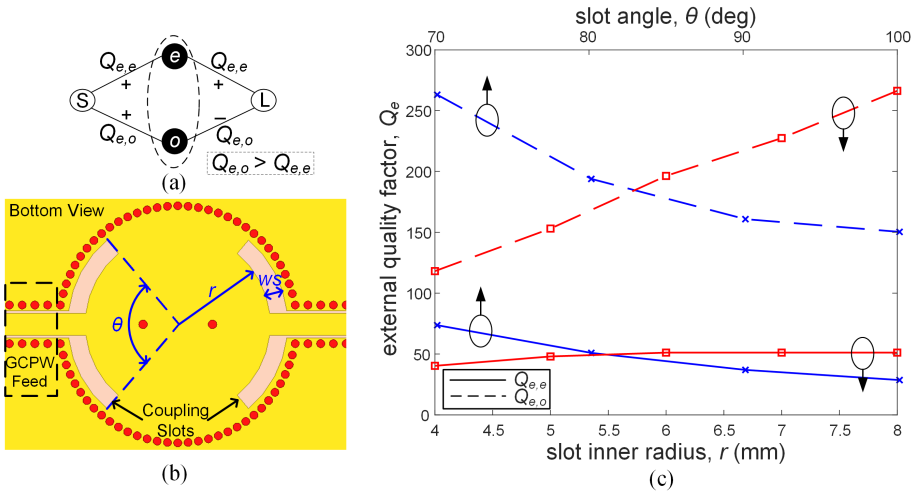

Fig. 5.3.: (a) Doublet-configuration of a bandpass filter. (b) Bottom view of resonator with external coupling slots (c) $Q_{e,e}$, $Q_{e,o}$ dependence on r and θ.

5.2.2 Bandpass Filter Design

The presented resonator is utilized to implement a reconfigurable bandpass filter. A suitable topology that fits this resonator is the doublet-configuration shown in Fig. 5.3(a). With this topology, a second order bandpass filter with a finite TZ can be realized. In order to have a TZ, we need to satisfy two conditions [64]. First, only one of the four couplings in the topology need to have the opposite polarity. Second, the external quality factor values ($Q_{e,e}$, $Q_{e,o}$) should not be equal. The location of the TZ depends on the difference between $Q_{e,e}$ and $Q_{e,o}$ in addition to the value of f_o.

To realize this topology, a grounded coplanar waveguide (GCPW), on the bottom of the cavity, is used to couple both modes to the input/output ports as shown in Fig. 5.3(b). Since the nature of this coupling is magnetic, the coupling slots are

positioned where the magnetic field for both modes is present. The values of $Q_{e,e}$ and $Q_{e,o}$ are controlled by the slot inner radius, r, slot angle, θ, and slot width, ws. Figure 5.3(c) shows the effect of r and θ on the external coupling. It is noteworthy that r has a small effect on $Q_{e,e}$ compared to $Q_{e,o}$. This effect provides us with some flexibility to control the coupling strength to each mode individually. In this work, the input/output GCPW has a 1.94 mm-wide signal line and a 0.2 mm-wide gap. Also, the dimensions chosen for the external coupling are; $r = 8$ mm, $\theta = 100°$ and $ws = 1.5$ mm.

5.3 Experimental Validation

To evaluate the tuning ranges and the modes quality factors, ($Q_{u,e}$, $Q_{u,o}$), a weakly-coupled resonator design was fabricated and measured. Each of the tuners was attached to a M3-L linear actuator in order to create the vertical motion required to tune both resonant modes. For each measurement, f_e was maintained at a certain value using tuner 1, while tuner 2 was used to tune f_o around it. A sample of these measurements are shown in Fig. 5.4(a), where f_e is set to five different values in the range 1.7-3.3 GHz. For each of these values, f_o was tuned to the minimum and to the maximum achievable frequencies. In addition, the minimum and maximum values for the frequency ratio f_o/f_e were recorded at multiple points and plotted in Fig. 5.4(b). The maximum ratio ranges between 1.1 - 1.18 while the minimum ratio ranges between 0.72 to 0.92. The measured $Q_{u,e}$ is between 150 - 400 over the full tuning range and is better than 200 for the range 1.7-2.7 GHz. The measured $Q_{u,o}$ is between 260 - 400 over the full range and it is better than 300 for the tuning states with f_e between 1.7-3 GHz.

The doublet-based bandpass filter design was also fabricated and measured. The picture of the filter with the actuators and the fixture assembly is shown in Fig. 5.5(a). The measurement demonstrated both center frequency tuning and TZ tuning. A good agreement between measurements and simulations is observed as shown in Fig. 5.5(b)

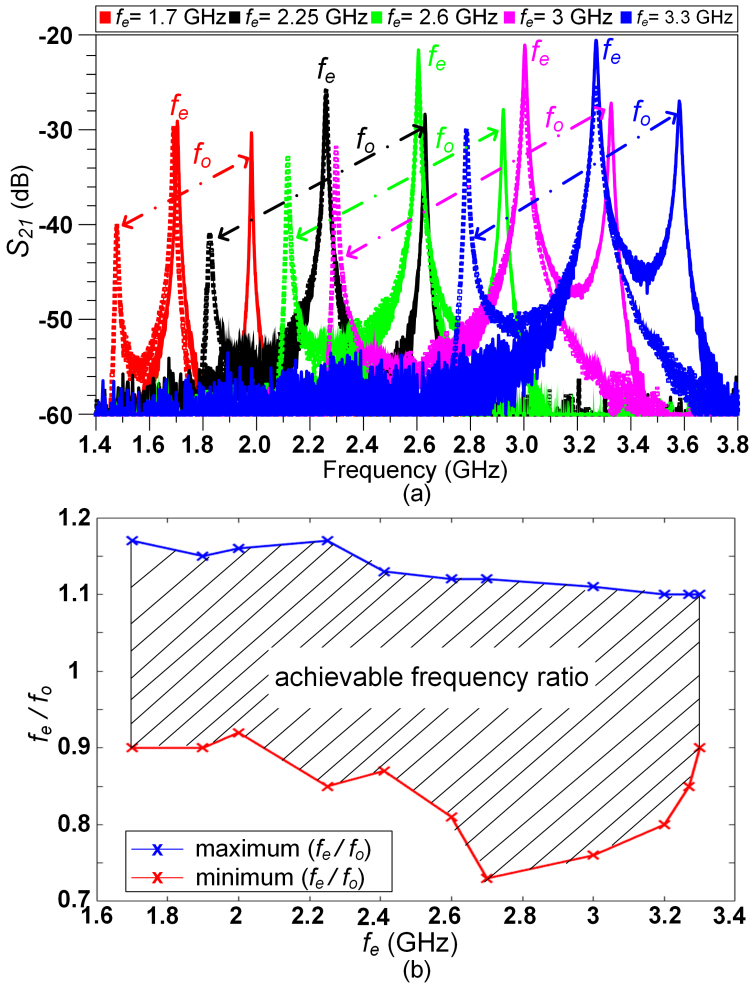

Fig. 5.4.: Measurements of weakly-coupled dual-mode resonator (a) S_{21} with f_o tuned to minimum (dashed line) and maximum (solid line) possible frequencies for each value of f_e (b) f_o/f_e versus f_e over frequency range.

for two different tuning states. The center frequency of the filter can be tuned in the range 2-3.2 GHz with TZ to the right of the passband, and in the range 2.2-3 GHz with TZ to the left. Measurements at several center frequencies with TZ on either side are shown in Fig. 5.6. The measured results show an IL between 0.65 - 1.1 dB and a return loss better than 10 dB for all tuning states.

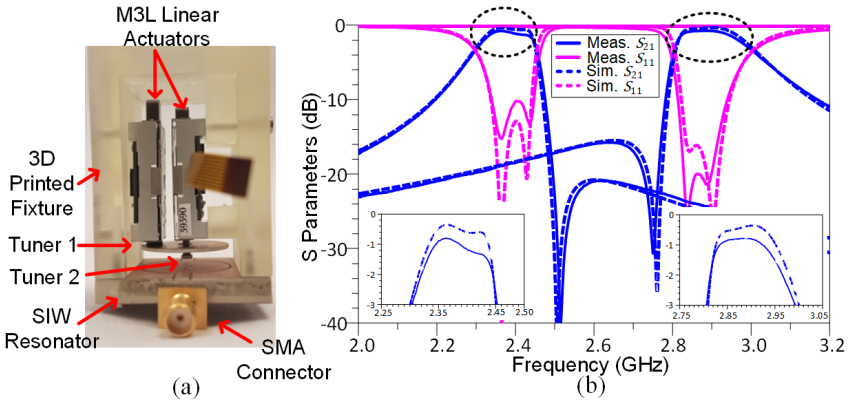

Fig. 5.5.: (a) Picture of fabricated filter with fixture and M3L linear actuators. (b) Measurement and simulation comparison for two tuning states.

5.4 Conclusion

This work presents a novel method to independently tune dual-band SIW resonators using two contact-less tuners. The resonator demonstrated a wide tuning range and a high-Q. A bandpass filter based on a doublet-configuration was designed utilizing a single dual-mode resonator. The filter demonstrated center frequency tuning from 2-3.2 GHz and a tunable TZ that can be placed on either side of the passband.

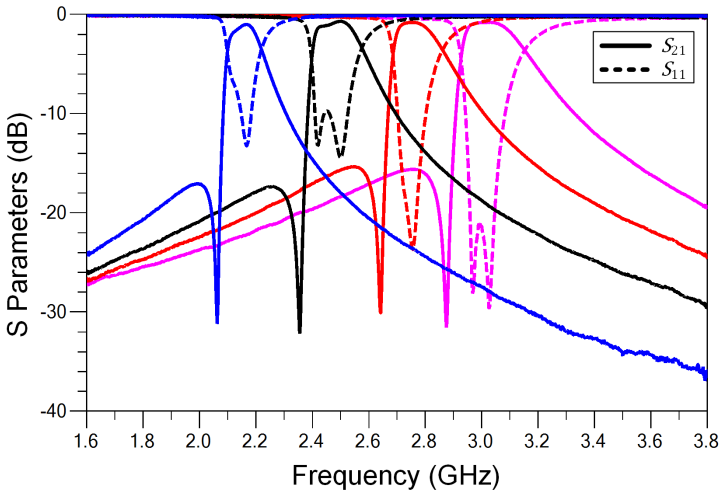

(a)

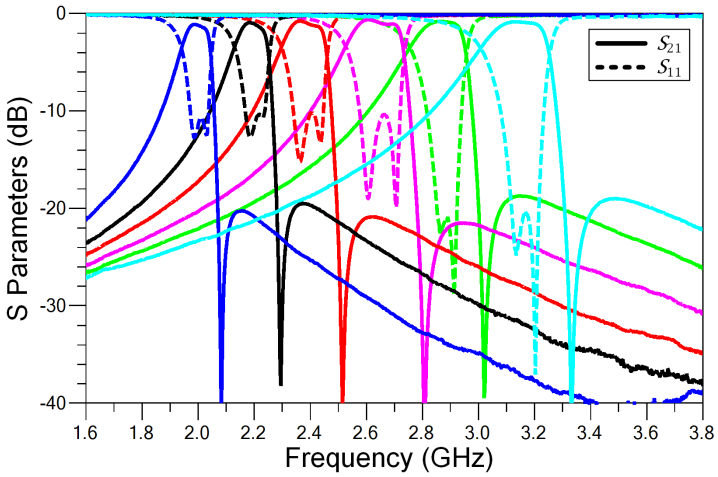

(b)

Fig. 5.6.: Measured response of doublet-based bandpass filter (a) TZ to the left of the passband (b) TZ to the right of the passband. Different color is used for each tuning state.

6. HIGH SELECTIVITY TUNABLE FILTERS WITH DUAL-MODE SIW RESONATORS IN AN L-SHAPED COUPLING SCHEME

6.1 Introduction

The advancement of reconfigurable wireless systems have raised the demand for compact, low-cost and high performance microwave and millimeter-wave tunable filters. The substrate-integrated-waveguide (SIW) technology has demonstrated great potential to implement such reconfigurable radio frequency (RF) components and systems [3,65,66]. One example is that SIW has been utilized to implement a wide range of tunable filters and diplexers because of its high RF performance, simple system integration capability and low-cost manufacturing. These implementations have demonstrated high-Q with wide TR and high power handling [3, 6, 9, 10, 39, 61, 62, 67–77].

Recent research efforts for future SIW-based tunable filters focus on achieving two major goals. The first is producing a tunable response with a constant absolute bandwidth (CABW) over the tuning range. The second is improving the response selectivity by added transmission zeros (TZs) while maintaining the size compactness. Successful solutions are expected to achieve these goals in a single design of satisfactory filter RF performance such as low insertion loss, large tuning range and high power handling. In addition, the proposed implementations are desired to offer low operation complexity and simple manufacturing and assembly.

A conventional approach to compensate for the response BW variation is to implement tunable coupling structures [39,70]. Although this provides the required control over BW, this approach increases the number of tuning elements and the complexity of the filter. Moreover, since varactors are used to control the coupling values, the power handling performance of the filter is compromised.

An alternative approach, to avoid additional tuning elements, is to implement innovative coupling structures. The structures are designed to produce coupling values with the desired variation over frequency tuning to maintain a constant BW [76–79]. This is achieved when the coupling values are also dependent on the frequency tuning structure or by using mixed magnetic and electric coupling. However, the proposed implementations, based on this approach, are limited to specific resonator structures. In addition, the passive control over the coupling variation is only demonstrated effectively over a limited tuning range.

Increasing the filter order is the traditional approach to improve the response selectivity. With more resonators, cross-coupling can be utilized to produce TZs [50]. To maintain size compactness, when increasing the filter order, resonator miniaturization techniques are employed. Several techniques are proposed to achieve miniaturization such as half-mode (HMSIW) and quarter-mode (QMSIW) resonators [71–73, 76]. Moreover, miniaturization is also obtained when using dual-mode (DM) or multi-mode resonators (MMR) [61, 62, 74, 75]. Compared to conventional single mode resonators, DM resonators are able to provide improved responses with added TZs even for second-order filters such as the doublet configuration [64, 74, 80]. Although, these techniques offer higher-selectivity in addition to compactness, they are not suitable to implement a CABW filter. This is because the TZ locations are dependent on the coupling values which results in two limitations. First, the passband and the TZ locations cannot be controlled independently because both are controlled by the coupling values. Second, as the coupling values vary with frequency tuning, the TZ locations will vary as well.

In this chapter, we propose a new utilization of SIW-based DM resonators in an L-shaped coupling scheme to effectively realize a tunable filter response with both high-selectivity as well as CABW. The presented solution achieves both goals without increasing the size or the number of tuning elements compared with a conventional filter implementation. By using an L-shaped coupling scheme, the even- and the odd-resonant modes are employed to produce the reflection zeros and TZs, respectively.

Each resonator is designed to have one contactless tuner which tunes both modes simultaneously. With the proposed structure, the DM resonator and its tuner can produce a controllable separation between the reflection zeros and TZs over the entire tuning range. This work expands on the work presented in [81] and provides more in-depth analysis on the DM resonator and its coupling scheme. The filter implemented in [81] is represented with additional discussion on the coupling topology parameters and with a proposed design procedure. Three new filter prototypes are also introduced in this paper. These filters employ techniques to either improve the out-of band rejection away from the passband or achieve higher selectivity and wider rejection bandwidth on one side near the passband. The following points provide a brief overview on the concept and the achieved performance of each of the four filters presented in this paper.

1. Filter A is in the principle filter topology, and it realizes a TZ on each side of the passband and covers the range 2.2 – 3.4 GHz with constant 3-dB ABW = 130 MHz.

2. Filter B uses additional source-load coupling, and it adds one more TZ on each side of the passband for improved out-of-band rejection and covers the range 2.5 – 3.4 GHz with constant 3-dB ABW = 130 MHz.

3. Filter C combines two TZs on the upper side of the passband to greatly improve the rejection level, and it covers the range 2.2 – 3.6 GHz with a stopband BW of 120 MHz and constant separation of 180 MHz between the passband and stopband.

4. Filter D is a counter part of filter C by re-locating the two TZs on the lower side of the passband, and it covers the range 2.3 – 3.4 GHz with a stopband BW of 57 MHZ and a constant separation of 96 MHz between passband and stopband.

The text and figures presented in this chapter are based on the following submitted paper: M. Abdelfattah and D. Peroulis, "High Selectivity Tunable Filters with Dual-Mode SIW Resonators in an L-Shaped Coupling Scheme," submitted to *IEEE Transactions on Microwave Theory and Techniques*, May 2019.

6.2 DM Resonator Design

6.2.1 Resonator Structure

The 3-D view and the cross-section view of the DM SIW resonator used in this paper are shown in Fig. 6.1. The resonator is constructed by electrically-isolating two center patches (P1, P2) from the top of a conventional SIW cavity resonator and connecting them to the cavity bottom through shunt vias. The top view of P1 and P2 is shown in Fig. 6.1 (b). This design was presented in [74] to realize an independently-tunable DM resonator using two contactless tuners. In this paper, the resonator design is modified in order to have one tuner to tune both modes simultaneously. This will be discussed in details in the tuning scheme section. The contactless tuner is a vertically moving plate on top of the resonator controlling the air gap, g_t, and it is in a pattern of two isolated conductor patches (T1, T2).

This resonator structure produces an even (e) and an odd (o) resonant modes. High Frequency Structure Simulator (HFSS) is used to plot the magnetic and electric field distribution for both modes as shown in Fig. 6.2. Based on the field distributions, the following observations should be highlighted. The even-mode electric field and the odd-mode magnetic field are symmetric about the symmetry plane. There is no even-mode electric field between P1, P2 and T2. The odd-mode magnetic field is significantly weaker near the edge of the cavity across the symmetry plane. These features will be utilized later in the filter design.

The two modes can be modeled as TEM-mode transmission-line (TL) resonators with distributed coupling as shown in Fig. 6.3 (a) [80]. C_1 represents the total capacitance between either P1 or P2 and ground. C_2 represents the total capacitance

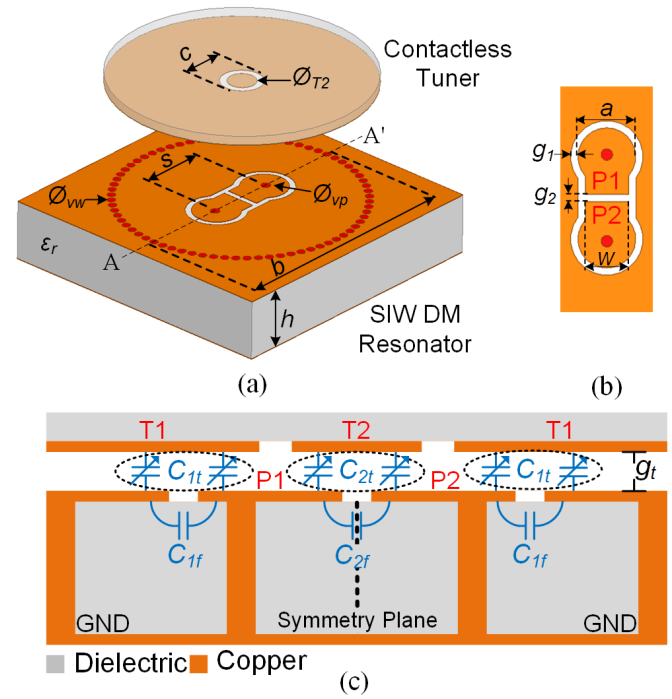

Fig. 6.1.: Proposed DM resonator (a) 3D view with main physical dimensions (b) top view of P1,P2 (c) cross-section view (A-A') with highlighted capacitances.

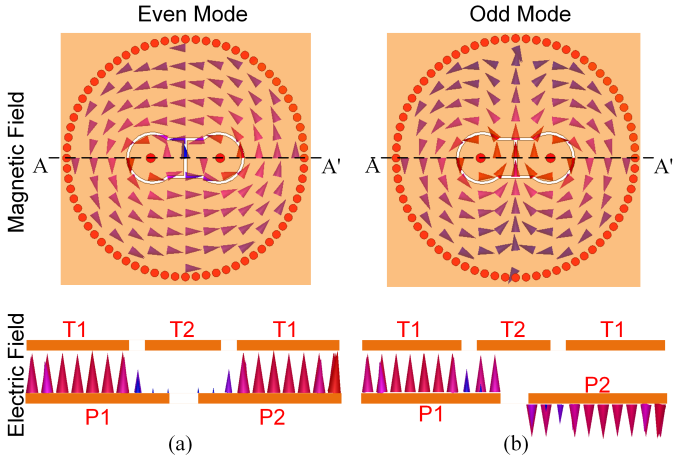

Fig. 6.2.: Electric and magnetic field distribution for (a) even and (b) odd mode. Symmetry plane is perpendicular to the line A-A'.

between P1 and P2. Each capacitance consists of a fixed capacitance (C_{1f}, C_{2f}) and a tunable capacitance (C_{1t}, C_{2t}) as highlighted in Fig. 6.1 (c). For simplicity, the TL

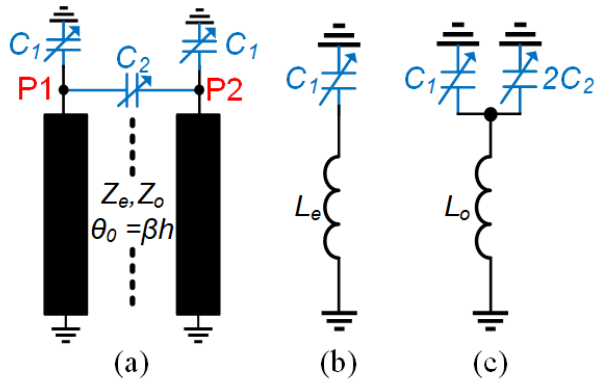

Fig. 6.3.: (a) TEM-mode TL equivalent model for DM resonator, (b) even-mode LC model, (c) odd-mode LC model.

resonators can be approximated as inductances L_e, L_o, which represent the even- and odd-mode inductances as shown in Fig. 6.3 (b-c). The inductance for either mode can be approximated from the TEM-modes parameters as,

$$L_{e,o} = \frac{Z_{e,o}}{\omega_{e,o}} \tan(\beta_{e,o} h), \tag{6.1}$$

where $Z_{e,o}$ is the mode characteristic impedance, $\omega_{e,o}$ is the mode angular resonant frequency, $\beta_{e,o}$ is the mode propagation constant and h is the cavity height. Based on the simplified LC models, the resonant frequency for each mode can be expressed as

$$f_e = \frac{1}{2\pi\sqrt{L_e C_1}}, f_o = \frac{1}{2\pi\sqrt{L_o(C_1 + 2C_2)}}. \tag{6.2}$$

Also, we define the modes' resonant frequency separation (Δf_m) as

$$\Delta f_m = f_o - f_e. \tag{6.3}$$

Due to the magnetic field nature of the modes, L_e is always larger than L_o. This results in a positive Δf_m when $C_2 = 0$. Moreover, due to the electric field nature of the modes, C_2 only increases the loading of the odd-mode as in (6.2). As a result, a negative Δf_m could be obtained with larger C_2.

6.2.2 Tuning Scheme

A key feature of the DM resonator is the use of one tuner to tune both modes. Therefore, for this resonator to be useful in implementing a CABW filter, it requires a high level of control over the two modes within the tuning range. In this section, we will demonstrate the flexibility and the simplicity of such control. This is achieved by showing that the resonator could be designed to produce the desired Δf_m variation (increasing or decreasing) with frequency tuning. Moreover, this should be demonstrated for either a positive or a negative Δf_m.

As a first step, we define the following three design ratios, based on the fixed and tunable capacitor definitions in Fig. 6.1 (C) and the resonator model in Fig. 6.3,

$$r_L = \frac{L_o}{L_e}, r_{Cf} = \frac{C_{2f}}{C_{1f}}, r_{Ct} = \frac{C_{2t}}{C_{1t}}. \tag{6.4}$$

Using these ratio definitions, we can rewrite the expression for f_o as

$$f_o = \frac{1}{2\pi\sqrt{r_L L_e(C_{1f}(1+2r_{Cf}) + C_{1t}(g_t)(1+2r_{Ct}))}}. \tag{6.5}$$

By studying the resonator model, it can be shown that the ratios in (6.4) can be used to manipulate the relation between the modes' tuning curves over varying air gap (g_t) values. This is studied in Fig. 6.4. For each study case, the tuning curve (f_e vs. g_t) is fixed, as a reference, while each ratio is swept individually to observe the variation in the curve (f_o vs. g_t). It is shown in Fig. 6.4 (a) that r_L shifts f_o uniformly for all values of g_t. However, r_{Cf} shifts f_o significantly only for large g_t when the fixed capacitance is dominant. On the other hand, r_{Ct} has significant effect for small g_t as the tunable capacitance is dominant as shown in Fig. 6.4 (b-c).

The three ratios are controlled by the physical dimensions of the cavity highlighted in Fig. 6.1. r_L is inversely proportional to the shunt vias' spacing, s. r_{Cf} is mainly controlled by w and g_2. r_{Ct} is dependent on the overlapping area between T2 and both P1 and P2. To further illustrate this feature, four DM resonators are designed using HFSS to produce the four possible cases for the Δf_m curve. Each resonator's

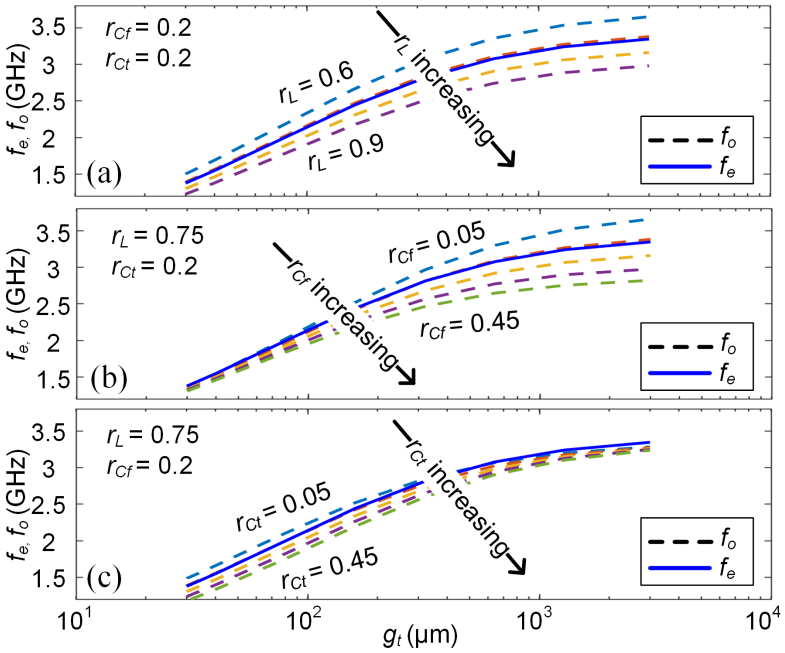

Fig. 6.4.: Design ratios control over the slope of f_o (a) r_L (b) r_{Cf} (c) r_{Ct}.

top view highlighted with the dimensions is shown in Fig. 6.5. The first two designs, shown in Fig. 6.5(a), demonstrate either increasing or decreasing positive Δf_m. The other two designs, shown in Fig. 6.5(b), demonstrate both cases for a negative Δf_m.

It should be noted that although this tuning scheme can be realized using a conventional flexible tuner implementation, the contactless tuner has several advantages [67]. First, with a contactless tuner, a uniform air gap (g_t) between the cavity and the tuner can be easily realized. This is highly desired to have accurate control on the ratios r_{Ct} and r_{Cf}. Moreover, the contactless scheme allows for larger values for g_t, which enables finer and more accurate control over Δf_m. Finally, it does not require the sensitive attachment between the membrane and the resonator. This significantly reduces the complexity of the assembly process to make it more appropriate for mass manufacturing.

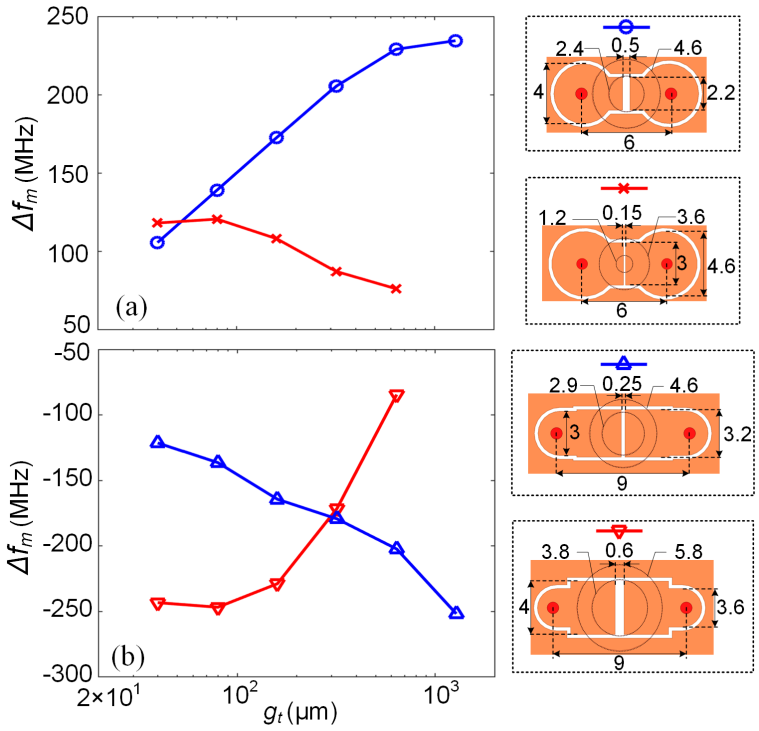

Fig. 6.5.: Four resonator examples showing increasing or decreasing Δf_m with frequency tuning (a) $\Delta f_m > 0$ (b) $\Delta f_m < 0$.

6.2.3 L-coupling Scheme

Several previous works have often used the even/odd mode resonators in a conventional doublet configuration [64, 74, 80]. In this configuration, each of the source and load nodes are coupled to both resonant modes. A single doublet coupling configuration could produce a second-order bandpass response with one TZ from one DM resonator. Despite its compactness, this configuration is not suitable for the CABW filter implementation. This is because the TZ location is dependent on the external coupling values which vary over the tuning range. Therefore, in this paper, we propose to utilize the alternative L-coupling scheme shown in Fig. 6.6(a). In this configuration, both the source and load are coupled to the even mode, while only the source is coupled to the odd mode. This is equivalent to a first-order bandpass-bandstop (BPF-BSF) cascaded filter. The even mode produces a first order bandpass

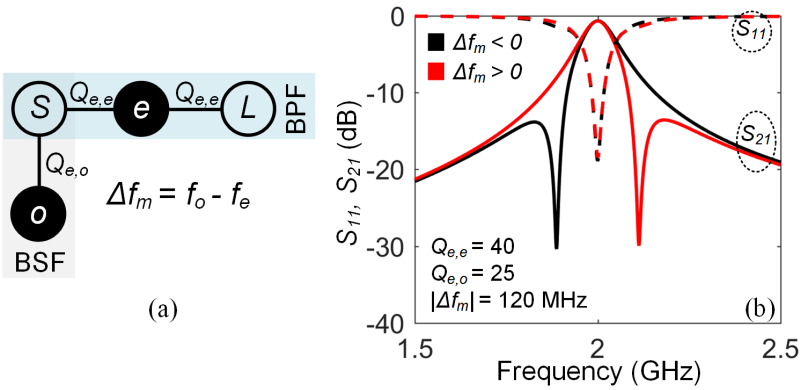

Fig. 6.6.: Proposed L-coupling scheme for DM resonator (a) coupling diagram (b) frequency response.

response while the odd mode produces a TZ as shown in the S-parameter response in Fig. 6.6(b). In this configuration, both the center frequency and TZ location are mainly dependent on f_e and f_o. The TZ can be located at the upper- or lower-side of the passband when Δf_m is positive or negative, respectively.

In Fig. 6.7, the effects of Δf_m and the external quality factor values $(Q_{e,e}, Q_{e,o})$ are studied while f_e is fixed at 2 GHz. It is shown that Δf_m controls the location of the TZ. Moreover, $Q_{e,e}$ controls the passband BW as expected from a conventional BPF while $Q_{e,o}$ controls the TZ BW as expected from a BSF. However, it is critical to notice that both Δf_m and $Q_{e,o}$ affect the in-band return loss (RL) level. This adds extra degrees-of-freedom to control the passband RL, which will be utilized later in the CABW filter design section.

The L-coupling scheme can be physically realized using coupling vias that pass through the resonator and connect to the input/output microstrip feed lines as shown in Fig. 6.8. Depending on the location of the via, it could couple to both modes or only to the even mode. This is understood by considering the magnetic filed distribution in the resonator. When the via is positioned on the symmetry plane its coupling to the odd mode experiences self-cancellation which results in coupling to only the even mode. The strength of the external coupling depends on the position of the via, which is defined by the distance, d_c, from the center. $Q_{e,e}$ and $Q_{e,o}$ dependence on d_c

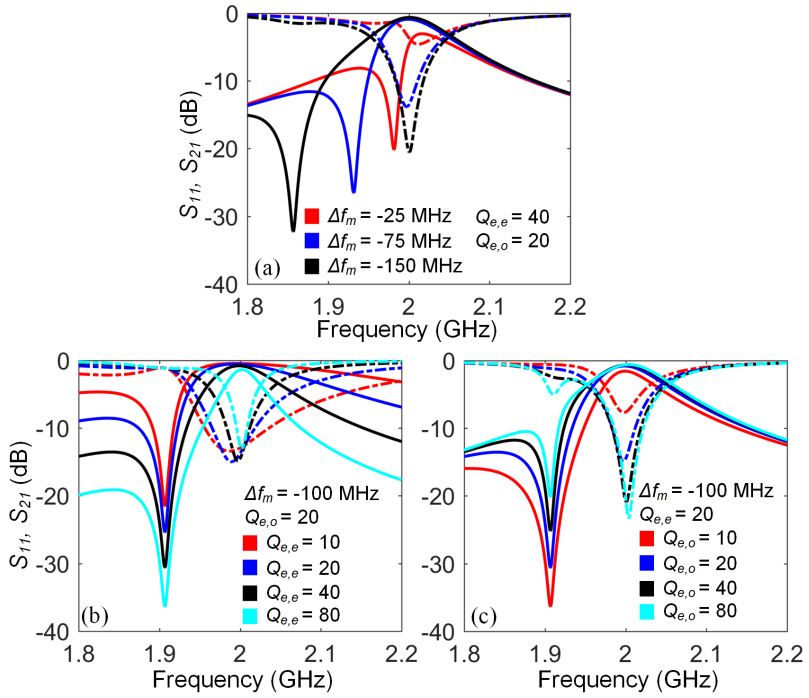

Fig. 6.7.: Effects of (a) Δf_m, (b) $Q_{e,e}$, and (c) $Q_{e,o}$ on frequency response.

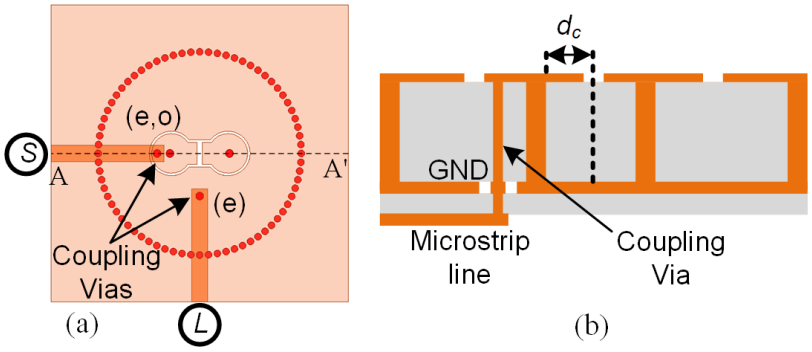

Fig. 6.8.: Physical implementation structure of the L-coupling scheme (a) top view (b) cross-section view (A-A').

can be different depending on the cavity structure. Therefore, it is studied in Fig. 6.9 for two cases with different signs for Δf_m. It can be seen that $Q_{e,e}$ could be larger or smaller than $Q_{e,o}$ depending on the resonator. This relation needs to be considered in the filter design.

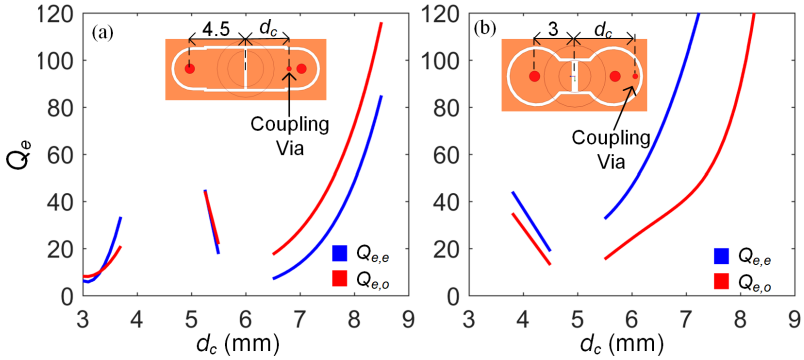

Fig. 6.9.: $Q_{e,e}, Q_{e,o}$ dependence on via spacing d_c for (a) $\Delta f_m < 0$ (b) $\Delta f_m > 0$. Discontinuities in the curves correspond to values which will short the coupling via with either the post via or the ring surrounding the post patches.

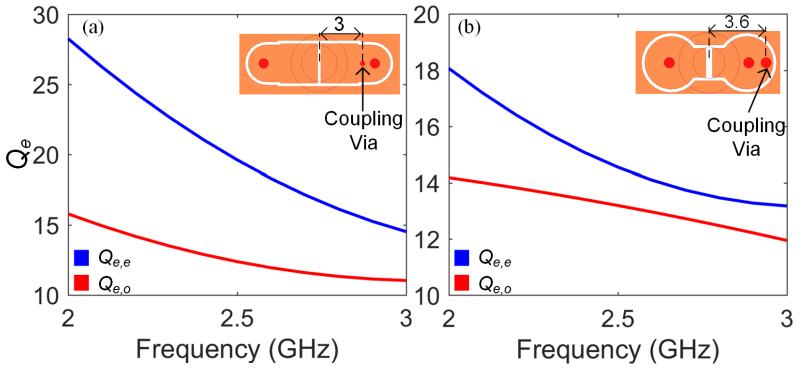

Fig. 6.10.: $Q_{e,e}, Q_{e,o}$ dependence on frequency (a) $\Delta f_m < 0$ (b) $\Delta f_m > 0$.

Finally, the values of $Q_{e,e}$ and $Q_{e,o}$ are dependent on the resonant frequency. This is illustrated in Fig. 6.10. It is shown that external coupling strength to both modes increases with frequency due to its dominantly magnetic nature. The slope of this variation could differ with the resonator design and operation frequency. Therefore, it should be always extracted and accounted for when designing CABW filters.

6.3 Constant ABW BPF Filter

6.3.1 Topology

Since one DM resonator, with the proposed coupling scheme, is able to produce a first-order response with a TZ, we could utilize two resonators to produce a second-order response with two TZs. This could be readily accomplished using the BPF topology shown in Fig. 6.11 (a). This topology was first introduced in [9] and implemented using conventional microstrip and single-mode SIW resonators to achieve a filter response with adjustable notches. When implementing the topology using DM resonators, the passband is produced by the coupling of both even-modes (e_1, e_2) through the inter-resonator coupling $(k_{12,e})$. In addition, in order to have a TZ on each side of the passband, one resonator needs to have a negative value of Δf_m while the other has a positive value. The resonator with negative Δf_m is denoted as Res. L while the other is Res. H. In order to produce a certain filter response, e_1 and e_2 might be required to have an offset in their resonant frequencies. Hence, we define the even-mode frequency separation by $(\Delta f_e = f_{e2} - f_{e1})$. As an illustration of the topology, a BPF response with 3-dB ABW of 80 MHz and RL better than 20 dB is shown in Fig. 6.11 (b). The response is overlaid with the response of Res. L and Res. H individually. This demonstrates that the passband is created in the overlapping passband of the two resonators. Also, it shows that the TZ locations are correlated with the TZs of the individual resonators. The response is also compared with a conventional second-order Chebyshev filter response with the same BW and RL level. This clearly illustrates the improved selectivity of the proposed filter due to the added TZs on each side near the passband.

For a conventional second-order filter, in order to change the RL level (or passband ripple) while maintaining the same BW, it is required to change both inter-resonator and external coupling values. However, due to the added TZs in the proposed filter topology, there are additional degrees-of-freedom. To demonstrate this flexibility, Fig. 6.12 shows different responses that could be produced by the topology. All

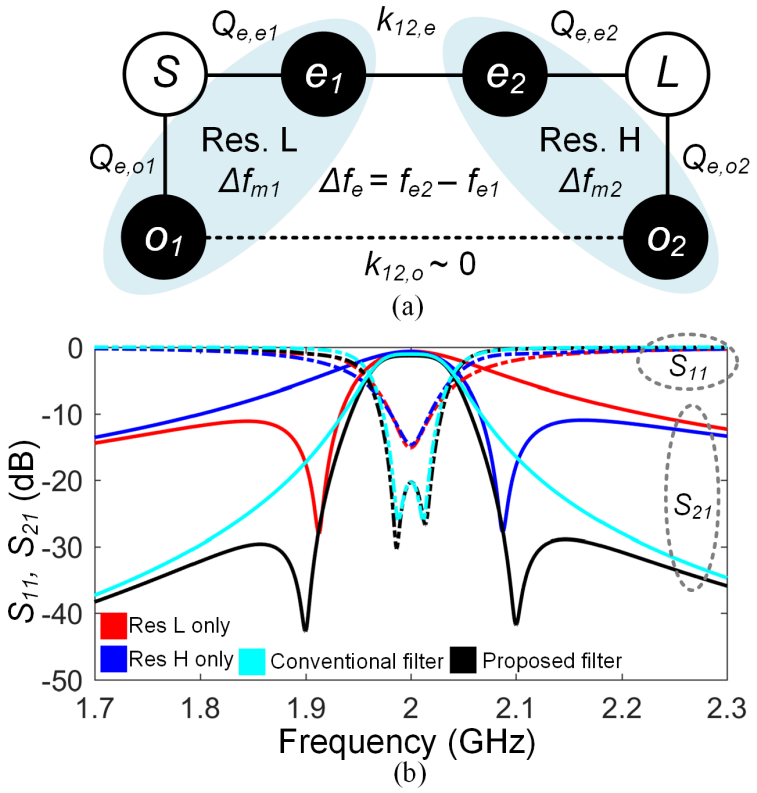

Fig. 6.11.: Proposed second-order bandpass filter topology using DM resonators (a) coupling diagram (b) static filter response with 80 MHz ABW at 2 GHz, $Q_{e,e} = 29, Q_{e,o} = 20, k_{12,e} = 0.028, \Delta f_m = 100$ MHz , $\Delta f_e = 25.6$ MHz.

responses have equal $k_{12,e}$, $Q_{e,e}$ and $Q_{e,o}$ values. While all of them have an equal 3-dB BW, the responses have different in-band RL and passband ripple as highlighted the inset in Fig. 6.12. This is enabled by manipulating the parameters Δf_m and Δf_e. This is understood by considering the effect of Δf_m on the in-band matching for an individual resonator as previously shown in Fig. 6.7 (a).

A conventional tunable BPF with fixed coupling values has an increasing BW as the frequency is increased. This is because fixed coupling values result in a fixed fractional bandwidth (FBW), which means that the ABW will increase proportionally with the center frequency of the filter (ABW=f_0×FBW). In practice, coupling values also increase with frequency which results in higher ABW variation over the tuning

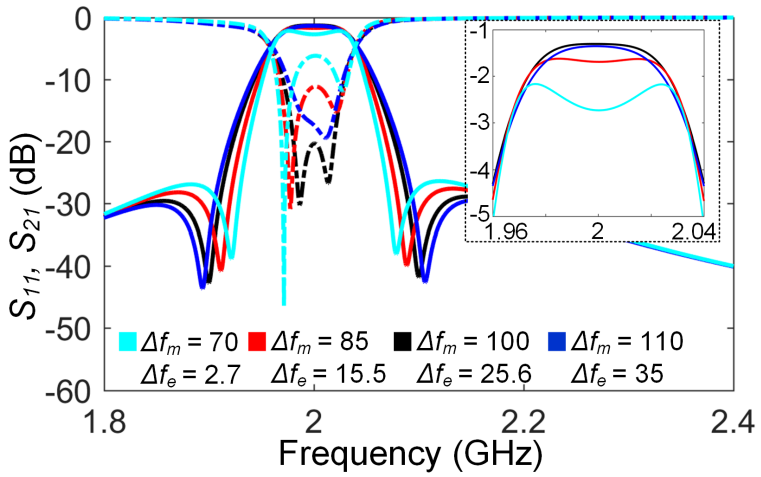

Fig. 6.12.: (a) S-parameters for different filter responses with equal ABW = 80 MHz and coupling values and different Δf_m, Δf_e (in MHz) (b) enlarged view of passband ripple

.

range. The proposed filter topology is capable of counteracting this effect due to two features. The first is the TZs, on each side, which sets limits on the ABW. The second is the additional control on the passband shape enabled by the parameters Δf_m and Δf_e. This could be achievable regardless of which mode has stronger external coupling. As an illustration, we studied the design of a filter with constant 3-dB ABW = 100 MHz and center frequency tuning form 2 GHz to 3 GHz. The following assumptions are made:

1. External coupling will vary as predicted by the individual resonator analysis presented in the previous section.

2. Inter-resonator coupling will increase linearly by 10% over the specified tuning range.

3. Res. L and Res. H can be designed to have the required curve for Δf_m over the tuning range.

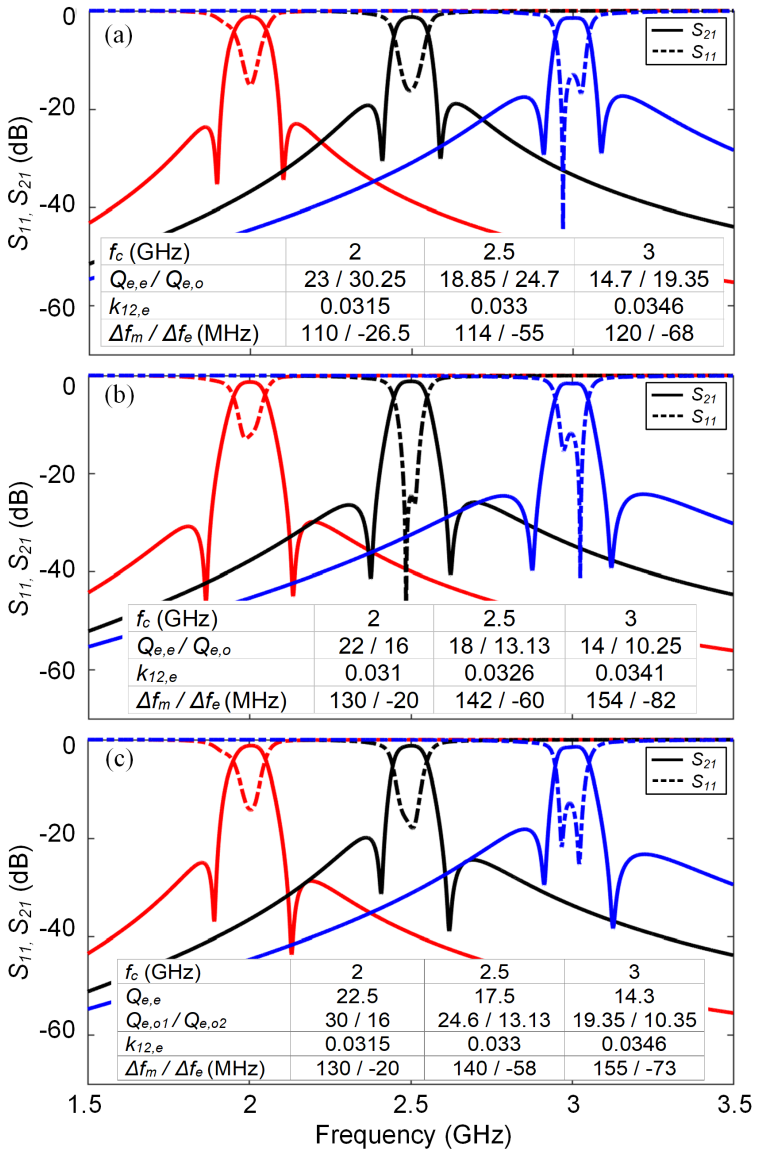

Fig. 6.13.: Illustrations of constant ABW tunable filter of 100 MHz (a) $Q_{e,o} > Q_{e,e}$, (b) $Q_{e,o} < Q_{e,e}$ (c) $Q_{e,o2} < Q_{e,e} < Q_{e,o1}$.

4. Δf_e is controlled over the tuning range by individually tuning Res. L and Res. H.

5. Acceptable in-band RL is larger than 10 dB.

6. The study also considers the following three cases relating to the available external coupling values:

(a) The odd-mode external coupling is weaker for both resonators ($Q_{e,o1} > Q_{e,e1}$, $Q_{e,o2} > Q_{e,e2}$).

(b) The odd-mode external coupling is stronger for both resonators ($Q_{e,o1} < Q_{e,e1}$, $Q_{e,o2} < Q_{e,e2}$).

(c) The odd-mode external coupling is weaker for Res. L and stronger for Res. H ($Q_{e,o1} > Q_{e,e1}$, $Q_{e,o2} < Q_{e,e2}$).

The results of this study are shown in Fig. 6.13. The filter topology is able to produce CABW responses over the specified tuning range with the given coupling variation and with acceptable RL in all cases. The only parameters controlled over the tuning range are Δf_m and Δf_e. With a conventional Chebyshev filter topology, the same coupling variation will result in a 3-dB ABW variation of 67% from 76 MHz to 127 MHz over the same tuning range.

6.3.2 Design Procedure

In this discussion, we present procedure steps to design CABW filters based on the presented topology and resonator structure. The following steps will provide the general order of steps to obtain a tunable filter response with specified ABW using both circuit model and electromagnetic (EM) simulations.

A. Resonators Initial 3D Design

Construct the design for both Res. L and Res. H based on the structure shown in Fig. 6.1. Design f_{e1} and f_{e2} to be equal to the filter center frequency. Confirm that they cover the required tuning range given the available g_t variation. Further details on tuning range optimization of single mode SIW resonator were presented in [67]. Set f_{o1} and f_{o2} to the desired TZ locations when the center frequency is at the lowest tuning state (f_{min}). Modify the resonator structure to assure that the relation $\Delta f_{m1} < 0$ is satisfied for Res. L and vice versa for Res. H.

B. External Coupling Extraction

Design the external coupling structure to produce $Q_{e,e}$ roughly equal to the value required by a Chebyshev filter response with the specified ABW and minimum acceptable RL at f_{min}. Use EM simulations to extract the relation between $Q_{e,e}$ and $Q_{e,o}$ for each resonator as in Fig. 6.9. Vary the resonant frequency over the range to extract the variation in external coupling similar to Fig. 6.10.

C. Filter Design Using Circuit Model

Find a set of values for $Q_{e,e}, k_{12,e}, \Delta f_m, \Delta f_e$ which satisfy the specified ABW and RL at f_{min}. The values of $Q_{e,o1}, Q_{e,o2}$ should depend on $Q_{e,e}$ with the same relation extracted from EM simulations. There are several solutions that satisfy the ABW with different RL levels. Change the center frequency across the tuning range while varying the external coupling values as expected from EM simulations. At each tuning state, attempt to satisfy the ABW and the RL by only varying Δf_m and Δf_e as illustrated in Fig. 6.13. If the response does not satisfy specifications across the range, the initial coupling values at f_{min} should be adjusted. Iterative process might be required to find optimum solution across the tuning range. Extract the required Δf_m versus frequency curves.

D. Δf_m Variation

Modify the structure of both resonators to satisfy the Δf_{m1} and Δf_{m2} curves using EM simulations as demonstrated in Fig. 6.5.

E. 3D Filter Design

Combine both Res. L and Res. H to construct the 3D model of the filter. Optimize the inter-resonator coupling structure to obtain the required $k_{12,e}$ at f_{min} while minimizing $k_{12,o}$. Further details about the coupling iris are discussed in the following

subsection. Use EM simulations across the tuning range to observe $k_{12,e}$ variation with tuning. Update the circuit model with expected $k_{12,e}$ variation. Fine adjustments on Δf_m and Δf_e might be needed to counteract this variation. Use EM simulations to validate the response over tuning range.

6.3.3 Filter A Implementation

Filter A, shown in Fig. 6.14, is designed in order to realize the CABW filter topology using the proposed DM SIW resonator. Res. L and Res. H are individually designed to have the required Δf_m variation across the tuning range. The dimensions for each resonator are also shown in the table included in Fig. 6.14. The inter-resonator coupling is achieved by the coupling iris between the resonators. The coupling iris is located at the symmetry line where the odd-mode magnetic field is weakest. This assures that $k_{12,o}$ is close to zero as required by the topology [58]. The external coupling vias are designed as previously shown in Fig. 6.8. Each resonator has different coupling via spacing (d_c) and coupling via diameter in order to realize the required coupling values. Filter A is designed and simulated using HFSS. It is designed to have a constant 3-dB BW of 130 MHz over the tuning range 2.2 GHz – 3.4 GHz.

6.3.4 Filter A Experimental Validation

Filter A was manufactured using conventional Printed Circuit Board (PCB) technology. A picture of the manufactured filter and the full assembly is shown in Fig. 6.15. Two M3-L linear actuators were used to provide the vertical movement for the tuners. The filter was measured using Keysight N5230C vector network analyzer. A good agreement between measurements and HFSS simulations is demonstrated in Fig. 6.16 (a) for two tuning states. The filter center frequency is tunable from 2.2 – 3.4 GHz. The tuning range is covered by tuning g_t between 80 μm and 2 mm. In all the tuning states, the 3-dB ABW was maintained constant to 130$\pm$1 MHz. Measure-

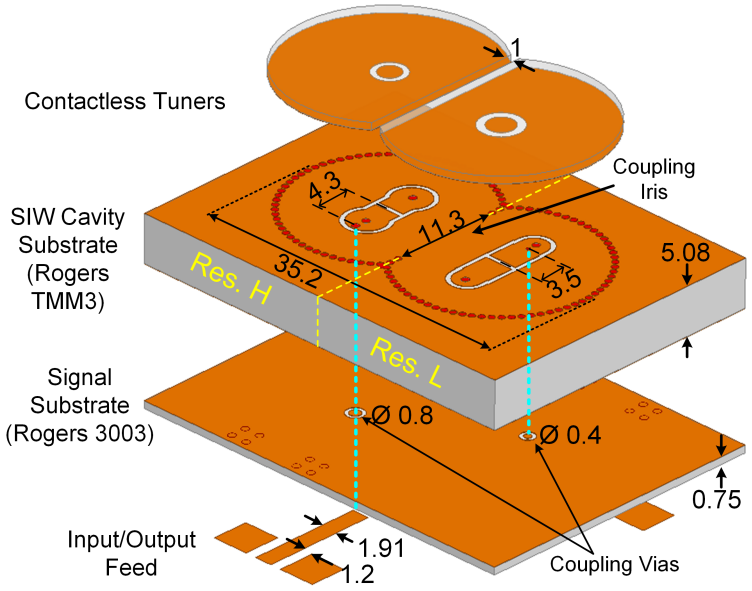

Dim.	a	c	$Ø_{T2}$	s	w	b	$Ø_{vp}$	$Ø_{vw}$	$g_{1,2}$
Res. L	3	2.3	1.45	9	3.2	20	0.8	0.7	0.25
Res. H	4	1.8	1.2	6	3				

Fig. 6.14.: 3-D view of Filter A stack up with dimensions in millimeters.

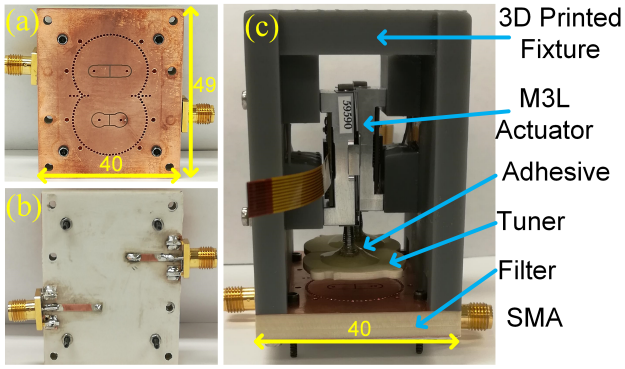

Fig. 6.15.: Pictures of the manufactured parts for Filter A (a) top view (b) bottom view (c) assembled filter with tuners and actuators. All dimensions in millimeters.

ments of several tuning states over the range are shown in Fig. 6.16 (b). The filter return loss and insertion loss (IL) are better than 15 dB and 1.36 dB, respectively. The resonators' estimated unloaded quality factor (Q_u) is between 200 – 400. The rejection of both the lower and the upper TZs ranges from 25 – 50 dB.

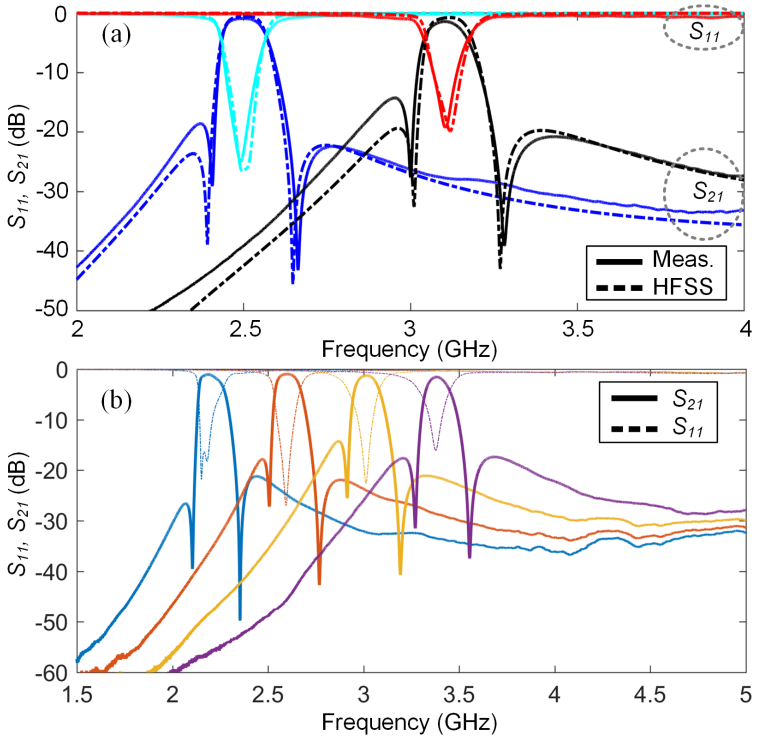

Fig. 6.16.: Filter A (a) measurements versus HFSS simulations for two tuning states (b) tunable states with constant ABW.

6.4 Improved Out-of-Band Rejection

6.4.1 Source-to-Load Coupling

It is observed from Filter A measurements that the out-of-band rejection at frequencies higher than the passband is limited to 30 dB. This rejection could be improved by modifying the topology to include intentional source-to-load coupling (k_{SL}) as shown in Fig. 6.17 (a). The added coupling path creates one additional TZ on each side of the passband. The new TZs will not be located near the passband and will not affect the filter selectivity. However, they will improve the out-of-band rejection on both sides of the passband. Realizing this coupling could be achieved by simply modifying each microstrip feed line before its termination with the coupling via. To illustrate this design modification, Filter B is designed with similar

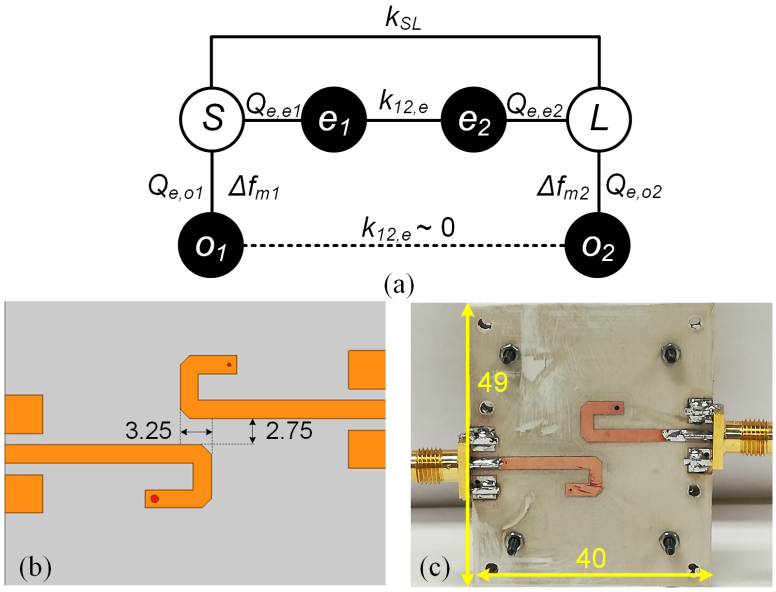

Fig. 6.17.: (a) Coupling topology with added source-to-load coupling (b) modified microstrip feed with source-to-load coupling (c) picture of the manufactured part.

dimensions to Filter A and the modified microstrip feed structure shown in Fig. 6.17 (b). The source-to-load coupling strength will depend on the length of the overlap and the spacing between the two feeding lines. Further details on the extraction of source-to-load coupling are provided in [82].

Filter B was also manufactured and measured. A picture of the new feeding structure is shown in Fig. 6.17 (c). The measurements versus simulations for the tuning state with 2.5 GHz center frequency is shown in Fig. 6.18 (a). In addition, several measured tuning states are shown in Fig. 6.18 (b). Filter B maintains a constant ABW of 130±1 MHz over the range 2.5 GHz – 3.4 GHz. The IL is between 1.37 dB – 1.97 dB and the RL is better than 10 dB. The out-of-band rejection at higher frequencies (around 5 GHz) is improved by 19-29 dB proving the advantage of the source-to-load coupling as shown in Fig. 6.19. Both filters A and B were measured up to 8 GHz to observe their spurious responses. The filters show better than 20 dB rejection up to more than 6 GHz.

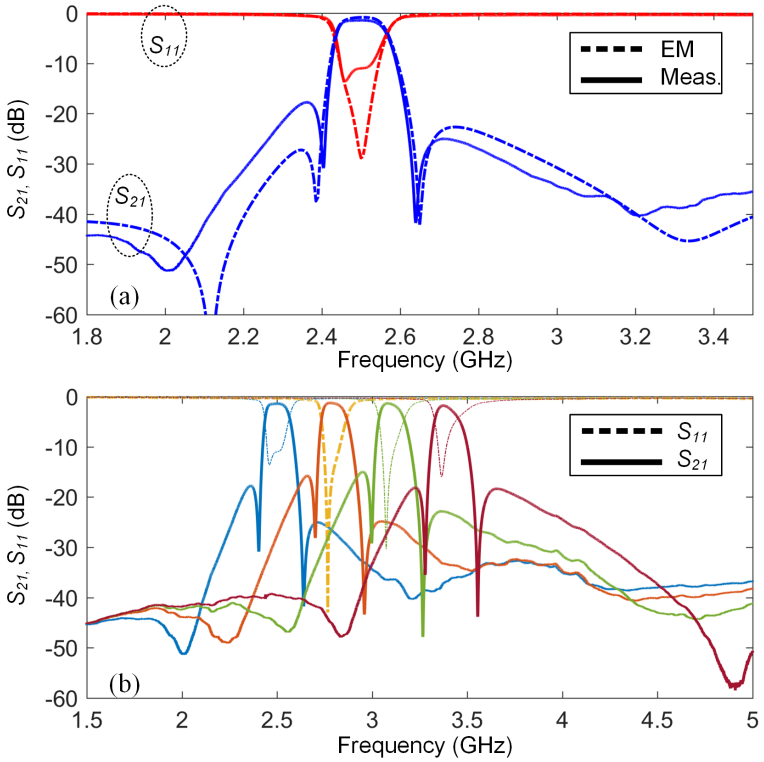

Fig. 6.18.: Filter B (a) measurements versus HFSS simulations for one tuning state with 2.5 GHz center frequency (b) tunable states with constant ABW.

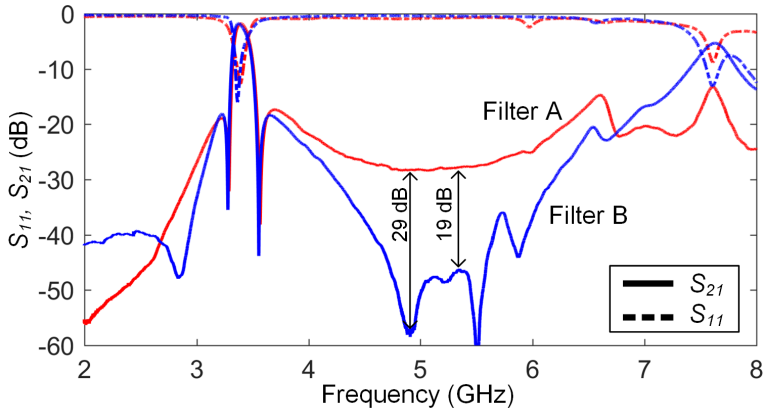

Fig. 6.19.: Measured wide band frequency response for Filters A and B showing improved out-of-band rejection for Filter B.

6.4.2 Combining TZs on the Same Side

In some applications, a tunable filter with higher selectivity might be more desired than a CABW filter. This could be due to a blocker that is located at a fixed spacing

from the filter passband. This could be addressed by combining TZs on one side of the passband where the blocker is located. As a result, a higher attenuation and a wider stopband bandwidth (BW_S) can be obtained at the blocker frequency. We can achieve this response by using the same filter topology we presented in the previous section. However, for this case, both DM resonator will have the same sign for Δf_m. Filter responses achieved by this topology are shown in Fig. 6.20 (a-b). The passband is produced by e_1, e_2 and the stopband is produced by o_1, o_2. In the previous section, the coupling $k_{12,o}$ was assumed to be practically zero. This was acceptable as o_1 and o_2 are widely separated. However, when they are set at the same frequency, any non-zero value will be observable. In fact, a non-zero $k_{12,o}$ is desired to increase BW_S. In general, if $k_{12,o}$ is about $10\times$ smaller than $k_{12,e}$, the stopband will have larger BW without deteriorating the rejection. One important requirement, when using this topology, is to have a stronger coupling for the odd-modes ($Q_{e,o} < Q_{e,e,}$) in order to achieve higher rejection levels in the stopband.

The frequency spacing between the passband (f_c) and the stopband (f_S) can be controlled using Δf_m of the resonators. Since, the DM resonator design provides Δf_m control over the tuning range, we can have a fixed value for the separation over the tuning range. This is demonstrated in Fig. 6.20 (c), where the stopband has a $BW_S = 100$ MHz at a rejection level of 30 dB. Also, the separation between the passband and the stopband is fixed at 185 MHz. A similar implementation can be realized for a stopband to the left of the passband by reversing the sign of Δf_m. Since we have flexibility in controlling Δf_m, an increasing or decreasing separation between the passband and the stopband can be also obtained. In the following discussion, we present the implementation of Filters C and D, which realize responses with fixed stopband separation on the higher side of the passband for Filter C and on the lower side for Filter D.

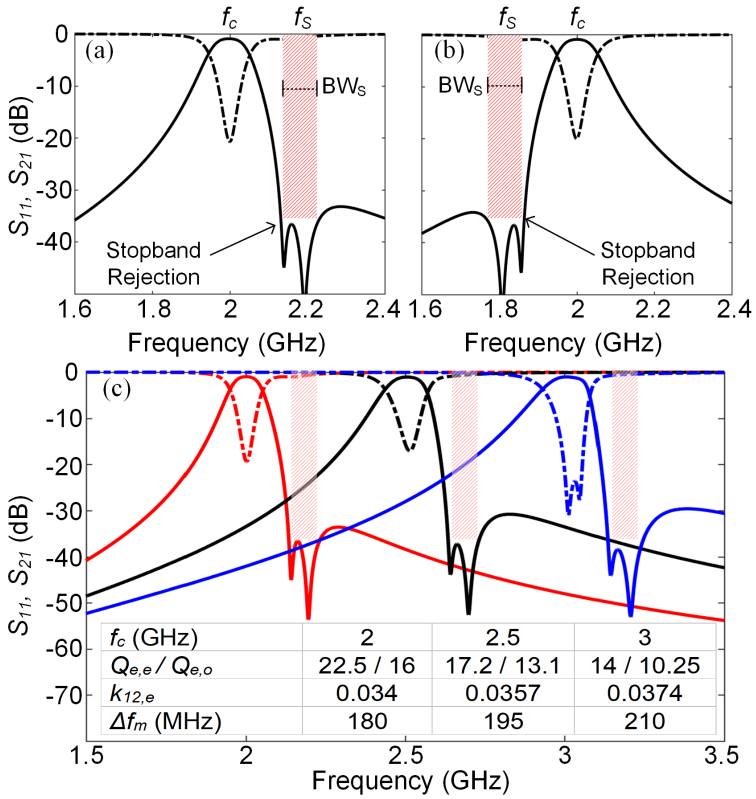

Fig. 6.20.: (a) Stopband on the upper side of passband (b) stopband on the lower side of the passband (c) tunable response with constant separation of 180 MHz between passband and stopband.

Filter C

The top and bottom views of Filter C are shown in Fig. 6.21 (a-b). The filter is designed using the same stack-up shown in Fig. 6.14, however both resonators are identical. The filter also utilizes source-to-load coupling, as shown in Fig. 6.21 (b), in order to maintain a good level of rejection away from the passband on both sides. The manufactured filter pictures are shown in Fig. 6.21 (c-d). The assembly of the filter is similar to both Filters A and B. The manufactured filter demonstrated center frequency tuning between 2.2 GHz – 3.6 GHz. A comparison between simulations and measurements is shown in Fig. 6.22 (a) for the state $f_c = 3.2$ GHz. The results for different tuning states are shown in Fig. 6.22 (b). The filter has an IL between 0.9

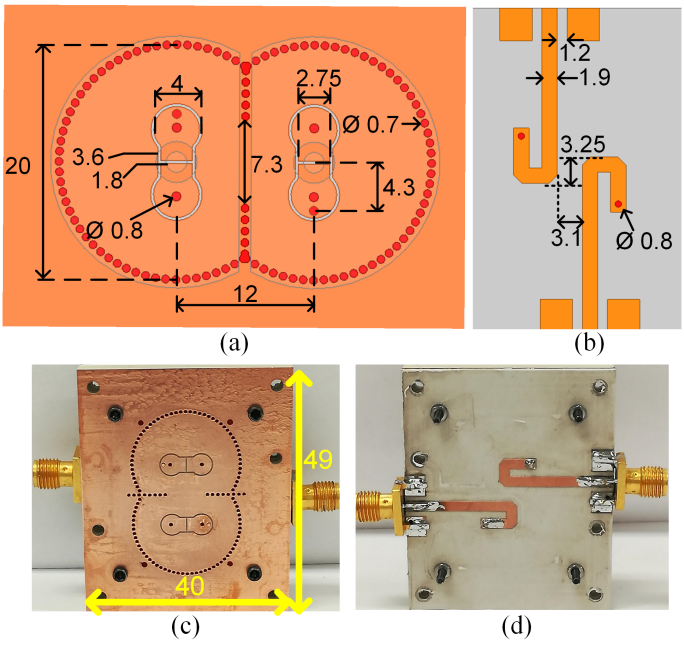

Fig. 6.21.: Filter C (a) top view (b) bottom view (c-d) pictures of the manufactured prototype.

dB – 1.6 dB and RL better than 16 dB. A stopband rejection level of at least 28 dB is consistently satisfied, across the range, with $BW_S = 120$ MHz and $f_S - f_c = 180$ MHz. The passband 3-dB BW is between 88 – 139 MHz.

Filter D

In order to implement Filter D, with improved selectivity on the lower side of the passband, some modifications were required, namely the external coupling structure. For this resonator, when using the coupling via structure, the odd-modes have weaker external coupling which results in poor rejection in the stopband. On the other hand, a grounded coplanar waveguide (GCPW) feeding structure with a coupling slot provides the required relation between the coupling values. The top and bottom views of Filter D with the modified coupling structure are shown in Fig. 6.23 (a-b). The coupling slot is a conventional coupling element that was implemented in several previous works [70, 74].The coupling strength is controlled by the the slot's radius,

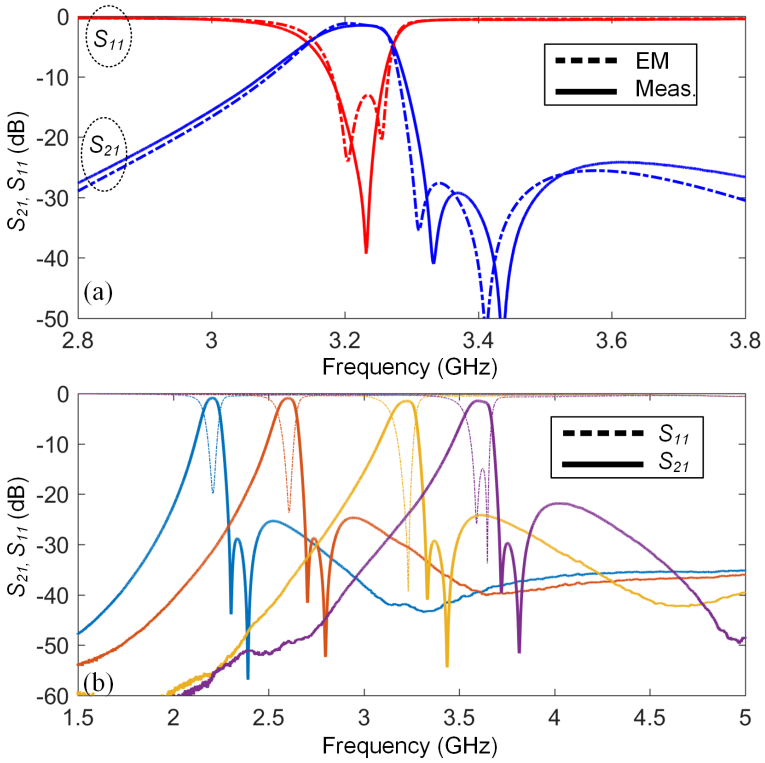

Fig. 6.22.: Filter C (a) measurements versus HFSS simulations for one tuning state (b) measured tunable states.

radial angle and width. Pictures of the manufactured Filter D are shown in Fig. 6.23 (c-d). A comparison between the simulated and the measured response of Filter D is shown in Fig. 6.24 (a) for center frequency of 2.5 GHz. The filter achieves center frequency tuning from 2.3 GHz – 3.4 GHz. The IL varies between 1.5 dB and 2.8 dB while the RL is better than 12 dB. The stopband rejection level is higher than 28 dB with $BW_S = 57$ MHz and $f_c - f_S = 96$ MHz. The passband 3-dB BW is between 49 – 59 MHz. Furthermore, a wide band frequency measurement for Filters C and D is shown in Fig. 6.25. The measurements show no significant spurious resonance up to 8 GHz for both filters.

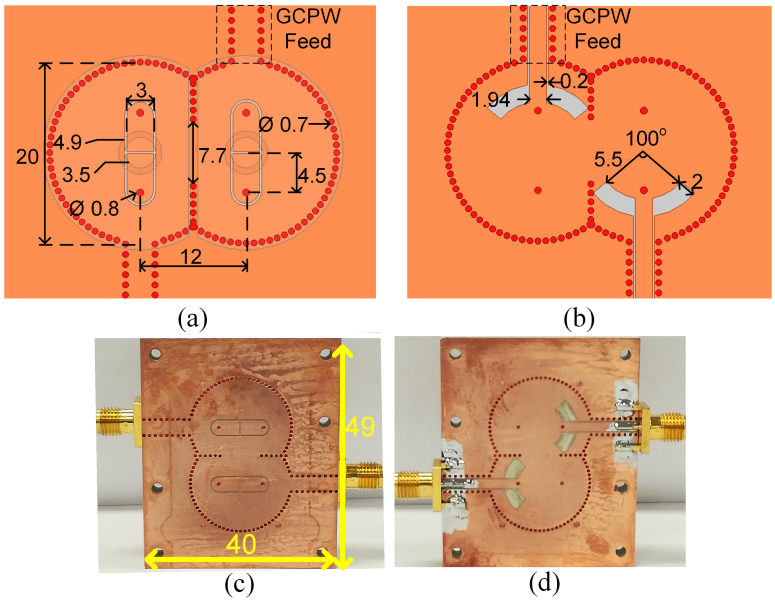

Fig. 6.23.: Filter D (a) top view (b) bottom view (c-d) pictures of the manufactured prototype.

6.5 Comparison

Table I shows a comparison between the filters presented in this paper and state-of-the-art CABW tunable filters. The comparison shows that our implementations exhibit a much lower insertion loss when compared to microstrip implementations. This is due to the higher Q_u offered by the SIW resonator with mechanical tuning. The ABW performance of Filters A and B shows that the proposed coupling topology has enabled the realization of truly constant ABW, with negligible variation over the tuning range, without requiring tunable coupling structures. Compared to varactorless implementations, Filters A and B has demonstrated wider tuning range and higher selectivity. Furthermore, the performance of Filters C and D has illustrated the advantage of combining TZs to increase the rejection BW near the edge of the passband (BW_S) and maintain its separation (Δf_S) from the center frequency. This is achieved while maintaining an acceptable ABW variation and without compromising the insertion loss.

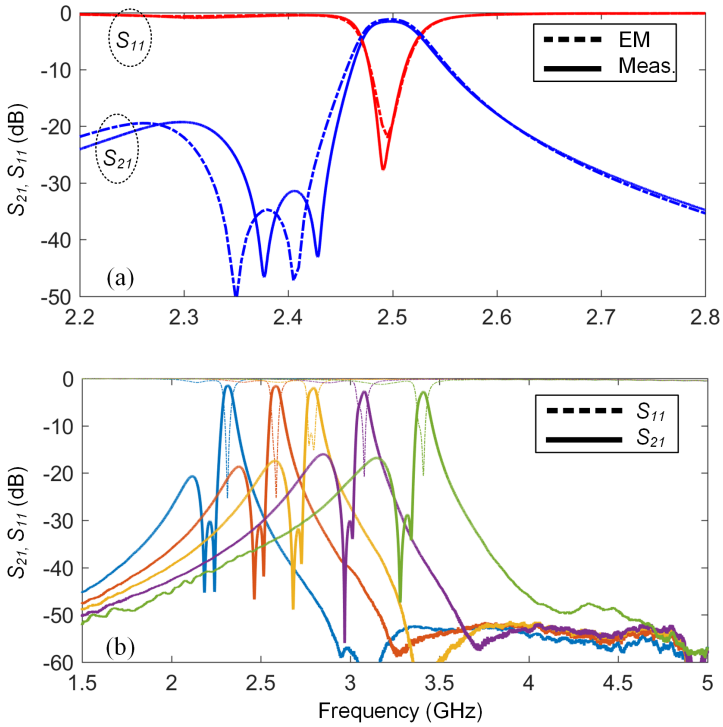

Fig. 6.24.: Filter D (a) measurements versus HFSS simulations for one tuning state (b) measured tunable states.

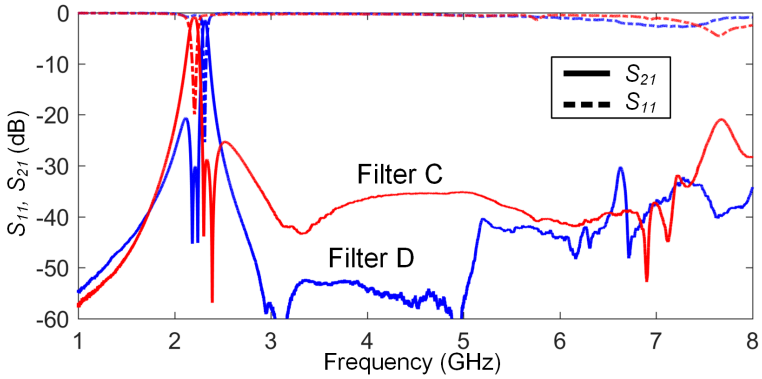

Fig. 6.25.: Wide band frequency measurements for Filters C and D.

Table 6.1.: Comparison of implemented filters with state-of-the-art CABW Filters

Ref.	Tech.	f_c (GHz) (TR)	ABW (MHz)	IL (dB)	Order/TZ	$BW_S/\Delta f_S$ (MHz) Rej. (dB)	# Tuners M	# Tuners V/S (B)	Size (λ_0^3) at f_{min}
[83]	μstrip V + S	0.55-1.9 (3.45)	86-98	3.2-4.4	2/0	NA	0	6 (4)	0.006×10^{-3}
[84]	μstrip/ V	0.95-1.48 (1.56)	114-120	3.5-4.4	4/2	26-48 / 130 at 34 dB	0	4 (2)	0.154×10^{-3}
[85]	μstrip/ V	1.24-1.72 (1.39)	92-97	4.6-5.4	4/4	NA	0	4 (2)	0.053×10^{-3}
[86]	μstrip/ V	2.41-2.73 (1.13)	201-219	1.7-2.7	2/0	NA	0	2 (2)	0.023×10^{-3}
[59]	μstrip/ V	0.6-1.03 (1.72)	80-90	1.8	2/1	28-30 / 50-60 at 15 dB	0	3 (1)	0.003×10^{-3}
[87]	μstrip/ V	0.89-1.13 (1.27)	43.4-50.2	3.2-4.3	4/2	9-13 / 44-52 at 28 dB	0	4 (1)	0.081×10^{-3}
[79]	Waveguide Motor	14.8-16.2 (1.09)	287-305	0.4-0.6	5/0	NA	1	0	1.13

continued on next page

Table 6.1.: *continued*

Ref.	Tech.	f_c (GHz) (TR)	ABW (MHz)	IL (dB)	Order/TZ	$BW_S/\Delta f_S$ (MHz) Rej. (dB)	# Tuners M	# Tuners V/S (B)	Size (λ_0^3) at f_{min}
[88]	Dielectric μstrip/ V	0.67-0.98 (1.46)	42-47	2.9-5.3	2/2	14-38 / 72-102 at 34 dB	0	2 (2)	0.042×10^{-3}
[76]	HMSIW Piezo	1.8-2.3 (1.24)	136-142	1.3-2	2/0	NA	2	0	0.73×10^{-3}
[73]	HMSIW/ V	1.11-1.5 (1.35)	75	2.62-7	2/0	NA	0	6 (3)	0.2×10^{-3}
[72]	HMSIW Piezo + V	1.2-1.6 (1.33)	113-141	1.2-3.4	2/0	NA	0	6 (6)	0.144×10^{-3}
[77]	SIW MEMS S	3.9-4.75 (1.22)	339-416	1.3-1.65	4/1	27-73 / 174-365 at 40 dB	0	3 (3)	3.45×10^{-3}
[39]	SIW/ V	0.55-1.1 (2)	60	1.9-2.3	2/1	Reconfigurable	0	80 (5)	0.046×10^{-3}
[70]	SIW Piezo + V	0.8-1.43 (1.79)	24.7-25.3	1.6-3.1	2/0	NA	2	4 (3)	0.046×10^{-3}

continued on next page

Table 6.1.: *continued*

Ref.	Tech.	f_c (GHz) (TR)	ABW (MHz)	IL (dB)	Order/TZ	$BW_S/\Delta f_S$ (MHz) Rej. (dB)	# Tuners M	# Tuners V/S (B)	Size (λ_0^3) at f_{min}
Filter A	**DM-SIW M3-L**	**2.2-3.4 (1.55)**	**129-131**	**0.98-1.38**	**2/2**	**23-27 / 153-165 at 28 dB**	**2**	**0**	**1.4×10^{-3}**
Filter B	**DM-SIW M3-L**	**2.5-3.4 (1.36)**	**129-131**	**1.37-1.97**	**2/4**	**23-40 / 146-163 at 28 dB**	**2**	**0**	**2.06×10^{-3}**
Filter C	**DM-SIW M3-L**	**2.2-3.6 (1.63)**	**88-139**	**0.9-1.6**	**2/4**	**120 / 180 at 28 dB**	**2**	**0**	**1.28×10^{-3}**
Filter D	**DM-SIW M3-L**	**2.3-3.4 (1.47)**	**49-59**	**1.5-2.8**	**2/2**	**57 / 96 at 28 dB**	**2**	**0**	**1.46×10^{-3}**

TR = f_{max}/f_{min}

BW_S = Rejection BW due to TZ near the passband

Δf_S = Separation between center of rejection BW and center frequency ($f_S - f_c$)

M = Mechanical Tuner, V = Varactor, S = Switch, B = Bias Lines

Since the presented filter do not use any varactors, they are expected to demonstrate improved power handling capability in terms of non-linear behavior as well as the peak RF power handling. Also, the contactless tuner scheme enables tuning using larger air gap (g_t), this is expected to have further improvement on the power handling capability and lower operation sensitivity [67]. In addition, the filters have the potential to offer wider tuning range with further design optimizations and starting from lower g_t values.

6.6 Conclusion

This chapter has presented high-selectivity and constant absolute bandwidth tunable filters based on DM SIW resonators and their L-shaped coupling scheme. The analysis and design considerations of the resonator are discussed by highlighting the implemented coupling and tuning schemes. In this implementation, each resonator is capable of producing a reflection zero and a transmission zero while being controlled using a single tuner. The resonator design has the capability of controlling the modes' separation with tuning enabling control over the absolute bandwidth variation. Four tunable filters were presented to demonstrate the design versatility and flexibility. The first filter has demonstrated a wide tuning range with constant absolute bandwidth and a TZ on each side of the passband. The next one uses the source-load coupling technique to add two more transmission zeros to further improve the out-of-band rejection. The last two filters demonstrated higher and constant selectivity by combining both transmission zeros on one side of the passband.

7. SUMMARY AND FUTURE WORK

7.1 Summary

In the past decade, several research efforts have focused on the design of tunable RF filters using mechanically tunable EVA-mode cavity resonators. These efforts have demonstrated high performance such as high-Q, low loss, wide TR and high power handling. However, the utilization of such filters in modern communication systems remains limited due to several practical challenges. The main purpose of this dissertation is to address some of these challenges from both aspects; RF performance and operation reliability.

One of the major challenges, addressed in this dissertation, is maintaining a constant absolute bandwidth for both bandstop and bandpass filters. Compared to other approaches in the literature, we presented solutions that achieve the goal using passive-compensation techniques (i.e. without additional tuning for BW). In addition, the solutions avoided the use of any varactors in order to maintain the filter performance in terms of loss, non-linearity and power handling.

The second challenge, addressed in this dissertation, is improving the filter response selectivity by adding transmission-zeros. The presented designs utilized novel techniques using dual-mode SIW resonators in order to produce additional TZs while maintaining compact filter size. Compared to other techniques, the ones presented are better suited to tunable filters producing acceptable response over different tuning states.

The final challenge is pertaining to the operation reliability of the filters. Firstly, we proposed, for the first time, the contactless tuning concept which resolves the major limitation of using flexible tuners. Moreover, we have demonstrated the advantages of this alternative approach and provided all the design optimization steps

required to maintain high performance when using it. Secondly, we presented the first electronic monitoring and control system for high frequency, electro-statically tunable MEMS cavity filters. The proposed inductive-based sensing and actuation is implemented with a control loop which adjusts the deflection of the MEMS diaphragm to produce the desired tuning state. The system was demonstrated on a mm-wave BSF showing potential in high frequency applications.

7.2 Contribution

The contributions in this work are summarized as follows:

1. Chapter 2 demonstrated two passively-compensated tunable quasi-absorptive bandstop filters. The filters operate in the 12-20 GHz and the 23-45 GHz frequency ranges. The filters demonstrated more than 40 dB rejection, wide TR, and the ABW stability is improved by 4 to 9 times when compared to the state-of-the-art.

2. Chapter 3 presented an electronic monitoring and control system for MEMS tunable EVA-mode filters. The system is based on inductive proximity sensing and was implemented with a control loop on a mm-wave tunable BSF covering the range 30-42 GHz. The measurements demonstrated good system repeatability and long-term performance.

3. Chapter 4 presented the contactless tuning concept to reliably tune high-Q EVA-mode cavity resonators and filters. A full optimization procedure was presented to design the resonator given certain specifications on TR, power handling and tuning reliability. Presented resonators demonstrated more than octave TR with Q_u between 200 and 650, and power handling up to 100 W.

4. Chapter 5 presented a widely-tunable, SIW, DM resonator with mode-independent frequency tuning using two contactless tuners. The resonator demonstrates high Q_u between 150-400 and 94% TR. A second-order reconfigurable bandpass filter

based on the resonator was presented. The filter has a tunable center frequency from 2-3.2 GHz with a reconfigurable TZ that can be located on either the upper or the lower side of the passband.

5. Chapter 6 presented the design of high selectivity and CABW bandpass filters utilizing SIW, DM resonators in an L-shaped coupling scheme. Four tunable filters were presented. The first filter has demonstrated a wide TR ($> 50\%$) with CABW and a TZ on each side of the passband. The next one uses the source-load coupling technique to add two more TZs to further improve the out-of-band rejection. The last two filters demonstrated higher and constant selectivity by combining both TZs on one side of the passband.

7.3 Future Directions

The work presented in this dissertation compliments the extensive research on the design and implementation of high-Q tunable filters. The presented techniques attempts to overcome some of the challenges limiting the integration of such filters in practical systems. However, there is a potential to further improve the presented techniques and address a wider scope of challenges. This discussion presents some of the recommended directions for future research efforts focusing on tunable cavity filters.

7.3.1 High Frequency Bandstop Filters

In Chapter 2 we presented two QABS filters. The filters demonstrated high performance in several aspects. However, the filters suffered from high out-of-band IL. The loss is mainly due to the connectorized fixture used to integrate the filters. Future solutions are encouraged to implement a connectorized solution with less number of RF transitions in order to reduce the loss and maintain a good level of matching over a wide frequency range.

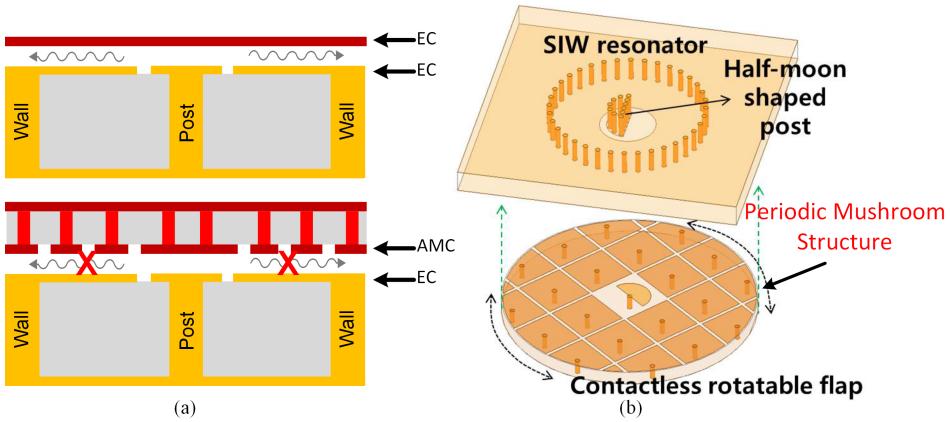

Fig. 7.1.: Artificial magnetic conductor on tuner using mushroom structure [89].

7.3.2 Contactless Tuning Scheme

In Chapter 4, we proposed the contactless tuning concept and provided an extensive study of the optimization process and the expected performance using this concept. It can be observed that one limitation facing this concept is the drop in Q_u when tuning to large air gap values. This is due to the increased radiation losses. One technique that could potentially reduce the drop in Q_u is creating an artificial magnetic conductor (AMC) using the periodic mushroom structure on the tuner to prevent signal propagation between the tuner and the cavity as shown in Fig. 7.1(a) . This idea was first proposed in [89], where a rotateable contactless tuner was used to tune the resonator frequency as shown in Fig. 7.1(b). This structure or similar ones should be able to minimize radiation losses. However, further investigation is required in order to evaluate the effectiveness of this technique and its limitations.

We have also showed the effect of the dielectric loss tangent in limiting the Q_u at larger gap values. In order to mitigate this effect, substrates with lower loss tangent will result in better Q_u values. Furthermore, these losses could be completely avoided by creating an air gap between the post patch and cavity top metal layer. This could be obtained using machined or injection-molded cavity structures.

One advantage of the contactless tuning structure is that tuning-related performance is solely dependent on the used actuator. Therefore, the reliability of the filter tuning is a direct representation of the actuator reliability and therefore the need for a monitoring and control system could be avoided. However, if the actuator does not satisfy the required stability/repeatability specifications, integrating a monitoring system might be required. Unlike the flexible membrane tuning, with the contactless tuner structure there is a direct access to the air gap creating the tuning capacitance. Therefore, a capacitive structure on the cavity substrate which has an overlapping area with the tuner would have a 1:1 relation with the center frequency. And this relation is expected to have higher repeatability due to the load-free linear movement of the contactless plate. Conversely, in the flexible membrane case, the monitoring has to be done externally and the continuous bending on the membrane might affect the accuracy of the monitoring.

One of the possible implementations of the monitoring device is shown in Fig. 7.2(a). In this structure, two capacitive monitoring elements are added outside the cavity. These capacitive patches overlap with an isolated copper layer on the tuner to minimized RF power leakage from the resonator. The monitoring capacitance parameter (C_{mon}) can be defined as the sum of the capacitance between the two added patches and ground. This capacitance will be dependent on the tuning gap and therefore has a 1:1 relation with the resonant frequency as shown in Fig. 7.2 (b) where C_{mon} is the capacitance at 100 MHz.

In addition to frequency monitoring, the same devices can be readily used for RF power monitoring. The resonator electric field couples to the capacitance patches. For the shown structure, the coupling (S_{31}) value ranges between -40 to -28 dB. This value can be controlled by the position of the capacitance elements and the gap on the tuner between the isolated ring and the main tuning conductor. Since the coupling to the capacitance elements is weak, it would not add any significant loss to the resonator but will provide sufficient signal for power detection at resonance. To summarize, a simple capacitance-based monitoring structure can be easily added for

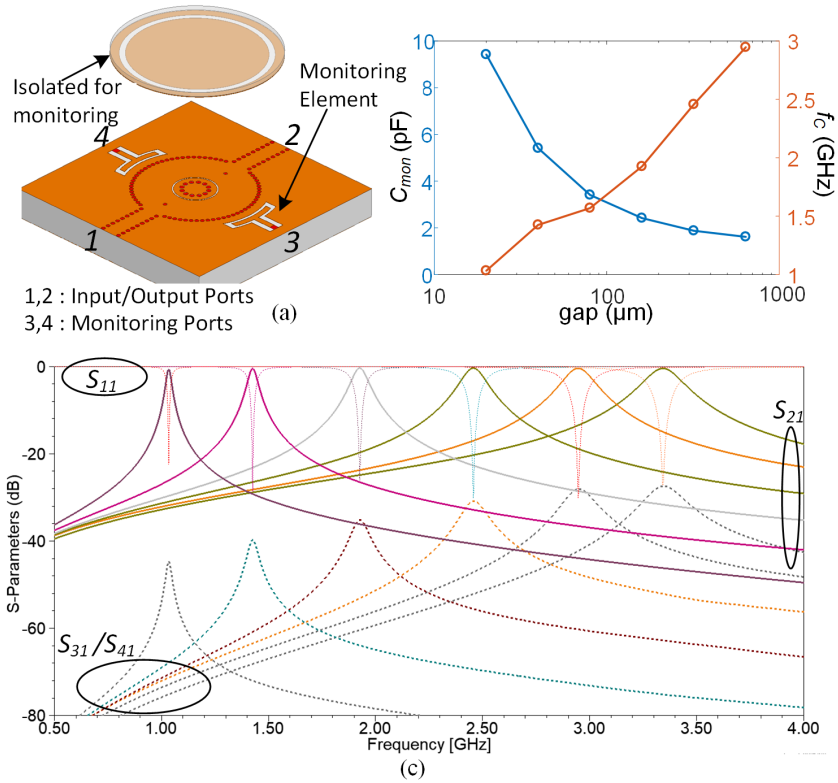

Fig. 7.2.: (a) Proposed structure with added capacitance monitoring elements (b) 1:1 relation between C_{mon} and center frequency (c) S-parameter response of proposed structure with four ports (1,2: input/output, 3,4: monitoring).

frequency and RF power monitoring when using a resonator with contactless tuning concept. This feature is extremely important to overcome the actuator limitations in highly adaptive systems.

7.3.3 Tunable DM SIW Resonator

To improve the design process of filters utilizing tunable DM resonators, more investigation on the external couping method is required. Specifically, a new coupling structure enabling independent control over the coupling to each resonant mode is required. The main challenge in realizing such coupling structure is finding a solution

without using varactors. Once a solution is found, this will enable the realization of wide range of compact filters with complex responses and high reconfigurability.

7.3.4 High Selectivity and CABW Filter Using DM Resonators

The CABW filter design presented in Chapter 6 can be expanded to realize higher order filters. A proposed topology for a fourth-order filter with 4 TZs is shown in Fig. 7.3 (a). An example of the achievable response, using this topology, is shown in Fig. 7.3 (b). The response is optimized to meet certain rejection specifications as highlighted in the figure. Therefore, two TZs are combined on each side of the passband to meet the specifications. The response is compared with the second-order response showing the steeper roll-off and the higher out-of-band rejection as expected. Since the TZs location is dependent on the resonant frequencies of the odd-modes, the filter response is expected to have CABW if designed according to the procedure presented previously in Chapter 6.

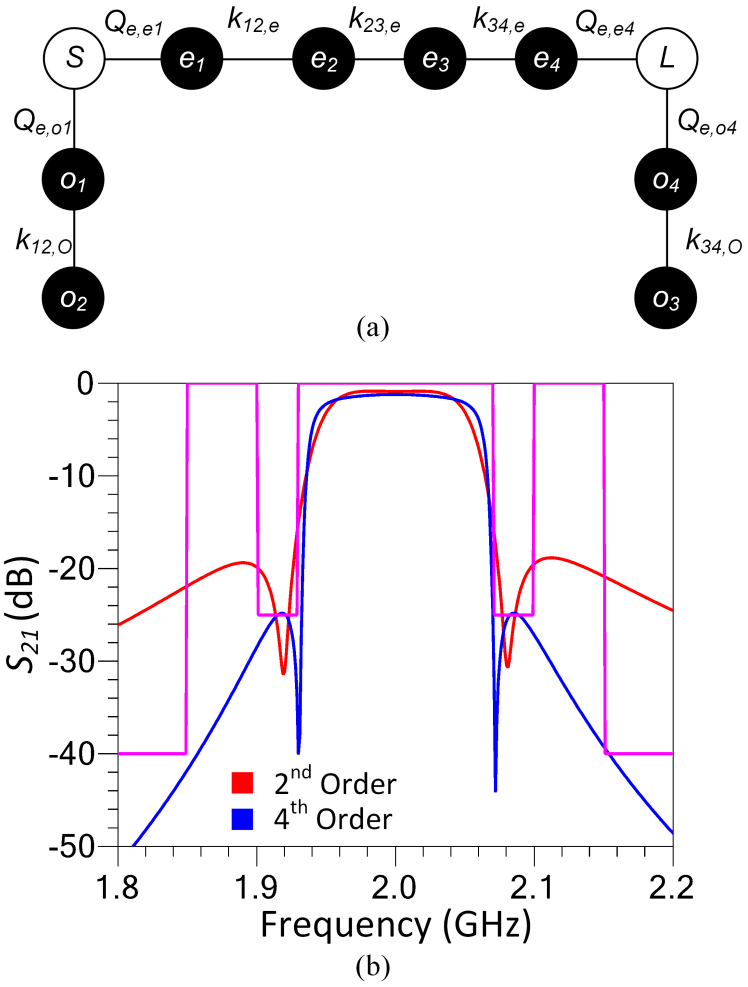

Fig. 7.3.: (a) Proposed topology for a fourth-order filter with 4 TZs using 4 DM resonators (b) response of fourth-order filter compared with second-order.

REFERENCES

REFERENCES

[1] R. J. Cameron, C. M. Kudsia, and R. R. Mansour, *Microwave Filters for Communication Systems: Fundamentals, Design and Applications*, 2nd ed. John Wiley and Sons, Inc., 2018.

[2] K. Chen, "High-power microwave/ radio-frequency components, circuits, and subsystems for next-generation wireless radio front-ends," Ph.D. dissertation, Purdue University, 2013.

[3] D. Peroulis, E. Naglich, M. Sinani, and M. Hickle, "Tuned to resonance: transfer-function-adaptive filters in evanescent-mode cavity-resonator technology," *IEEE Microw. Mag.*, vol. 15, no. 5, pp. 55–69, July 2014.

[4] H. Joshi, H. H. Sigmarsson, D. Peroulis, and W. J. Chappell, "Highly loaded evanescent cavities for widely tunable high-Q filters," in *IEEE MTT-S Int. Microw. Symp. Dig.*, Jun 2007, pp. 2133–2136.

[5] X. Liu, L. P. B. Katehi, W. J. Chappell, and D. Peroulis, "High-Q tunable microwave cavity resonators and filters using SOI-based RF MEMS tuners," *J. Microelectromech. Syst*, vol. 19, no. 4, pp. 774–784, Aug 2010.

[6] S. Moon, H. H. Sigmarsson, H. Joshi, and W. J. Chappell, "Substrate integrated evanescent-mode cavity filter with a 3.5 to 1 tuning ratio," *IEEE Microw. Compon. Lett.*, vol. 20, no. 8, pp. 450–452, Aug 2010.

[7] M. S. Arif and D. Peroulis, "A 6 to 24 GHz continuously tunable, microfabricated, high-Q cavity resonator with electrostatic MEMS actuation," in *IEEE MTT-S Int. Microw. Symp. Dig.*, Jun 2012, pp. 1–3.

[8] Z. Yang, D. Psychogiou, and D. Peroulis, "Design and optimization of tunable silicon-integrated evanescent-mode bandpass filters," *IEEE Trans. Microw. Theory Techn.*, vol. 66, no. 4, pp. 1790–1803, April 2018.

[9] S. Nam, B. Lee, B. Koh, and J. Lee, "Reconfigurable bandpass filter with resonators in cul-de-sacs for producing notches," *IEEE Trans. Compon. Packag. Manuf. Technol.*, vol. 7, no. 9, pp. 1531–1542, Sep 2017.

[10] B. Lee, B. Koh, S. Nam, T. H. Lee, and J. Lee, "Band-switchable substrate-integrated waveguide resonator and filter," *IEEE Trans. Microw. Theory Techn.*, vol. 66, no. 1, pp. 147–156, Jan 2018.

[11] D. R. Jachowski and A. C. Guyette, "Sub-octave-tunable microstrip notch filter," *IEEE International Symposium on Electromagnetic Compatibility*, pp. 99–102, 2009.

[12] D. R. Jachowski, "Compact, frequency-agile, absorptive bandstop filters," *IEEE MTT-S International Microwave Symposium Digest*, pp. 513–516, 2005.

[13] M. D. Hickle and D. Peroulis, "Tunable Constant-Bandwidth Substrate-Integrated Bandstop Filters," *IEEE Transactions on Microwave Theory and Techniques*, pp. 1–13, 2017.

[14] M. D. Hickle, M. D. Sinanis, and D. Peroulis, "Design and implementation of an intrinsically-switched 22-43 GHz tunable bandstop filter," in *IEEE 17th Annual Wireless and Microwave Technology Conference, WAMICON*, 2016.

[15] ——, "Tunable high-isolation W-band bandstop filters," in *IEEE MTT-S International Microwave Symposium*, may 2015, pp. 1–4.

[16] I. Reines, S. J. Park, and G. M. Rebeiz, "Compact low-loss tunable X-band bandstop filter with miniature RF-MEMS switches," *IEEE Transactions on Microwave Theory and Techniques*, vol. 58, no. 7, pp. 1887–1895, 2010.

[17] F. Barriere, A. Pothier, and A. Crunteanu, "A 2 Pole 9.6-11.7 GHz Band Stop Filter Using Analog Tuning RF MEMS Varactors," *41st European Microwave Conference*, pp. 530–533, 2011.

[18] M. D. Hickle and D. Peroulis, "Theory and design of frequency-tunable absorptive bandstop filters," *IEEE Transactions on Circuits and Systems I: Regular Papers*, vol. PP, no. 99, pp. 1–13, 2017.

[19] E. J. Naglich, J. Lee, D. Peroulis, and W. Chappell, "Tunable, substrate integrated, high Q filter cascade for high isolation," in *IEEE MTT-S Int. Microwave Symp. Dig.*, Anaheim, CA, May 2010, pp. 1468–1471.

[20] J. Lee, E. J. Naglich, H. H. Sigmarsson, D. Peroulis, and W. Chappell, "Frequency-agile field-programmable filter array (FPFA) with multiple functionalities," in *IEEE MTT-S Int. Microwave Symp. Dig.*, Baltimore, MD, June 2011, pp. 1–4.

[21] M. Fahmi, J. Ruiz-Cruz, R. Mansour, and K. Zaki, "Compact wide-band ridge waveguide dual-band filters," in *IEEE MTT-S Int. Microwave Symp. Dig.*, Anaheim, CA, May 2010, pp. 888–891.

[22] J. T. Do, Y. Bey, and X. Liu, "A high-Q w band tunable bandpass filter," in *IEEE MTT-S International Microwave Symp.*, San Francisco, CA, May 2016, pp. 1–4.

[23] Z. Yang and D. Peroulis, "A 20–40 ghz tunable MEMS bandpass filter with enhanced stability by gold-vanadium micro-corrugated diaphragms," in *IEEE MTT-S International Microwave Symp.*, San Francisco, CA, May 2016, pp. 1–3.

[24] V. Miraftab and R. Mansour, "Fully automated RF/microwave filter tuning by extracting human experience using fuzzy controllers," *IEEE Trans. Circuits Syst. I, Reg. Papers*, vol. 55, no. 5, pp. 1357–1367, June 2008.

[25] R. Jachowski, "Microprocessor controlled self-tuning resonant cavity and method," USA Patent 4,726,071, feb., 1988.

[26] H. H. Sigmarsson, A. Christianson, H. Joshi, S. Moon, D. Peroulis, and W. Chappell, "In-situ control of tunable evanescent-mode cavity filters using differential mode monitoring," in *IEEE MTT-S Int. Microwave Symposium Dig.*, Boston, MA, June 2009, pp. 633–636.

[27] X. Liu, A. Fruehling, L. Katehi, W. Chappell, and D. Peroulis, "Capacitive monitoring of electrostatic MEMS tunable evanescent-mode cavity resonators," in *Proc. European Microwave Integrated Circuits Conf.*, Manchester, Oct. 2011, pp. 466–469.

[28] J. De Luis, Q. Gu, A. S. Morris, and F. De Flaviis, "A novel frequency control loop for tunable notch filters," *IEEE Trans. Microw. Theory Techn.*, vol. 59, no. 9, pp. 2265–2274, Sept. 2011.

[29] M. Abu Khater and D. Peroulis, "Real-time feedback control system for tuning evanescent-mode cavity filters," *IEEE Trans. Microw. Theory Techn.*, vol. 64, no. 9, pp. 2804–2813, Sept. 2016.

[30] M. Abu Khater, Y. C. Wu, and D. Peroulis, "Tunable cavity-based diplexer with spectrum-aware automatic tuning," *IEEE Transactions on Microwave Theory and Techniques*, vol. 65, no. 3, pp. 934–944, 2017.

[31] M. Abu Khater, M. Abdelfattah, M. D. Sinanis, and D. Peroulis, "An inductor-based real-time monitoring and control system for tunable cavity MEMS filters," in *IEEE MTT-S Int. Microwave Symp. (accepted)*, Philadelphia, PA, USA, 2018.

[32] S. Babic and C. Akyel, "Improvement in calculation of the self- and mutual inductance of thin-wall solenoids and disk coils," *IEEE Trans. Magn.*, vol. 36, no. 4, pp. 1970–1975, July 2000.

[33] H. Wang, W. Li, and Z. Feng, "Noncontact thickness measurement of metal films using eddy-current sensors immune to distance variation," *IEEE Trans. Instrum. Meas.*, vol. 64, no. 9, pp. 2557–2564, Sept. 2015.

[34] S. Jianing, L. Hong, Y. Xiaojie, T. Zheng, and W. Shiheng, "A novel stability analysis approach based on describing function method using for DC-DC converters," in *Proc. IEEE Applied Power Electronics Conf. Exposition*, Charlotte, NC, March 2015, pp. 2642–2647.

[35] M. Abu Khater and D. Peroulis, "Variable-output charge-pump for piezoelectric and electrostatic tunable RF filters," in *IEEE Int. Symp. on Circuits and Systems*, Lisbon, Portugal, May 2015, pp. 1362–1365.

[36] S. Saeedi, S. Atash-Bahar, J. Lee, and H. Sigmarsson, "Control system for piezoelectric-actuator-based tunable evanescent-mode cavity microwave filters," *IEEE Trans. Compon. Packag. Manuf. Technol*, vol. 8, no. 11, pp. 1979–1989, Nov 2018.

[37] A. Anand, J. Small, D. Peroulis, and X. Liu, "Theory and design of octave tunable filters with lumped tuning elements," *IEEE Trans. Microw. Theory Techn.*, vol. 61, no. 12, pp. 4353–4364, Dec 2013.

[38] A. Anand, Y. Liu, and X. Liu, "Substrate-integrated octave-tunable combline bandstop filter with surface mount varactors," in *Proc. IEEE Int. Wireless Symp.*, March 2014, pp. 1–4.

[39] A. Anand and X. Liu, "Reconfigurable planar capacitive coupling in substrate-integrated coaxial-cavity filters," *IEEE Trans. Microw. Theory Techn.*, vol. 64, no. 8, pp. 2548–2560, Aug 2016.

[40] J. D. Martnez, M. Taroncher, and V. E. Boria, "Capacitively loaded resonator for compact substrate integrated waveguide filters," in *Proc. Eur. Microwave Conf.*, Sep. 2010, pp. 192–195.

[41] H. S. Lee and H. J. Eom, "Potential distributions through an annular aperture with a floating inner conductor," *IEEE Trans. Microw. Theory Techn.*, vol. 47, no. 3, pp. 372–374, Mar 1999.

[42] J. D. Martinez, S. Sirci, M. Taroncher, and V. E. Boria, "Compact CPW-fed combline filter in substrate integrated waveguide technology," *IEEE Microw. Compon. Lett.*, vol. 22, no. 1, pp. 7–9, Jan 2012.

[43] ANSYS Q3D Extractor, ANSYS Inc, Southpointe, 2600 ANSYS DRIVE, Canonsburg, PA 15317, USA. [Online]. Available: https://www.ansys.com/es-es/products/electronics/ansys-q3d-extractor

[44] ANSYS High Frequency Structure Simulator (HFSS), ANSYS Inc, Southpointe, 2600 ANSYS DRIVE, Canonsburg, PA 15317, USA. [Online]. Available: https://www.ansys.com/es-es/products/electronics/ansys-hfss

[45] P. Blondy and D. Peroulis, "Handling RF power: the latest advances in RF-MEMS tunable filters," *IEEE Microw. Mag.*, vol. 14, no. 1, pp. 24–38, Jan 2013.

[46] S. Sirci, M. A. Sánchez-Soriano, J. D. Martínez, V. E. Boria, F. Gentili, W. Bsch, and R. Sorrentino, "Design and multiphysics analysis of direct and cross-coupled SIW combline filters using electric and magnetic couplings," *IEEE Trans. Microw. Theory Techn.*, vol. 63, no. 12, pp. 4341–4354, Dec 2015.

[47] K. Chen, H. H. Sigmarsson, and D. Peroulis, "Power handling of high-Q evanescent-mode tunable filter with integrated piezoelectric actuators," in *IEEE MTT-S Int. Microw. Symp. Dig.*, June 2012, pp. 1–3.

[48] S. Saeedi, J. Lee, and H. Sigmarsson, "Prediction of power handling in tunable, high-Q, substrate-integrated, evanescent-mode cavity bandpass filters," *Electronics Letters*, vol. 52, no. 10, pp. 846–848, May 2016.

[49] C. Ernst, V. Postoyalko, and N. G. Khan, "Relationship between group delay and stored energy in microwave filters," *IEEE Trans. Microw. Theory Techn.*, vol. 49, no. 1, pp. 192–196, Jan 2001.

[50] M. Hong, J-S Lancaster, *Microstrip Filters for RF/Microwave Applications*. John Wiley and Sons, Inc., 2001.

[51] New Scale Technologies. M3-L micro linear actuator with embedded controller. [Online]. Available: https://www.newscaletech.com/micro-motion-modules/m3-l-linear-smart-actuators/

[52] J. Jiang and R. R. Mansour, "High-Q tunable filter with a novel tuning structure," in *Proc. Eur. Microw. Conf.*, Oct 2016, pp. 1365–1368.

[53] S. Fouladi, F. Huang, W. D. Yan, and R. R. Mansour, "High-Q narrowband tunable combline bandpass filters using MEMS capacitor banks and piezomotors," *IEEE Trans. Microw. Theory Techn.*, vol. 61, no. 1, pp. 393–402, Jan 2013.

[54] R. Stefanini, M. Chatras, A. Pothier, C. Guines, and P. Blondy, "High-Q 3D tunable RF MEMS filter with a constant fractional bandwidth," in *Proc. Eur. Microw. Integr. Circuit Conf.*, Oct 2013, pp. 312–315.

[55] S. J. Park, I. Reines, C. Patel, and G. M. Rebeiz, "High-Q RF-MEMS 4 - 6-GHz tunable evanescent-mode cavity filter," *IEEE Trans. Microw. Theory Techn.*, vol. 58, no. 2, pp. 381–389, Feb 2010.

[56] A. Anand and X. Liu, "Air cavities integrated with surface mount tuning components for tunable evanescent-mode resonators," in *IEEE MTT-S Int. Microw. Symp. Dig.*, May 2016, pp. 1–4.

[57] A. Semnani, K. Chen, and D. Peroulis, "Microwave gas breakdown in tunable evanescent-mode cavity resonators," *IEEE Microw. Compon. Lett*, vol. 24, no. 5, pp. 351–353, May 2014.

[58] M. F. Hagag, M. A. Khater, M. D. Hickle, and D. Peroulis, "Tunable siw cavity-based dual-mode diplexers with various single-ended and balanced ports," *IEEE Transactions on Microwave Theory and Techniques*, no. 99, pp. 1–11, 2017.

[59] W. Tang and J. Hong, "Varactor-tuned dual-mode bandpass filters," *IEEE Trans. Microw. Theory Techn.*, vol. 58, no. 8, pp. 2213–2219, Aug 2010.

[60] C.-K. Liao, C.-Y. Chang, and J. Lin, "A Reconfigurable Filter Based on Doublet Configuration," in *IEEE MTT-S International Microwave Symposium (IMS)*, June 2007, pp. 1607–1610.

[61] E. J. Naglich, J. Lee, H. H. Sigmarsson, D. Peroulis, and W. J. Chappell, "Intersecting parallel-plate waveguide loaded cavities for dual-mode and dual-band filters," *IEEE Trans. Microw. Theory Techn.*, vol. 61, no. 5, pp. 1829–1838, May 2013.

[62] J. R. Chen, M. D. Benge, A. Anand, H. H. Sigmarsson, and X. Liu, "An evanescent-mode tunable dual-band filter with independently-controlled center frequencies," in *IEEE MTT-S Int. Microw. Symp. Dig.*, May 2016, pp. 1–4.

[63] M. A. Sanchez-Soriano, S. Sirci, J. D. Martinez, and V. E. Boria, "Compact bandpass filters based on a new substrate integrated waveguide coaxial cavity," in *2016 IEEE MTT-S International Microwave Symposium (IMS)*. IEEE, May 2016, pp. 1–4.

[64] C.-K. Liao, P.-L. Chi, and C.-Y. Chang, "Microstrip Realization of Generalized Chebyshev Filters With Box-Like Coupling Schemes," *IEEE Transactions on Microwave Theory and Techniques*, vol. 55, no. 1, pp. 147–153, Jan 2007.

[65] K. Entesari, A. P. Saghati, V. Sekar, and M. Armendariz, "Tunable SIW structures: Antennas, vcos, and filters," *IEEE Microw. Mag.*, vol. 16, no. 5, pp. 34–54, June 2015.

[66] A. Belenguer, H. Esteban, A. L. Borja, and V. E. Boria, "Empty SIW technologies: A major step toward realizing low-cost and low-loss microwave circuits," *IEEE Microw. Mag.*, vol. 20, no. 3, pp. 24–45, March 2019.

[67] M. Abdelfattah and D. Peroulis, "High Q SIW cavity resonaotrs with contactless tuners," *submitted for publication, IEEE Trans. Microw. Theory Techn.*, pp. 1–8, 2019.

[68] B. Lee, S. Nam, T. Lee, and J. Lee, "Third-order frequency-agile substrate-integrated waveguide filter with a pair of transmission zeros," *IEEE Microw. Compon. Lett.*, vol. 27, no. 6, pp. 566–568, June 2017.

[69] F. Mira, J. Mateu, and C. Collado, "Mechanical tuning of substrate integrated waveguide filters," *IEEE Trans. Microw. Theory Techn.*, vol. 63, no. 12, pp. 3939–3946, Dec 2015.

[70] H. Joshi, H. H. Sigmarsson, S. Moon, D. Peroulis, and W. J. Chappell, "High-Q fully reconfigurable tunable bandpass filters," *IEEE Trans. Microw. Theory Techn.*, vol. 57, no. 12, pp. 3525–3533, Dec 2009.

[71] M. F. Hagag, M. Abu Khater, M. D. Sinanis, and D. Peroulis, "Ultra-compact tunable filtering rat-race coupler based on half-mode SIW evanescent-mode cavity resonators," *IEEE Trans. Microw. Theory Techn*, vol. 66, no. 12, pp. 5563–5572, Dec 2018.

[72] V. Sekar and K. Entesari, "A half-mode substrate-integrated-waveguide tunable filter using packaged RF MEMS switches," *IEEE Microw. Compon. Lett.*, vol. 22, no. 7, pp. 336–338, July 2012.

[73] B. You, S. Lu, L. Chen, and Q. J. Gu, "A half-mode substrate-integrated filter with tunable center frequency and reconfigurable bandwidth," *IEEE Microw. Compon. Lett.*, vol. 26, no. 3, pp. 189–191, March 2016.

[74] M. Abdelfattah and D. Peroulis, "A novel independently-tunable dual-mode SIW resonator with a reconfigurable bandpass filter application," in *IEEE MTT-S Int. Microw. Symp. Dig.*, June 2018, pp. 1091–1094.

[75] D. Psychogiou and R. Gmez-Garca, "Multi-mode-cavity-resonator-based bandpass filters with multiple levels of transfer-function adaptivity," *IEEE Access*, vol. 7, pp. 24 759–24 765, 2019.

[76] S. Nam, B. Lee, and J. Lee, "Constant-absolute-bandwidth frequency-tunable half-mode SIW filter containing no tunable coupling structures," in *IEEE MTT-S Int. Microw. Symp. Dig.*, June 2017, pp. 267–270.

[77] S. Sirci, J. D. Mart'nez, V. E. Boria, J. Gil, and L. Marchand, "Design of frequency tunable LTCC coaxial SIW filters with constant passband shape," in *Proc. IEEE MTT-S Int. Conf. on Numerical Electromagnetic and Multiphysics Modeling and Optimization (NEMO)*, Aug 2018, pp. 1–4.

[78] S. Adhikari, A. Ghiotto, and K. Wu, "Simultaneous electric and magnetic two-dimensionally tuned parameter-agile SIW devices," *IEEE Trans. Microw. Theory Techn.*, vol. 61, no. 1, pp. 423–435, Jan 2013.

[79] G. Basavarajappa and R. R. Mansour, "Design methodology of a tunable waveguide filter with a constant absolute bandwidth using a single tuning element," *IEEE Trans. Microw. Theory Techn.*, pp. 1–8, 2018.

[80] M. A. Sanchez-Soriano, S. Sirci, J. D. Martinez, and V. E. Boria, "Compact dual-mode substrate integrated waveguide coaxial cavity for bandpass filter design," *IEEE Microw. Compon. Lett.*, vol. 26, no. 6, pp. 386–388, June 2016.

[81] M. Abdelfattah and D. Peroulis, "A 2.2-3.4 GHz constant bandwidth high-selectivity tunable filter based on dual-mode SIW resonators," in *IEEE MTT-S Int. Microw. Symp. Dig.*, June 2019.

[82] M. Ohira and Z. Ma, "A parameter-extraction method for microwave transversal resonator array bandpass filters with direct source/load coupling," *IEEE Trans. Microw. Theory Techn.*, vol. 61, no. 5, pp. 1801–1811, May 2013.

[83] F. Lin and M. Rais-Zadeh, "Continuously tunable 0.551.9-ghz bandpass filter with a constant bandwidth using switchable varactor-tuned resonators," *IEEE Trans. Microw. Theory Techn.*, vol. 65, no. 3, pp. 792–803, March 2017.

[84] D. Tian, Q. Feng, and Q. Xiang, "Synthesis applied 4th-order constant absolute bandwidth frequency-agile bandpass filter with cross-coupling," *IEEE Access*, vol. 6, pp. 72 287–72 294, 2018.

[85] D. Lu, X. Tang, M. Li, and N. S. Barker, "Four-pole frequency agile bandpass filter with fully canonical response and constant abw," in *IEEE MTT-S Int. Wireless Symp. Dig.*, May 2018, pp. 1–3.

[86] Q. Xiang, Q. Feng, X. Huang, and D. Jia, "Electrical tunable microstrip lc bandpass filters with constant bandwidth," *IEEE Trans. Microw. Theory Techn.*, vol. 61, no. 3, pp. 1124–1130, March 2013.

[87] M. Ohira, S. Hashimoto, Z. Ma, and X. Wang, "Coupling-matrix-based systematic design of single-dc-bias-controlled microstrip higher order tunable bandpass filters with constant absolute bandwidth and transmission zeros," *IEEE Trans. Microw. Theory Techn.*, vol. 67, no. 1, pp. 118–128, Jan 2019.

[88] L. Cao, J. Yan, and L. Yin, "A compact tunable dielectric filter with constant absolute bandwidth," in *Proc. Int. Conf. on Microw. and Millimeter Wave Tech. (ICMMT)*, May 2018, pp. 1–3.

[89] S. Nam, B. Lee, and J. Lee, "Frequency-tunable substrate-integrated waveguide filter using contactless rotatable flaps," in *IEEE MTT-S Int. Microw. Symp. Dig.*, June 2019.

APPENDICES

A. QABS FILTERS TOPOLOGY OPTIMIZATION

This discussion will go over the optimization of the passively-compensated QABS filter topology presented in Chapter 2. The topology schematic is designed using Advanced Design Systems (ADS). The topology definitions as well as the optimization setup is included in the simulation bench.

The topology is designed as shown in Fig. A.1. The resonators are implemented using parallel RLC resonators. The coupling elements and the through TL are employed using ABCD chain component which represent the admittance inverter (J inverter). The circuit is normalized to frequency (i.e. minimum frequency in TR is 1 Hz). The topology implemented is the equivalent of the passively-compensated topology. This means there is one coupling element to each resonator with value k_E^*, and the through line length is θ_T^*. Further details about the topology were discussed in Chapter 2 and in [13].

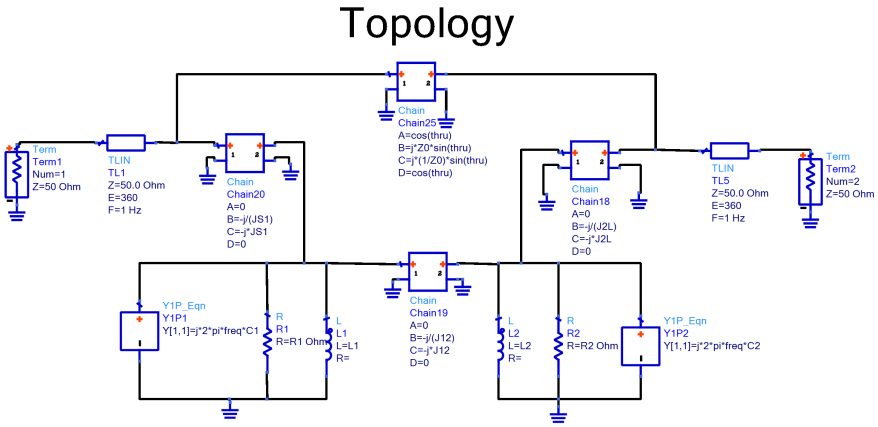

Fig. A.1.: Passively-compensated QABS filter topology implemented in ADS.

The main definitions of the resonators are shown in Fig. A.2. As previously discussed, the two resonators are detuned in order to achieve the AN. The detuning is

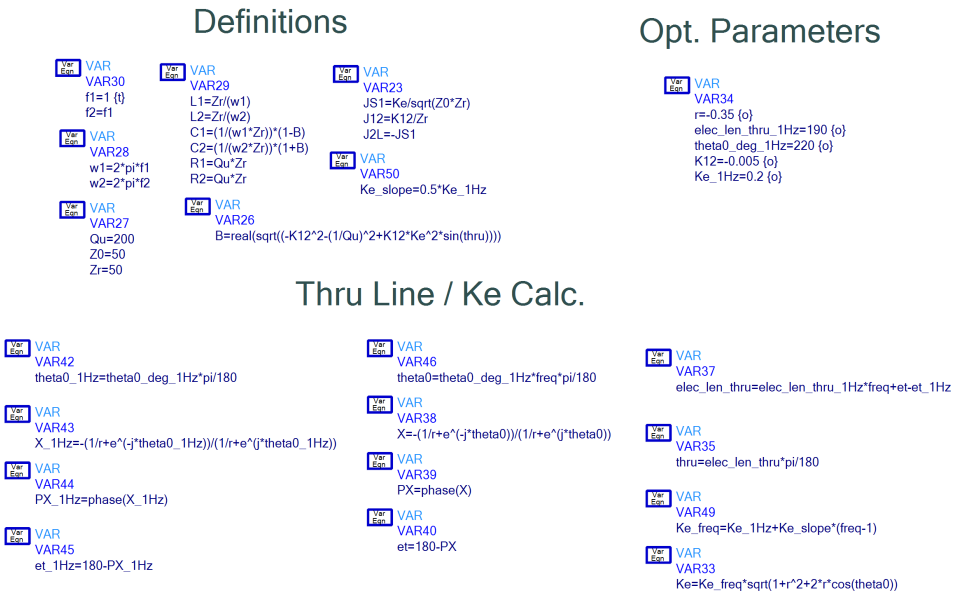

Fig. A.2.: Main topology definitions.

realized using the parameter B, which is used to detune C_1 and C_2. B is dependent on several parameters as defined in the equation. Using this B definition, the AN is achieved when possible according to the conditions previously discussed. The parameter $K_e slope$ defines the rate of external coupling variation with frequency assuming linear variation. The coupling parameters that are used for optimization are also shown in Fig. A.2. For frequency dependent parameters, such as coupling and TL electrical length, the values are defined at 1 Hz. The calculations to obtain the values for k_E^* and θ_T^* are shown in Fig. A.2.

The simulation and optimization setup along with measurements equations is shown in Fig. A.3. The objective for setting up the optimization is find the coupling parameters that results in minimum ABW variation and maximum AN frequency range over a certain range. The ABW can be defined to be measured at any attenuation level by changing (N_dB), the one chosen here is the 3-dB ABW.

The optimization goals definitions are shown in Fig. A.4. The first goals sets the upper and lower limits on the ABW over a certain frequency TR. The second goals is for obtaining a non-zero real value for B over the TR. By having a non-zero real

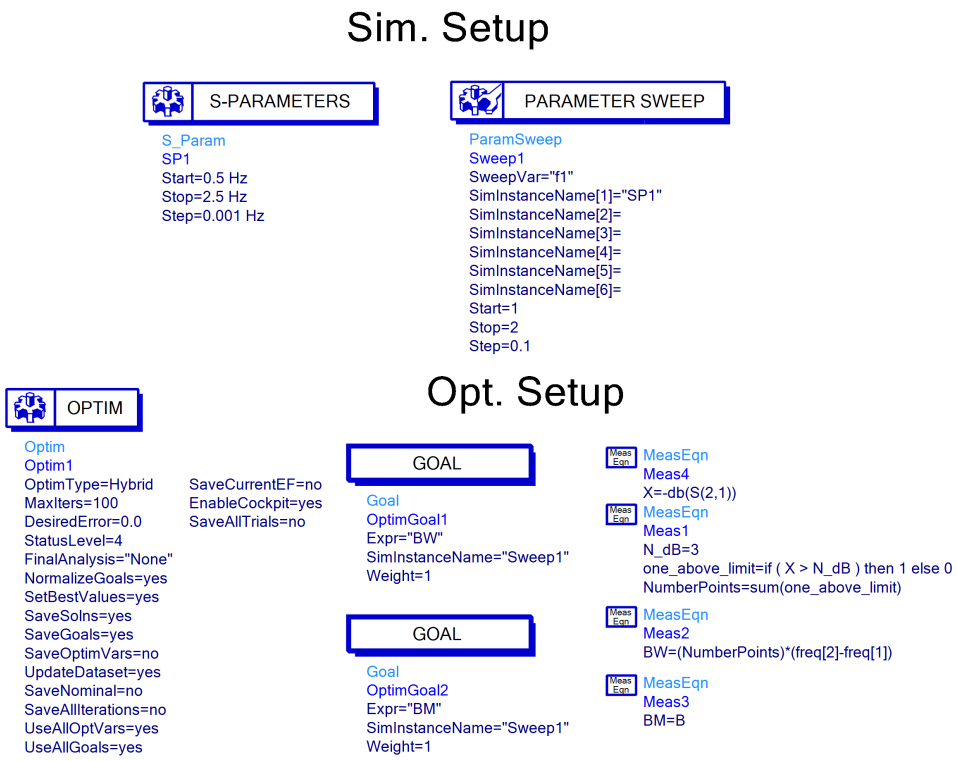

Fig. A.3.: Simulation and optimization setup.

value for B it is guaranteed the AN is obtainable. An optimization example with TR of 1.5:1 is demonstrated in Fig. A.5. Both the specifications and the results are shown.

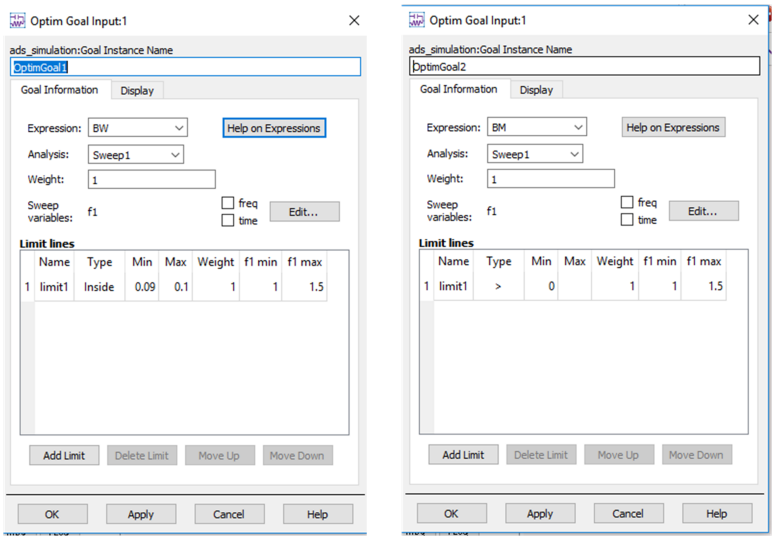

Fig. A.4.: Details of optimizations goals.

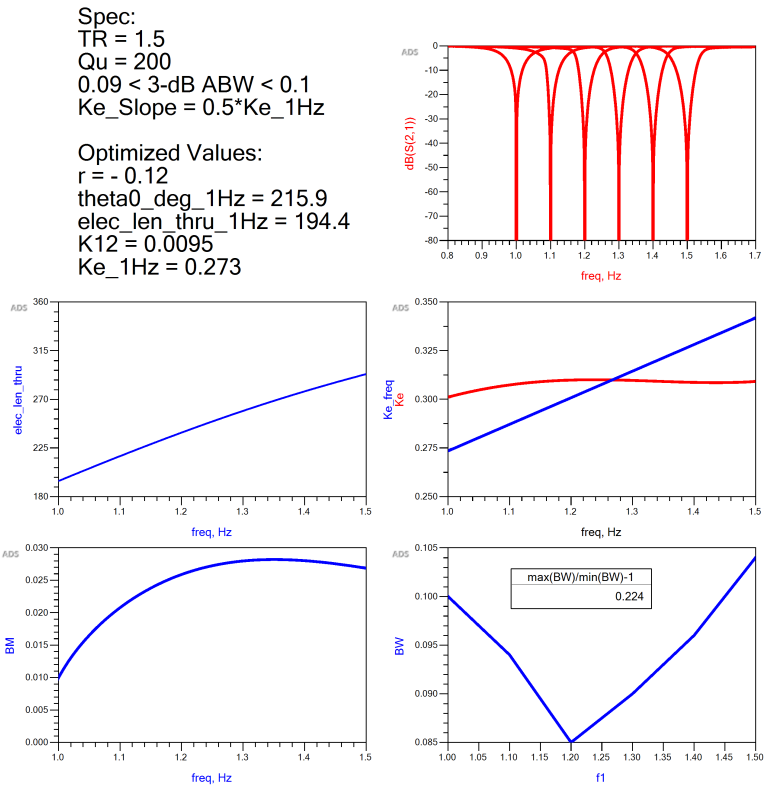

Fig. A.5.: Optimization example using presented bench.

B. SELECTIVITY IMPROVEMENT STUDY FOR CABW HIGH SELECTIVITY FILTER TOPOLOGY

This discussion will investigate the selectivity improvement achievable when using the CABW BPF topology presented in Chapter 6. The topology under investigation is shown in Fig. B.1. The goal of this study is to evaluate the achievable selectivity improvement due to the two additional TZs produced by o_1, o_2.

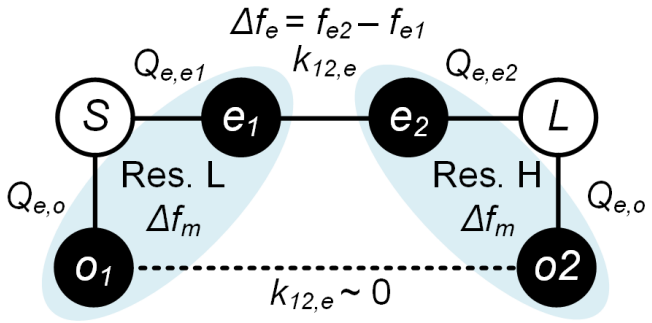

Fig. B.1.: Topology for CABW second-order BPF with two TZs.

The quantity used to evaluate the selectivity is the shape factor (SF) defined as the ratio between the 20-dB ABW and the 3-dB ABW as shown in (B.1).

$$SF = \frac{BW_{20dB}}{BW_{3dB}} \tag{B.1}$$

The main parameter of this study is the separation between the TZs and the center frequency $|f_{TZ} - f_c|$. For each separation value, the topology parameters $(Q_{e,e}, Q_{e,o}, k_{12,e}, \Delta f_e)$ are optimized in order to achieve lowest value for SF while maintaining 3-dB ABW = 100 MHz and RL better than 20 dB and TZ attenuation better than 20 dB. In addition, the study assumes that $Q_u = 300$ for all resonant modes in the topology.

The final response for each optimization case are overlaid and shown in Fig. B.2. The responses are also compared with a conventional Chebyshev response with no TZs.

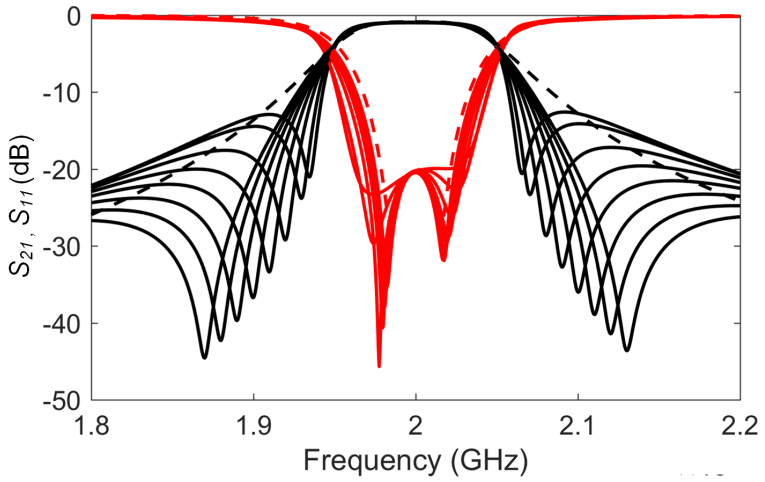

Fig. B.2.: Several bandpass filter responses with different TZ locations.

Table B.1 shows the parameters and the results for each optimization case. It can be observed that the most selective response (minimum SF) is obtained when the TZs are closest to the center frequency. However, there exists a trade-off between the SF and the TZ rejection. Moreover, it can deduced from the coupling parameters values that if the locations of the TZs is further from the passband, stronger external coupling and smaller inter-resonator coupling is used to optimize the SF. To maintain ABW and RL, with this trend, the value of Δf_e is increased resulting in a lower IL.

Table B.1.: Coupling parameters and achieved selectivity for different TZ locations.

$\lvert f_{TZ} - f_c \rvert$ (MHz)	$Q_{e,e}$	$Q_{e,o}$	$k_{12,e}$	Δf_e (MHz)	IL (dB)	TZ Attn. (dB)	SF
65	21.5	41.8	0.041	-21.38	0.91	21	1.315
70	21.22	33.46	0.0413	-25.74	0.92	23.8	1.35
80	19.93	22.56	0.0405	-35.09	0.95	29.2	1.477
90	18.78	17.07	0.04	-42.16	0.97	33.4	1.605
100	17.8	13.82	0.0396	-47.2	0.98	36.7	1.718
110	16.95	11.52	0.0393	-51.8	0.98	39.7	1.83
120	16.23	9.88	0.0391	-55.7	0.98	42.3	1.93
130	15.57	8.65	0.039	-58.91	0.98	44.6	2.02
inf	31.39	NA	0.0354	0	0.87	NA	3.15

VITA

VITA

Mahmoud Abdelfattah received the B.S. degree in electrical engineering from Princess Sumaya University for Technology, Amman, Jordan in 2014. He is currently working toward the Ph.D. degree in electrical and computer engineering at Purdue University, West Lafayette, IN, USA. His current research interests include the design, manufacturing and control of reconfigurable microwave and millimeter-wave cavity filters, lumped-element and planar filters, microwave and millimeter-wave passive components.

In 2018, he joined Qualcomm Inc. where he worked on the design of on-chip passive components for state-of-the-art handset transceivers. He also joined Skyworks Solutions Inc. in 2019 where he worked on the design of multi-chip modules for 5G RF front-ends.

Mr. Abdelfattah is a member of the IEEE Microwave Theory and Techniques Society (IEEE MTT-S). He was a recipient of the IEEE WAMICON Best Paper in Conference Award, 2018, and the Second Place Award of the Student Design Competition on Switchable RF-MEMS Filter in the IEEE MTT-S IMS 2016.